



**Raytheon**

# **GEOLOCATION**

## **VISIBLE/INFRARED IMAGER/RADIOMETER SUITE**

### **ALGORITHM THEORETICAL BASIS DOCUMENT**

**Version 3: May 2000**

James C. Storey

RAYTHEON SYSTEMS COMPANY  
Information Technology and Scientific Services  
4400 Forbes Boulevard  
Lanham, MD 20706

SBRS Document #: Y3258

*NPOESS COMPETITION SENSITIVE*



SDR: GEOLOCATION

Doc No: Y3258

Version: 3

Revision: 0

	Function	Name	Signature	Date
Prepared by	Developer	J. C. STOREY		
Approved by	Relevant IPT Lead	S. MILLER		
Approved by	Chief Scientist	P. ARDANUY		
Released by	Program Manager	H. BLOOM		



## TABLE OF CONTENTS

	<u>Page</u>
LIST OF TABLES .....	vi
GLOSSARY OF ACRONYMS .....	vii
ABSTRACT .....	xi
1.0 INTRODUCTION .....	1
1.1 HISTORICAL PERSPECTIVE .....	2
1.2 PURPOSE .....	4
1.3 SCOPE.....	4
1.4 VIIRS DOCUMENTS.....	5
1.5 REVISIONS .....	5
2.0 EXPERIMENT OVERVIEW .....	6
2.1 OBJECTIVES OF GEORETRIEVAL .....	6
2.2 INSTRUMENT CHARACTERISTICS .....	6
2.2.1 Detector Geometry and Detector Response .....	6
2.2.1.1 Triangular Weighting Function .....	7
2.2.1.2 Location of Spatial Element .....	10
2.2.2 Scan Geometry .....	10
2.3 RETRIEVAL STRATEGY .....	11
3.0 ALGORITHM DESCRIPTION .....	13
3.1 PROCESSING OUTLINE .....	13
3.2 ALGORITHM INPUT .....	13
3.2.1 VIIRS Data .....	13
3.2.2 Non-VIIRS Data.....	13
3.3 THEORETICAL DESCRIPTION OF GEOLOCATION.....	14
3.3.1 Physics of the Problem .....	14
3.3.1.1 Viewing Geometry Overview.....	15
3.3.1.2 Coordinate Systems .....	16
3.3.1.3 Coordinate Transformations.....	23
3.3.2 Mathematical Description of Algorithm .....	28
3.3.2.1 Instrument Model Algorithm.....	28
3.3.2.2 Earth Location Algorithm .....	41
3.3.3 Archived Algorithm Output .....	49
3.4 ERROR ANALYSIS AND SENSITIVITY STUDIES .....	50

3.4.1	Variance or Uncertainty Estimates .....	50
3.4.2	Earth Location Sensitivity to Position/Pointing Error .....	54
3.4.2.1	Pixel and Scan Growth as a Function of Scan Angle .....	54
3.4.2.2	Geolocation Sensitivity to Position Error .....	55
3.4.2.3	Geolocation Sensitivity to Attitude/Pointing Error.....	56
3.4.3	Position and Attitude Error Specification and Estimation .....	57
3.4.3.1	NPOESS Platform Position Error .....	57
3.4.3.2	NPOESS Platform Attitude Error .....	58
3.4.3.3	VIIRS Instrument Pointing Error.....	59
3.4.4	Earth Location Impact.....	61
3.4.4.1	Platform Position Error Component Impact .....	61
3.4.4.2	Platform Attitude Error Component Impact .....	62
3.4.4.3	Instrument Pointing Error Component Impact.....	64
3.4.4.4	Combined Cross-Track and Along-Track Geolocation Error due to Position, Attitude, and Pointing Errors .....	64
3.4.5	Geolocation Equations and Methods .....	67
3.4.6	Ground Processing .....	67
3.4.6.1	Earth Location Processing Approach.....	67
3.4.6.2	Geometric Error Characteristics.....	68
3.4.6.3	Limitations of Ground Processing .....	69
3.4.7	Terrain Height Error Impact .....	69
3.4.8	Summary .....	71
3.4.9	Error Analysis Algorithms .....	71
3.4.9.1	Land Control Point Matching and Correlation Algorithm.....	71
3.4.9.2	Error Analysis and Parameter Estimation Algorithm .....	75
3.5	PRACTICAL CONSIDERATIONS.....	76
3.5.1	Numerical Computation Considerations.....	77
3.5.2	Programming/Procedural Considerations .....	77
3.5.3	Configuration of Retrievals.....	77
3.5.4	Quality Assessment and Diagnostics .....	78
3.5.5	Exception Handling.....	78
3.6	ALGORITHM VALIDATION AND DISCUSSION.....	78
3.6.1	Algorithm Verification.....	78
3.6.1.1	Verification Standard .....	79
3.6.1.2	Preflight Verification .....	79
3.6.1.3	In-flight Verification .....	80
3.6.1.4	Verification of Inputs .....	81
3.6.2	Product Validation .....	84
3.6.3	Risks and Risk Reduction Efforts .....	85
4.0	ASSUMPTIONS AND LIMITATIONS .....	86
4.1	ASSUMPTIONS.....	86
4.2	LIMITATIONS.....	86

5.0 REFERENCES ..... 88

## LIST OF FIGURES

	<u>Page</u>
Figure 1.1-1. VIIRS Instrument and Support Overview.....	3
Figure 1.1-2. Coordinate Systems Overview and Coordinate Transformations.....	3
Figure 2.2-1. Rectangular Response Weighting Function.....	7
Figure 2.2-2. VIIRS Spatial Response Functions .....	8
Figure 2.2-3. Triangular Response Function from the Effective Time Weighting .....	8
Figure 2.2-4. Series of Triangular Weighted Pixels .....	9
Figure 2.2-5. 75 % of Signal is Collected from the Nominal Pixel.....	9
Figure 2.2-6. Panoramic Bow Tie Effect.....	10
Figure 2.2-7. Pixel Size Growth and Overlap within a Scan.....	11
Figure 3.3-1. Growth of Spatial Element Ground Field of View .....	16
Figure 3.3-2. Focal Plane Coordinate System for VIS NIR .....	17
Figure 3.3-3. Instrument, Aft Optics and Half Angle Mirror Coordinate Systems' Relative Orientation .....	18
Figure 3.3-4. Off-Nadir View, Half Angle Mirror Rotation, Telescope Rotation in Instrument Coordinate System.....	19
Figure 3.3-5. Telescope Entrance and Exit Basis Vectors.....	20
Figure 3.3-6. Orbital Coordinate System.....	21
Figure 3.3-7. ECI Coordinate System.....	22
Figure 3.3-8. ECR Coordinate System .....	23
Figure 3.3-9. VIIRS Instrument Model Components .....	28
Figure 3.3-10. Physical Layout of the Focal Planes .....	29
Figure 3.3-11. Measurements of Detector Locations on Focal Plane.....	31
Figure 3.3-12. Mirror Wedge Angles and Axis Errors Definitions.....	34
Figure 3.3-13. Half Angle Mirror Normal Vectors .....	36



Figure 3.3-14.	Encoder Time Sample Interpolation.....	38
Figure 3.3-15.	Ellipsoidal Viewing Vector Intersection .....	42
Figure 3.3-16.	Terrain Intersection Search Geometry .....	47
Figure 3.4-1.	3-Sigma Earth Location Error (Meters) .....	52
Figure 3.4-2.	Earth Location Error Growth .....	53
Figure 3.4-3.	Earth Location Error (in imaging band pixel fraction) Resulting from Various Terrain Height Errors as a Function of Scan Angle .....	53
Figure 3.4-4.	Earth Location Error (in meters) resulting from Spacecraft Position Error (in meters) as a Function of Scan Angle .....	56
Figure 3.4-5.	Earth Location Error (in meters) resulting from Instrument/Platform Pointing Error (in arcseconds) as a Function of Scan Angle .....	57
Figure 3.4-6.	Three-Sigma Earth Location Error (in meters) resulting from the at-launch design for Scan Angles of 0, 20, 30, 35, 40, 45, 50, and 55 degrees .....	66
Figure 3.4-7.	Three-Sigma Earth Location Error (in meters) resulting from the post-calibration estimates for Scan Angles of 0, 20, 30, 35, 40, 45, 50, and 55 degrees.....	67
Figure 3.4-8.	Earth Location Error (in meters) resulting from various Terrain Height Errors as a Function of Scan Angle.....	70
Figure 3.4-9.	Connecting Parts of 3 Scans.....	73
Figure 3.4-10.	Triangular Weighting Function.....	74
Figure 3.4-11.	Satellite Position and Ground Control Point.....	76

## LIST OF TABLES

		<u>Page</u>
Table 3.3-1.	Detector Specifications .....	29
Table 3.3-2.	Detector Sampling .....	31
Table 3.3-3.	Focal Lengths for Each Focal Plane (TBD).....	32
Table 3.3-4.	Half Angle Mirror Assembly Geometric Specifications (TBD).....	33
Table 3.3-5.	Telescope Encoder Geometric Constants .....	36
Table 3.3-6.	Telescope Encoder Geometric Derived Values .....	36
Table 3.4-1.	Geolocation Impact of 3 Sigma Spacecraft Position Errors .....	50
Table 3.4-2.	Geolocation Impact of 3 Sigma NPOESS Platform Attitude Knowledge Error Components .....	51
Table 3.4-3.	Geolocation Impact of 3 Sigma Instrument Pointing Knowledge Error Components .....	51
Table 3.4-4.	Total Combined 3 Sigma RSS Geolocation Error .....	51
Table 3.4-5.	NPOESS Platform Position 3 sigma Error Specification .....	58
Table 3.4-6.	NPOESS Platform Attitude Knowledge 3 sigma Error Specification .....	58
Table 3.4-7.	NPOESS Platform Attitude Knowledge 3 sigma Error Estimates.....	59
Table 3.4-8.	VIIRS Instrument Pointing Knowledge 3 sigma Error Estimates .....	60
Table 3.4-9.	Geolocation Impact of 3 sigma Spacecraft Position Errors .....	62
Table 3.4-10.	Geolocation Impact of 3 NPOESS Platform Attitude Knowledge Error Components .....	63
Table 3.4-11.	Geolocation Impact of 3 sigma VIIRS Instrument Pointing Knowledge Error Components .....	64
Table 3.4-12.	Total Combined 3-sigma RSS Geolocation Error in Cross-Track and Along-Track Directions .....	65
Table 3.6-1.	In-flight Algorithm Verification Activities.....	81

## GLOSSARY OF ACRONYMS

AC	Ambient Calibration and Testing
arcsec	arc second
ATBD	Algorithm Theoretical Basis Document
AVHRR	Advanced Very High Resolution Radiometer
BIH	Bureau International de l'Heure
CCSDS	Consultative Committee on Space Data Systems
CMIS	Conical-Scanning Microwave Imager/Sounder
CrIS	Cross-track Infrared Sounder
CTS	Conventional Terrestrial System
deg	degree
DEM	Digital Elevation Model
DMSP	Defense Meteorological Satellite Program
ECI	Earth Centered Inertial
ECR	Earth Centered Rotating
EDOS	EOS Data and Operations System
EDR	Environmental Data Record
EOS	Earth Observing System
EOSDIS	EOS Data and Information System
EROS	Earth Resources Observation System
ETM+	Enhanced Thematic Mapper Plus
FPA	Focal Plane Assembly
GIIS	General Instrument Interface Specification
GPS	Global Positioning System
GSFC	Goddard Space Flight Center
IERS	International Earth Rotation Service
IFOV	Instantaneous Field of View
IMS	Information Management System
IPO	Integrated Program Office
IPT	Integrated Product Team
IR	Infrared
kHz	kilohertz

km	kilometer
LAC	Local Area Coverage (type of AVHRR data)
Landsat	Land Remote Sensing Satellite
LWIR	Long Wave Infrared (spectral bands)
m	meter
μm	micrometer
μrad	microradian
μsec	microsecond
MISR	Multi-angle Imaging Spectroradiometer
mm	millimeter
MODIS	Moderate-Resolution Imaging Spectroradiometer
mrad	milliradian
msec	millisecond
MSS	Multi-spectral Scanner
MTF	Modulation Transfer Function
MWIR	Medium Wave Infrared
NASA	National Aeronautics and Space Administration
NEDT	Noise Equivalent Temperature Differential
NIMA	National Imagery and Mapping Agency
NIR	Near Infrared (spectral bands)
NOAA	National Oceanic and Atmospheric Administration
NPOESS	National Polar-orbiting Environmental Satellite System
PGS	Product Generation System
POES	Polar Operational Environmental Satellite
QA	Quality Assurance
rad	radian
RMS	Root Mean Square
RSS	Root Sum Square
SBRC	Santa Barbara Research Center
SDST	Science Data Support Team
SeaWiFS	Sea Wide-Field Sensor
sec	seconds
σ	standard deviation

SOM	Space Oblique Mercator
SPOT	System pour l'Observation de la Terre
SRCA	Spectroradiometric Calibration Assembly
SRD	Sensor Requirement Document
SWIR	Short-wave Infrared (spectral bands)
TM	Thematic Mapper
TR	Technical Report
UIID	Unique Instrument Interface Document
USA	United States of America
USGS	United States Geological Survey
VIIRS	Visible/Infrared Imager/Radiometer Suite
VIS	Visible (spectral bands)
WGS84	World Geodetic System 1984



## ABSTRACT

The Visible Infrared Imaging Radiometer Suite (VIIRS) Earth location algorithm will be implemented as part of the VIIRS raw data processing software in order to include Earth location and related spatial information in the VIIRS data products. Earth location data fields will be computed for each VIIRS “spatial element” corresponding to one sample of one ideal radiometric band detector. The Earth location fields, including geodetic latitude, longitude, and height, are computed using rigorous models of the Earth, the NPOESS spacecraft, and the VIIRS instrument. These models account for instrument dynamics including the rotating telescope and half angle mirror, spacecraft position, velocity, and attitude, and the Earth’s terrain surface.

Routine Earth location processing will generate the required data fields using the engineering data contained in the VIIRS raw data stream in conjunction with supporting ancillary data. Offline calibration and analysis activities will ensure the quality of the Earth location data using ground control and instrument/spacecraft parameter estimation techniques. These activities will be particularly intense during the initial checkout and early orbit period when static pointing biases will be measured and removed. Earth location error propagation analyses based on estimates of the spacecraft and instrument performance indicate that a net Earth location accuracy on the order of 200 meters (three sigma circular error) should be achievable with sufficient care devoted to the removal of static errors through on-orbit geometric calibration.





## 1.0 INTRODUCTION

As a part of its Integrated Program Office (IPO) program, NPOESS will provide an enduring capability to measure, on a global basis, atmospheric, land, and ocean environmental parameters. The system will provide timely and accurate weather and environmental data to weather forecasters, military commanders, civilian leaders, and the scientific community. NPOESS converges the National Oceanic and Atmospheric Administration's (NOAA) Polar Operational Environmental Satellites (POES) and the Defense Department's Defense Meteorological Satellite Program (DMSP) into a single system. NPOESS will operate in near circular, sun-synchronous orbit and is scheduled to fly in the 2007-2010 time frame. A host of satellites with sensors operating in different frequency regions of the electromagnetic spectrum will have equatorial crossings at 0530, 0930, and 1330 local time. The Visible/Infrared Imager Radiometer Suite (VIIRS) and Conical-Scanning Microwave Imager/Sounder (CMIS) will form an important part of NPOESS and will share the same platform. The VIIRS and the CMIS will be successors in technology to the Advanced Very High Resolution Radiometer (AVHRR) and the Special Sensor Microwave/Imager (SSM/I), respectively. There are approximately five dozen parameters to be retrieved from the remote sensing data collected by NPOESS and among them six are considered to be "key" parameters (NPOESS, 1999).

This Algorithm Theoretical Basis Document (ATBD) describes the Visible Infrared Imaging Radiometer Suite (VIIRS) Earth location algorithm. This algorithm will be implemented as part of the VIIRS raw data processing software in order to include Earth location and related spatial information in the VIIRS data products. The Earth location algorithm uses Earth ellipsoid and terrain surface information in conjunction with spacecraft ephemeris and attitude data, and knowledge of the VIIRS instrument and National Polar-Orbiting Operational Environmental Satellite System (NPOESS) satellite geometry to compute the geodetic position (latitude, longitude, and height), ground to satellite direction and range, and sun direction for each VIIRS spatial element (0.8 km nadir ground field of view). The heart of the algorithm is a mathematical procedure that intersects the VIIRS instrument's line of sight with the Earth's terrain surface.

The term "spatial element" is used throughout this document to refer to the ground field of view of a single detector sample from one of the 0.8 km nadir resolution VIIRS radiometric bands. A single spatial element is associated with one data sample from each of the radiometric bands and four samples from the imaging bands. These data samples may actually consist of from one to three detector samples due to the VIIRS on-board detector aggregation strategy, described below. The Earth location information generated for each VIIRS spatial element is stored in eight data fields associated with the VIIRS scan image data during instrument data processing. These fields are:

1. geodetic latitude;
2. geodetic longitude;
3. height above the Earth ellipsoid;
4. satellite zenith angle;
5. satellite azimuth;
6. range to the satellite;

7. solar zenith angle; and
8. solar azimuth.

This document describes the algorithm used to generate these eight Earth location related fields and briefly discusses the supporting data preparation and validation processes.

## 1.1 HISTORICAL PERSPECTIVE

The VIIRS Earth location algorithm will operate as part of the raw instrument data processing system for VIIRS data from the NPOESS satellites. Raw instrument data processing involves unpacking and verifying the VIIRS instrument data stream, organizing these data into VIIRS scan oriented data structures, generating the Earth location data, adding associated ancillary information (metadata) required to describe the data set, and producing a data product in a standard format. VIIRS data is in the original un-resampled space throughout the science data processing. In this context, the Earth location data fields are treated as additional attributes of the spatial elements that contain the VIIRS science data, thus describing explicitly each spatial element's ground location.

The VIIRS instrument contains twenty-two spectral bands at two different spatial resolutions with nominal ground fields of view of 400 meters and 800 meters. The higher resolution 400 meter bands are referred to as the imaging bands and the lower resolution 800 meter bands are called the radiometric bands. One of the 800 meter bands is on a separate CCD focal plane that uses variable pixel aggregation to maintain a nearly constant ground footprint. This day/night band has unique geometry and will be treated separately. The detectors from the imaging and radiometric bands are nominally aligned to form spatial elements each with 36 data channels (one from each of the sixteen radiometric bands and four from each of the five imaging bands). The VIIRS Earth location algorithm provides a single set of Earth location fields for each spatial element. This spatial element is modeled as a detector in an "ideal" band(0) placed near the optical axis of the instrument. The exact position of this ideal band will be chosen to best represent the locations of all of the bands (see Figure 2.2-9). The use of the ideal band is explained in Section 3.3.2 Sub-pixel Approximate Ground Location Model.

A set of parametric equations and a table of sub-pixel corrections for each detector in each band will be included in the data product to capture the effects of band-to-band and detector to detector offsets and to permit calculation of the locations of the 400m bands. These are explained in Section 3.3.2 Instrument Model Algorithm/Focal Plane Assembly Model, where the telescope focal length is expressed in mm and detector locations and dimensions are expressed in m. However actual computation is done in meters using ground point coordinates.

An overview of the various sections in this document is presented in Figure 1.1-1. Also an overview of the various coordinate systems and their relationships are illustrated in Figure 1.1-2.

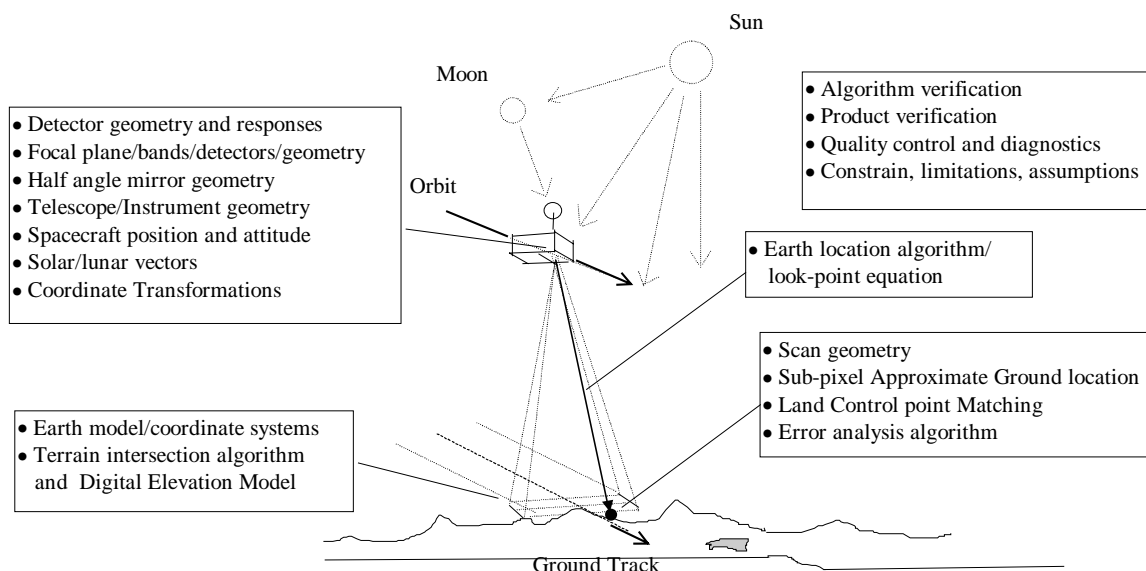


**Figure 1.1-1. VIIRS Instrument and Support Overview**

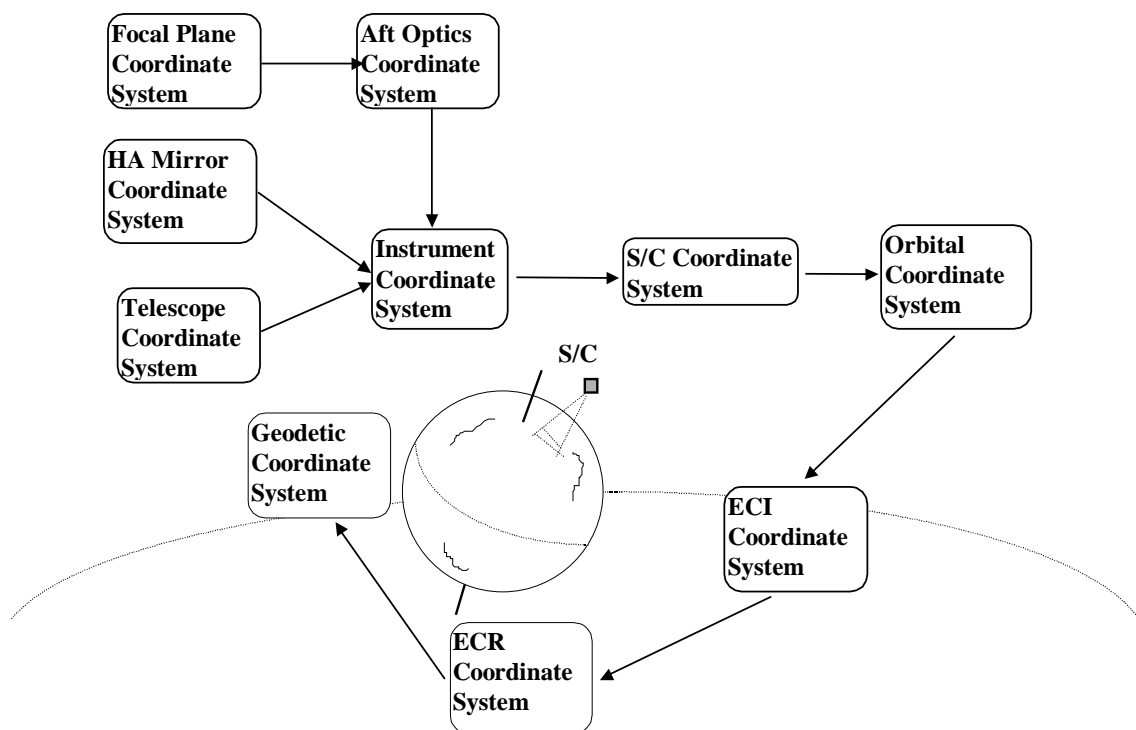


**Figure 1.1-2. Coordinate Systems Overview and Coordinate Transformations**

Similar Earth location algorithms are widely used in modeling and geometrically correcting satellite image data from the Earth Observing System (EOS) Moderate Resolution Imaging Spectroradiometer (MODIS), Land Remote Sensing Satellite (Landsat) Multi-spectral Scanner (MSS), Landsat Thematic Mapper (TM), System pour l'Observation de la Terre (SPOT), and Advanced Very High Resolution Radiometer (AVHRR) missions. In each case, the fundamental

problem is in computing the point at which the sensor line of sight intersects the Earth ellipsoid and/or terrain surface, leading to much commonalty among these algorithms. Experience with SPOT and AVHRR data in particular has demonstrated the importance of compensating for the effects of terrain relief when Earth locating off-nadir satellite imagery.

In the VIIRS data processing system, the Earth location algorithm is used to tag each spatial element with its locational “attributes.” This information contributes to the subsequent science processing and can ultimately be used to perform spatial resampling, if desired. In most Landsat and SPOT applications, the Earth location data are used immediately, prior to data analysis, to resample the instrument detector output to an Earth referenced grid. This contrasts with the spatial attribute tagging approach used for the VIIRS, which is similar to the approach used by the MODIS instrument. This difference in philosophy leads to data processing and data storage considerations that are somewhat unusual for the VIIRS Earth location algorithm. Two places where this is particularly relevant are the density at which Earth locations must be stored to capture the high spatial frequency variations due to terrain relief, and the need to defer band and detector alignment correction until later in the processing stream (see Section 3.3.2).

## 1.2 PURPOSE

This document summarizes the theoretical basis, development process, and functional flow of the Visible/Infrared Imager/Radiometer Suite (VIIRS) geolocation estimation process. The document is evolutionary in nature and will undergo periodic changes to fulfill threshold requirements and some objectives given in the VIIRS Sensor Requirement Documents (SRD) [V-1] and [V-2].

This document identifies sources of input data (both VIIRS and non-VIIRS) that are required for the geolocation retrieval. It provides theory and mathematical background underlying the use of this information in the retrieval process. The implementation, assumptions, and limitations of the adopted approach are also discussed in this document. Some results and validation of the algorithm are also discussed. The main purpose is to provide a sound, repeatable, step-by-step approach for estimating geolocation within the limits defined in the VIIRS Sensor Requirement Document (SRD).

## 1.3 SCOPE

This document describes the conceptual approach and associated mathematical development used to compute the absolute spatial locational attributes for VIIRS sensor data. Some suggestions are provided regarding key implementation issues, but the goal of this document is not to prescribe any particular implementation strategy. The initial draft of this document addresses only the twenty-one imaging and radiometric bands on the visible/near IR, short/mid-wave IR and long-wave IR focal plane assemblies. Treatment of the day/night CCD band will be deferred to a future revision.

## 1.4 VIIRS DOCUMENTS

Reference to VIIRS documents is indicated by a number in brackets, e.g., [V-1].

- [V-1] NPOESS IPO, 1997, Visible/Infrared Imager/Radiometer Suite (VIIRS), Sensor Requirement Document (SRD), Prepared by Associate Directorate for Acquisition, NPOESS Integrated Program Office.
- [V-2] NPOESS IPO, 1998, Visible/Infrared Imager/Radiometer Suite (VIIRS), Sensor Requirement Document (SRD), Prepared by Associate Directorate for Acquisition, Revision 1, NPOESS Integrated Program Office.
- [V-3] NPOESS IPO, 1999, Technical Requirement Document (TRD), Appendix D. Prepared by Associate Directorate for Acquisition, NPOESS Integrated Program Office.
- [C-1] NPOESS IPO, 1997, Conical-scanning Microwave Imager Sounder (CMIS), Sensor Requirement Document (SRD), Prepared by Associate Directorate for Acquisition, NPOESS Integrated Program Office.

## 1.5 REVISIONS

This is the first working version of this document, version 3.0. It is dated May 2000. There were no versions numbered 1.0 or 2.0; the current version number has been selected to match the delivery of the previously existing VIIRS EDR ATBDs, which underwent two previous version releases. It draws heavily on the MODIS Level 1A Earth Location ATBD version 3.0 (Wolfe *et al.*, 1997).

## 2.0 EXPERIMENT OVERVIEW

### 2.1 OBJECTIVES OF GEORETRIEVAL

The eight Earth location data fields include geodetic latitude and longitude, height above the Earth ellipsoid, satellite zenith angle, satellite azimuth, range to the satellite, solar zenith angle, and solar azimuth. These data will be used in subsequent science processing, as well as by the end users of all product levels. The VIIRS SRD requires the Earth location knowledge be accurate to 200 meters ( $3\sigma$ ). This accuracy requirement guides the design of the Earth location algorithm.

The Earth location latitude and longitude reference is needed to relate the VIIRS science data to other spatially referenced data sets, including other VIIRS data, and to provide a uniform, worldwide spatial reference system for all data products. Earth locations are provided at each spatial element in order to capture the terrain relief parallax, the high spatial frequency variations in the locations of off-nadir spatial elements caused by the Earth's terrain. If effects of the parallax were not included, samples in two data sets acquired with different viewing geometry would be incorrectly located relative to each other by tens of kilometers in areas of high relief. Earth location refinement for higher resolution bands and/or to incorporate sub-pixel band/detector misalignment is accomplished by interpolating between spatial element Earth locations using parametric equations (see Section 3.3.2).

The solar angles, satellite angles, satellite range and height are for use in VIIRS science processing, such as atmospheric correction. The ground point height and zenith angles are measured with respect to the local ellipsoid normal. The azimuth angles are relative to local geodetic north.

### 2.2 INSTRUMENT CHARACTERISTICS

The VIIRS sensor will provide global coverage from the NPOESS platform's 833 km descending orbit. The VIIRS sensor is a cross-track sensor with the spectral channels arranged on three focal planes. The minimum swath width is 3000 km. The Instantaneous Field of View (IFOV) and thus the nadir pixel size are variable for the various spectral channels.

Although the basic outline of the Earth location algorithm has much in common with other instruments, there are particular characteristics of the VIIRS instrument and science data stream that have special relevance to Earth location. There are two specific geometric characteristics of the instrument: detector and scan.

#### 2.2.1 Detector Geometry and Detector Response

Of particular significance is the geometry of the multiple detectors (sixteen each for the radiometric bands and thirty-two each for the imaging bands) from the multiple bands, which are themselves distributed over three focal planes. These bands and detectors are nominally aligned into coincident spatial elements corresponding to a single ideal radiometric band IFOV. All detectors from all bands for a nominally aligned family of sixteen spatial elements make up a dataset called a "frame". Misalignments will be measured preflight at the Santa Barbara Research Center (SBRC) and monitored in-flight through image data analysis. The best estimates

of the sub-pixel offsets from nominal locations for each detector in each band will be included with the Level 1A data products for use in subsequent processing.

In developing algorithms for the VIIRS instrument, it is important to understand exactly what the sensor measurements represent. What follows is a basic description of the VIIRS sensor pattern. It describes the response of the instrument on a single pixel basis and shows how individual pixels overlap in the along-scan direction.

### 2.2.1.1 Triangular Weighting Function

The VIIRS instrument has detectors that are rectangular in shape and receive a signal at any particular instant of time from an area of the Earth's surface that is approximately 742 m along-track by 262 m across-track (radiometric bands - all dimensions are for nadir pixels). These asymmetrical detectors are used to compensate for the asymmetrical effects of pixel growth at high scan angles. The 742 m by 262 m nadir footprint grows to approximately 1600 m by 1600 m at the end of scan. In order to maintain more symmetrical pixel dimensions at all scan angles a pixel aggregation scheme is used. At scan angles below  $\pm 31.71$  degrees groups of three samples are aggregated to form a single output pixel with effective dimensions of 742 m by 786 m at nadir. At scan angles between 31.71 degrees and 47.87 degrees a pixel aggregation factor of two is used, transitioning to a factor of one above 47.87 degrees.

There is a temptation to think that the detector dwells over a single location until a sample is taken and then steps to the next pixel. This would produce a rectangular response weighting function as shown in Figure 2.2-1.

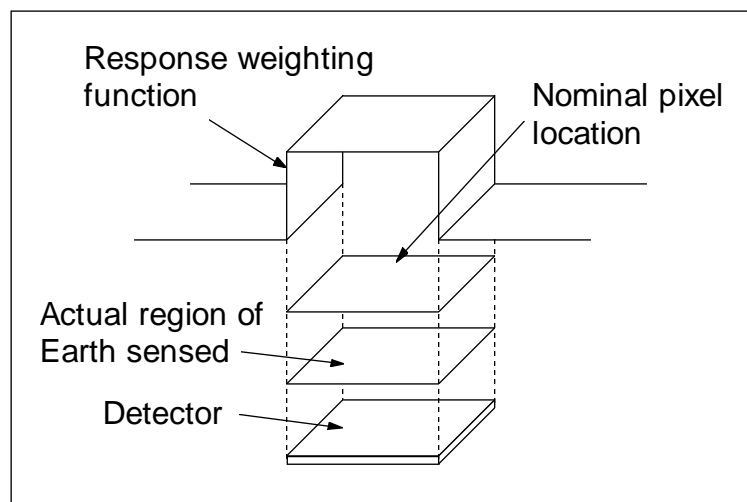


**Figure 2.2-1. Rectangular Response Weighting Function**

However, this is not the case; instead, VIIRS senses the Earth using a telescope that rotates at a constant speed. A single sample consists of the integrated signal received at the detector during the entire sampling interval. This sampling interval is typically the amount of time it takes the projected image of the detector on the ground to move sideways (along-scan) one sample, 89.6  $\mu$ sec (dwell time) for the radiometric bands. The small amount of time at the end of the sampling interval needed to read out the integrated information from the detector and reset the detector is



ignored in this discussion. The degree to which the actual detector dwell time is less than the sampling interval will cause this triangular pattern to have a flattened top, giving it a trapezoidal shape. Pixel aggregation alters the effective response function in a similar way. This effect is shown in Figure 2.2-2.

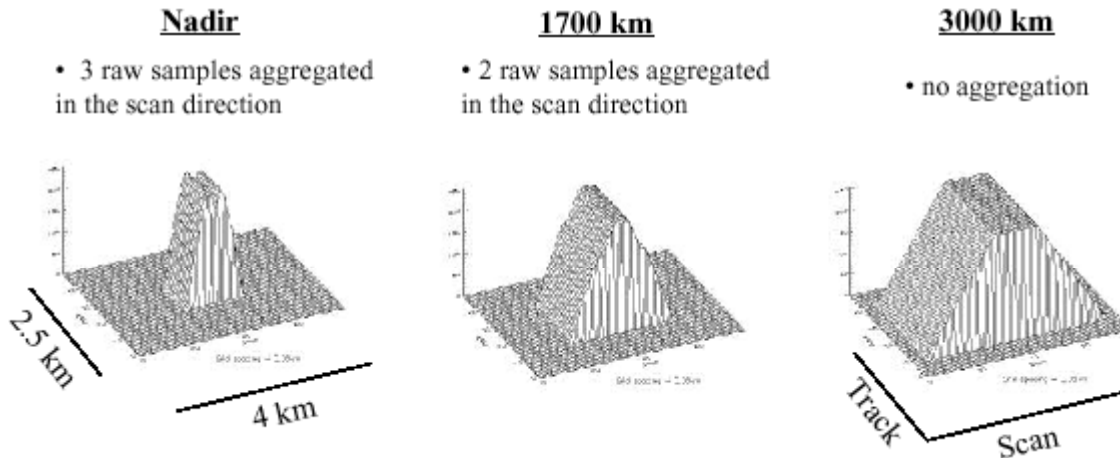


**Figure 2.2-2. VIIRS Spatial Response Functions**

Although what actually happens is that the ground image travels across the detector, it is common to speak as if the pixel moves across the surface of the Earth, which is portrayed in this description. So, for a detector with a perfect rectangular response, the area actually sensed is twice as long as the nominal detector pattern, and the effective time weighted response is triangular as shown in Figure 2.2-3.

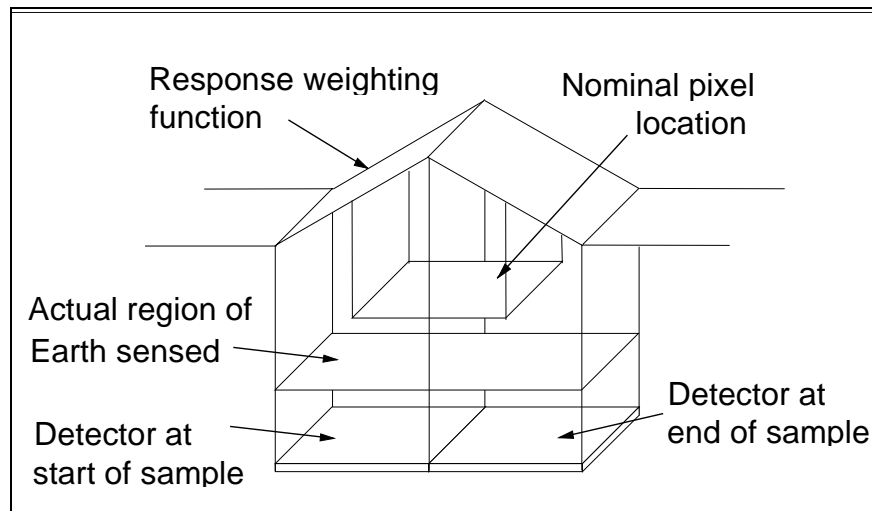


**Figure 2.2-3. Triangular Response Function from the Effective Time Weighting**

Of course, there is not just one sample along a scan line. As soon as the time for one sample ends a new sample is begun. The result is a series of triangular weighted pixels as shown in Figures 2.2-4 and 2.2-5. (For simplicity the remaining figures are done in two dimensions.)



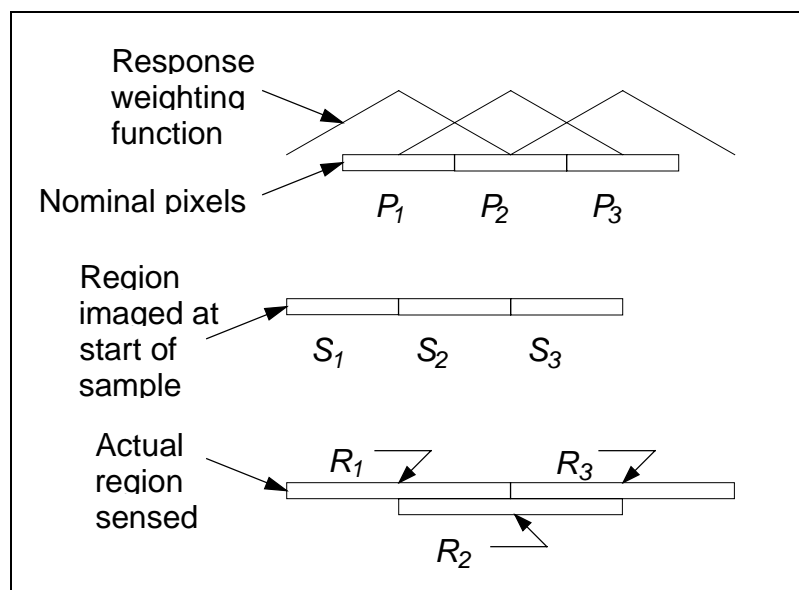


**Figure 2.2-4. Series of Triangular Weighted Pixels**

Figure 2.2-4 shows that nominal pixel P 2 actually obtains signal from the right hand side of nominal pixel P 1 and from the left hand side of nominal pixel P 3. It also shows that a small hot spot in the exact center of region P 1 would have all of its response in P 1, but the same hot spot, such as a fire, located at the right hand edge of P 1 would have half of its response shown in P 1 and half in P 2. Although we speak of nominal 262 m pixels, the signal is obtained from a strip that is 524 m along-scan and 742 km along-track at nadir. In fact, as shown in Figure 2.2-5, for a uniform scene of constant brightness, 12.5% of the signal is collected from each side and 75% of the signal is collected from the nominal pixel itself.

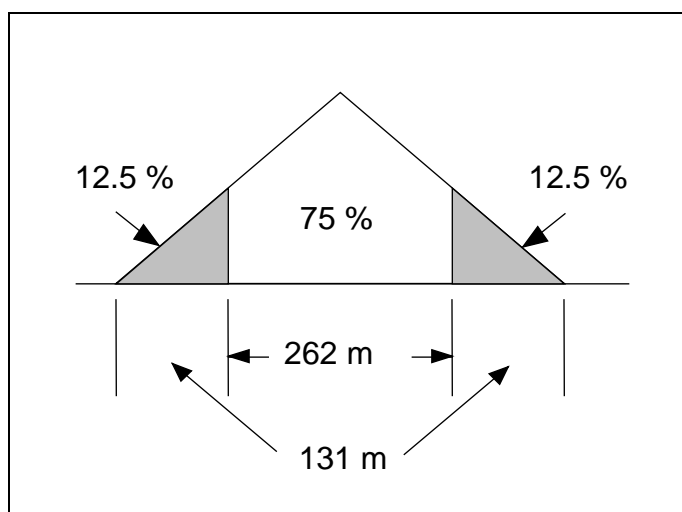


**Figure 2.2-5. 75 % of Signal is Collected from the Nominal Pixel**

### 2.2.1.2 Location of Spatial Element

The location of a spatial element is associated with the center of the pixel response function for an ideal radiometric band detector. From Figure 2.2-4 it can be seen that the peak of the response function corresponds to the location of the detector trailing edge at the end of the sampling interval. Each frame of VIIRS data contains all of the samples from all of the bands corresponding to sixteen radiometric band ground locations along-track. There are thus sixteen spatial elements associated with each data frame. The exact pixel locations for each individual detector from each VIIRS band are computed as offsets from the corresponding spatial element location. Offset values for each detector for each sample aggregation factor will be included in the VIIRS sensor parameter table for use in computing Earth locations for a specific band/detector combination. These offsets will be expressed as pixel fractions along and across scan and will be used to interpolate Earth location field values for the detector from the values for the surrounding spatial elements.

The effective spatial element center must be adjusted to account for pixel aggregation. In the three sample aggregation region the center of the spatial element is associated with the location of the middle of the three aggregated samples. In the two sample aggregation region the spatial element location is associated with the average of the two aggregated sample locations.

### 2.2.2 Scan Geometry

The second characteristic of the VIIRS instrument of particular importance for Earth location is the behavior of the cross-track rotating telescope. The telescope sweeps out a 111 deg Earth field of view in each scan, effectively moving the instrument's sixteen spatial elements over a swath of the Earth approximately 12 km wide at nadir. This scan width increases to 25.6 km at the end of scan due to the panoramic "bow tie" effect (Figure 2.2-6). This effect leads to scan-to-scan overlap at scan angles greater than approximately 19 deg (Figure 2.2-7). On the other hand, the scan gap at nadir is nominally zero. The telescope along-scan motion is measured and down-linked in the instrument data stream. These measurements will be used by the Earth location algorithm to determine the instrument pointing (rather than assuming telescope motion linearity).

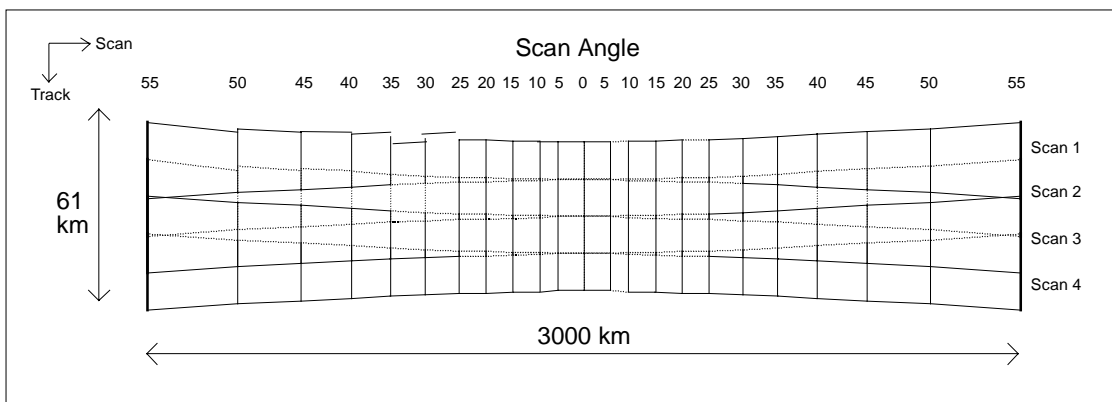


**Figure 2.2-6. Panoramic Bow Tie Effect**

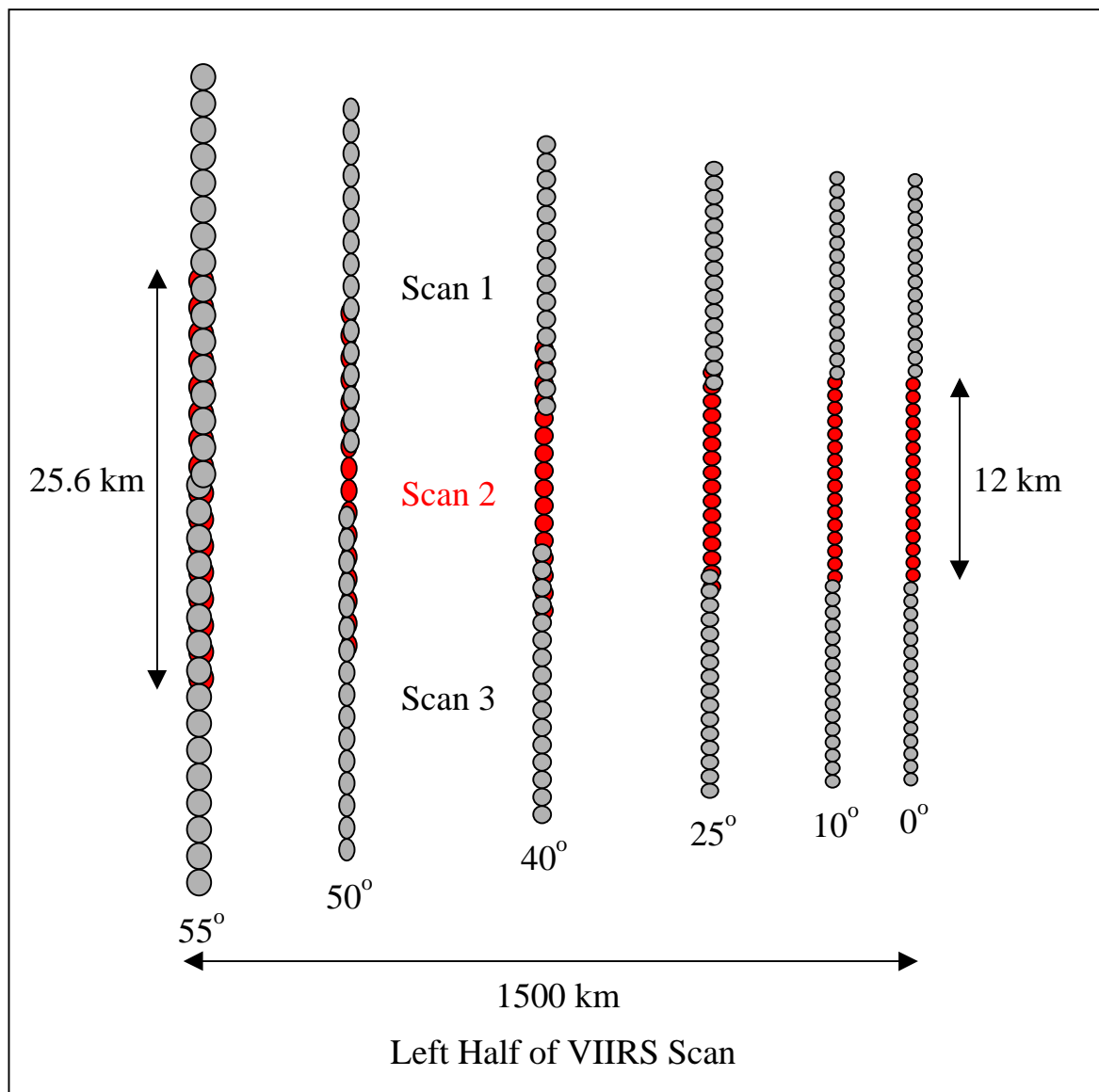


**Figure 2.2-7. Pixel Size Growth and Overlap within a Scan**

### 2.3 RETRIEVAL STRATEGY

The support data accompanying the imagery will be used to compute Earth location information for each VIIRS spatial element. The core of this procedure uses models of the VIIRS sensor and NPOESS spacecraft to construct line-of-sight vectors for each spatial element. The timing information associated with these vectors is then used to intersect them with the terrain surface of the rotating Earth. The geodetic position of this terrain intersection point is stored in the VIIRS product geolocation fields. This procedure is described in section 3.



## 3.0 ALGORITHM DESCRIPTION

### 3.1 PROCESSING OUTLINE

The Earth location process first loads and quality checks the supporting engineering data for the VIIRS data set. These validated support data are then used to construct dynamic models of the VIIRS instrument and NPOESS platform. These models make use of the spacecraft ephemeris and attitude data as well as the instrument telemetry (e.g., telescope encoder data) contained in the VIIRS engineering data. Once constructed, these models are used to generate line-of-sight vectors for each VIIRS spatial element, propagate these vectors through the instrument optics, and orient the vectors in inertial space. Each inertial line-of-sight is then intersected with the rotating Earth, taking into account variations in the Earth's terrain surface by using a digital elevation model.

### 3.2 ALGORITHM INPUT

The VIIRS Earth location algorithm uses the spacecraft and instrument engineering data contained in the VIIRS RDR along with key external support data sets to generate the eight geolocation fields for each VIIRS spatial element. These input data sets are divided into those "internal" VIIRS data that are a part of each VIIRS data set and those ancillary items which must be assembled and maintained on the processing system, independent of the VIIRS data stream.

#### 3.2.1 VIIRS Data

The VIIRS image data itself is not required to perform the routine Earth location processing. Rather it is the engineering data that is of primary importance. In particular, the spacecraft ephemeris and attitude data are used to construct a model of the platform position, velocity, and orientation as a function of time. The VIIRS telescope encoder data contained in the instrument telemetry are used to construct models of the telescope and half angle mirror rotation as functions of time. The scan timing information is used to relate the VIIRS image data samples (spatial elements) to the models of both the dynamic components of the instrument (telescope and half angle mirror) and the spacecraft.

#### 3.2.2 Non-VIIRS Data

Several important ancillary input data sets are used by the VIIRS Earth location algorithm. These include digital elevation data used to describe the Earth's terrain surface, instrument constants used to describe the internal geometry of the VIIRS instrument, and ground control points used to validate the accuracy of the Earth location data.

The digital elevation model (DEM) used by the VIIRS Earth location algorithm will be derived from the best available global database of terrain information including 3 arc-second resolution DEM data generated from the results of the Shuttle Radar Topography Mission (SRTM) where available. Three types of instrument constants are required for VIIRS Earth location processing. Although the term "constants" is used here it is understood that the values of these parameters may be intentionally adjusted, change with time, or may be updated as better knowledge of their true values becomes available. They are constants when generating a particular data product.

The first type of instrument constants include the focal plane, band, and detector locations. These

constants will be stored in the VIIRS data product as a table of locations to generate corrections applicable to each detector (channel) in a spatial element. The second type may be classified as optics parameters. They include the focal lengths of the aft optics, the relationship between the optical axis and instrument alignment axes, angles that describe the half angle mirror surfaces, the relationship between the half angle mirror and telescope assemblies and the instrument alignment axis, and the telescope angle as a function of encoder number. The aft focal lengths are needed to generate a viewing vector from a location on the focal plane. The other optics parameters are needed to determine the orientation of the normal to the half angle mirror surface and the orientation of the telescope at a given sample time. Once this is known, the viewing vector is reflected off the half angle mirror and through the telescope to produce an object space viewing vector. The third type of instrument constant required is the instrument-to-spacecraft alignment matrix. This matrix describes the spatial relationship between the VIIRS instrument alignment axes and the NPOESS spacecraft. This relationship may have a time varying component that can be detected and modeled over time, but will be assumed to be static at launch.

The spacecraft's orbital ephemeris and attitude may be available from either the spacecraft ancillary data packets included in the VIIRS instrument telemetry or from archived ephemeris. Attitude information in the spacecraft ancillary data packets is unreliable during platform maneuvers when the vehicle is commanded away from Earth-centered pointing. Accurate attitude data is required for VIIRS calibration during the spacecraft calibration maneuvers.

The ground control points used to validate the VIIRS Earth location algorithm's performance are image windows containing well defined features with known ground locations. These control points will be collected from a number of sources, including Landsat 7 ETM+ data. The current VIIRS operational concept includes the use of control with a subset of VIIRS data products only. This is based on the idea that it will be more effective to concentrate the acquisition of high quality ground control along a few orbits so that one product in ten, for example, has abundant control rather than all having minimal control. Concentrating high quality control throughout a few orbits allows both short-term and long-term variations in parameter biases to be detected. Additional ground control will be used throughout the rest of the world to verify the accuracy of the Earth location parameters globally.

### 3.3 THEORETICAL DESCRIPTION OF GEOLOCATION

This section presents the underlying theory and mathematical development of the VIIRS Earth location algorithm in Sections 3.3.1 and 3.3.2. Implementation and operational considerations are addressed in Section 3.5.

#### 3.3.1 Physics of the Problem

The supporting theoretical concepts and mathematics of the VIIRS Earth location algorithm are presented in the following subsections. This section presents a review of the VIIRS viewing geometry to put the subsequent discussion in context. This section then addresses the coordinate systems used by the algorithm and the relationships between them, citing references where appropriate. Section 3.3.2 is the heart of this document, presenting the mathematical development of, and solution procedure for, the Earth location algorithm. Section 3.4 discusses estimates of uncertainty and product accuracy issues.

### 3.3.1.1 Viewing Geometry Overview

The VIIRS instrument detectors are aligned in parallel rows on three focal planes assemblies. The aft optics assembly illuminates the detectors on each of the three focal planes. The detector placement geometry and aft optics focal length define the internal geometry of each focal plane relative to the instrument optical axis. Each band consists of a row of either 16 (radiometric bands) or 32 (imaging bands) detectors. The rows of detectors from each band are separated on the focal plane in the along-scan (cross-track) direction. The different bands are aligned into corresponding spatial elements by delaying the samples from each band to account for the slight along-scan motion needed to view the same target point. The instrument's 111.68 deg field of view is swept over the three focal planes by the combined motions of a double-sided rotating half angle mirror and a rotating telescope. The telescope rotates at a rate of 33.471 (TBR) revolutions per minute with the half angle mirror rotating at half this rate to illuminate the aft optics/focal plane assemblies. The VIIRS scan period is 1.7926 (TBR) seconds of which approximately 0.554 (TBR) seconds is devoted to the Earth view portion of the scan. Significant spacecraft motion and Earth rotation take place during this scan period. The detector sampling period is 89.47 (TBR) microseconds with the radiometric bands sampled once per period and the imaging bands sampled twice per period. The sampling strategy also includes along-scan sample aggregation as a function of scan angle, as discussed below.

The 111.68 deg-wide instrument field of view sweeps out a ground swath approximately 3000 km long during the 0.554 seconds Earth view period. The wide ground swath made possible by the  $\pm 55.84$  deg viewing angles exhibits significant Earth curvature effects. The apparent Earth zenith angle of a line of sight at a 55 deg scan angle is increased to approximately 65 deg by Earth curvature. This effect, along with the increasing target range, also contributes to the growth of the projected ground spatial element as a function of scan angle. Asymmetrical detectors are used with a variable pixel aggregation scheme in the cross-track direction to moderate this pixel growth and provide a more uniform ground sample size at all scan angles. The along-scan aggregation factor ranges from 3:1 at nadir to 1:1 at the maximum 55.84 degree scan angle. Figure 3.3-1 is a graph depicting the growth of the spatial element ground field of view with scan angle. The discontinuities in this curve identify the aggregation factor transition points from 3:1 aggregation to 2:1 aggregation at  $\pm 31.71$  degrees and from 2:1 aggregation to 1:1 at  $\pm 47.87$  degrees. The ground dimensions of radiometric band spatial elements range from 0.79 km along-scan by 0.74 km along-track at nadir to 1.6 km along-scan by 1.6 km along-track at a 55.84 deg scan angle. The center of the spatial element (nominal detector) will be used when computing spatial element lines of sight. It should be noted that there is a very small distance between the spatial element center and the centroid of the ground projected field of view for off-nadir pixels. This distance is less than 2 m near the edges of the scan.

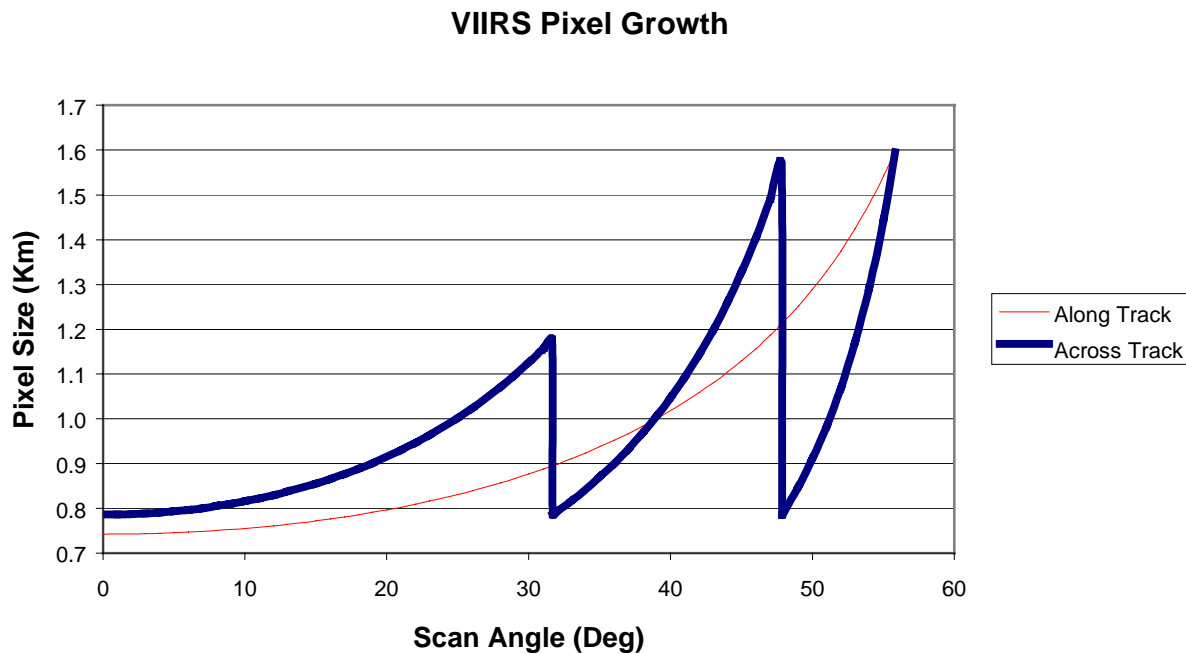


**Figure 3.3-1. Growth of Spatial Element Ground Field of View**

### 3.3.1.2 Coordinate Systems

There are ten basic coordinate systems used by the VIIRS Earth location algorithm. These coordinate systems are defined here and referred to frequently in the remainder of this document. They are presented in the logical order in which a viewing vector and sample time would be transformed into a geodetic position. The orientation of the focal plane, aft optics, half angle mirror, telescope, and instrument coordinate system's axes chosen for this model are somewhat arbitrary. It should also be noted that the origin of the instrument coordinate system does not coincide with the origin of the spacecraft (which is located at the spacecraft center of mass). This offset will be ignored in the rest of the document.

#### Focal Plane Coordinate System

The axis of the focal plane coordinate system coincides with the aft optics z-axis. Because of a small rotation of the focal plane in the aft optics coordinate system, the focal plane coordinate system is needed. The X-axis of the focal plane almost corresponds to the scan direction. The Y-axis corresponds to the negative direction of the ground track. The origin of each focal plane is marked in Figure 3.3-2 using NIR focal plane. A detailed layout of each band and its detectors are shown later in Figure 3.3-10. For example, X-coordinates of the detectors in Band 17 are all positive, while all detectors in band 19 have negative X-coordinates. Detectors are numbered so that detector 1 will see the south of where detector 2 sees on the ground during the descending path.



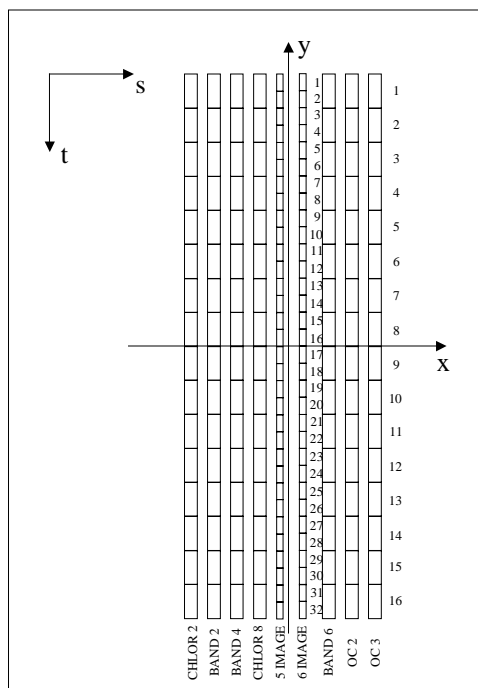


**Figure 3.3-2. Focal Plane Coordinate System for VIS NIR**

### Aft Optics Coordinate System

The aft optics coordinate system is the place where the image space viewing vector is generated for either individual detector samples or for the ideal spatial elements. The origin is where an ideal optical axis intersects the focal planes (Figure 3.3-3 where the focal plane rotation is shown). The Z axis is pointed at the center of the half angle mirror such that it is approximately parallel to the telescope optical axis after reflection off the half angle mirror. The X axis is perpendicular to the half angle mirror's axis of rotation (unless there is some axis error as shown in Figure 3.3-14 and 3.3-15) and is in the along-scan direction after a reflection off the mirror. The positive direction is toward the band on the leading edge of the focal plane. The Y axis is in the focal plane's negative along-track direction after a reflection off the half angle mirror with the positive direction toward the highest detector number.

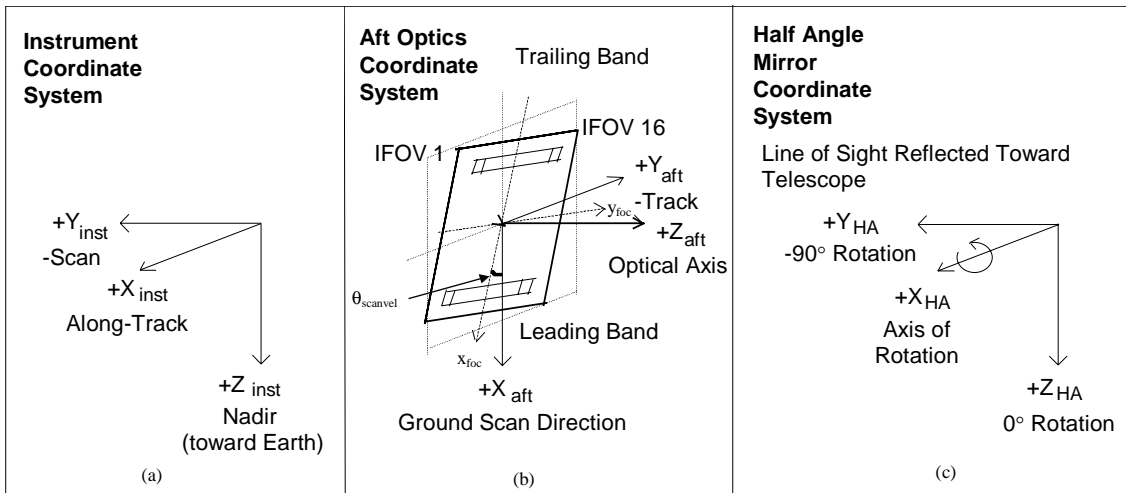


**Figure 3.3-3. Instrument, Aft Optics and Half Angle Mirror Coordinate Systems' Relative Orientation**

### Half Angle Mirror Coordinate System

The half angle mirror model is defined in the half angle mirror coordinate system. It is nominally aligned with the instrument coordinate system. This coordinate system is defined (Figure 3.3-3) so that the X axis is along the axis of rotation of the half angle mirror, which is parallel to the telescope axis of rotation which is also parallel to the along-track direction, and the Z axis is in the nadir direction (downward toward the Earth). The Y axis completes the right handed coordinate system.

When the normal of scan mirror side 1 is parallel to but in the opposite direction from the Z axis, the mirror is defined to have a zero rotation angle (ignoring the small mirror wedge angles and axis error). When the mirror is rotated to either 0 or +180 deg, the line of sight along the aft optics' optical axis is reflected by the mirror directly into the telescope which, in turn, redirects it straight down toward nadir. As the telescope rotates about the scan axis the half angle mirror must rotate at exactly half the telescope rate so that the doubling effect of reflection of the line of sight off the half angle mirror exactly compensates for the telescope rotation. A view of the half angle mirror, telescope, and instrument coordinate systems from the positive X inst is illustrated in Figure 3.3-4 to show their relationship.

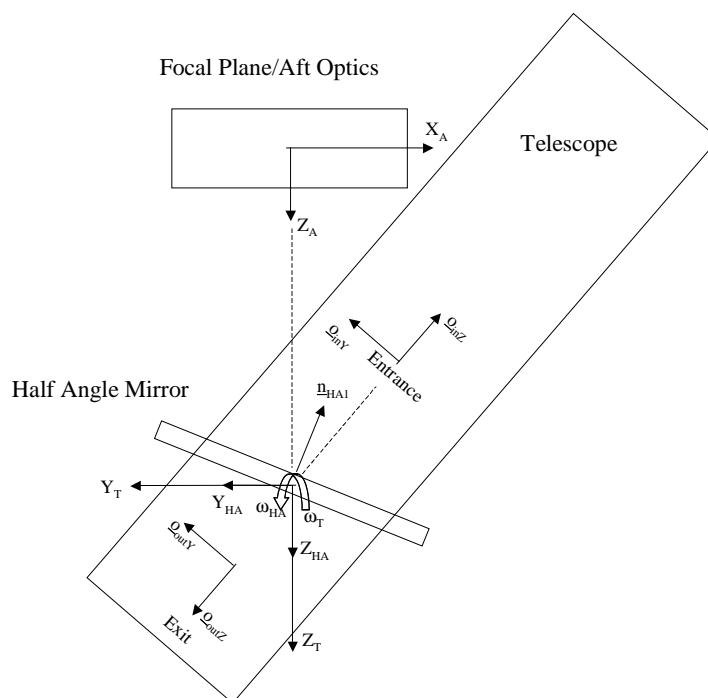


**Figure 3.3-4. Off-Nadir View, Half Angle Mirror Rotation, Telescope Rotation in Instrument Coordinate System**

The matrix expression for the coordinate transformation is given below. It should be noted that the actual locations of the three focal planes vary. However, all the focal planes can be symbolized and placed at one location as depicted in Figure 3.3-4. The light leaving the half angle mirror will be redirected by the aft optics to reach a focal plane.

### Telescope Coordinate System

The telescope coordinate system is nominally aligned with the instrument coordinate system with the X axis being the axis of telescope rotation during scanning. The Y axis is the cross-product of the X axis and the telescope axis at a 0 degree scan angle, and the Z axis completes a right handed coordinate system. This nominally make the Z axis point toward the Earth at nadir (positive toward the Earth). The telescope transforms line of sight vectors from the entrance (aft) aperture to the exit (fore) aperture applying a 4X (de)magnification factor along the way. Figure 3.3-5 shows the construction of a set of basis vectors for the entrance aperture and another for the exit aperture. In each set, the Z axis vector corresponds to the telescope optical axis. These basis vectors can be used to model the telescope operation by mapping line of sight vectors from the half angle mirror onto the entrance basis vectors, applying the magnification scale factor to the aperture X and Y axes, and reconstructing the line of sight at the exit aperture using the exit basis vectors. These aperture basis vectors are constructed in the telescope coordinate system so the incoming line of sight vector must first be transformed from the instrument coordinate system to the telescope coordinate system. Similarly, the outgoing line of sight is transformed from the telescope coordinate system to the instrument coordinate system.

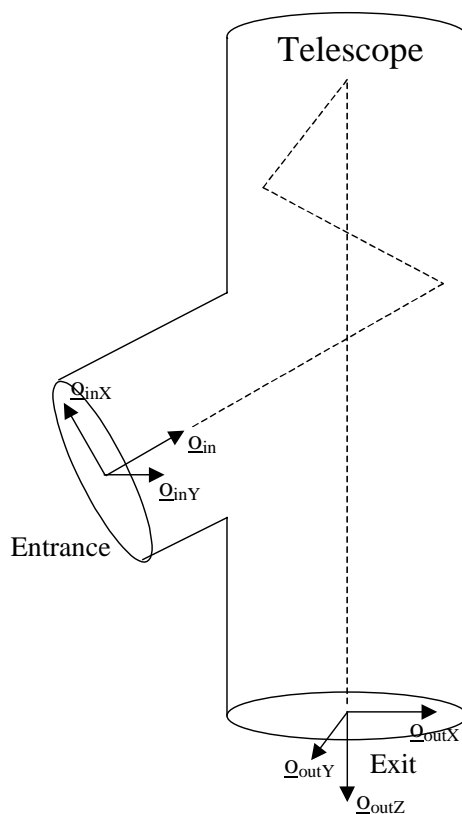


**Figure 3.3-5. Telescope Entrance and Exit Basis Vectors**

### Instrument Coordinate System

The instrument coordinate system (Figure 3.3-3) is the coordinate system in which an image space vector emanating from the center of a detector or spatial element number (1 through 16) and sample time is converted to an object space viewing vector. It is based on the VIIRS reference axes defined by the VIIRS alignment cube. During preflight testing, the actual alignment of the telescope, half angle mirror, aft optics/focal plane, and the spacecraft coordinate system to the instrument coordinate system will be measured. This relationship will be monitored in-flight by analyzing pointing errors as functions of scan angles. This coordinate system is based on preflight measurements of the orientation of the instrument alignment cube. The sides of this cube could be slightly non-orthogonal because of manufacturing limits but an orthogonal transformation is used to convert to and from this coordinate system.

### Spacecraft Coordinate System

The spacecraft coordinate system is fixed to the NPOESS spacecraft with its origin at the spacecraft center of mass. The coordinate axes are defined by the spacecraft attitude control system. It is the orientation of this coordinate system relative to the orbital coordinate system that is captured in the spacecraft attitude data.

## Orbital Coordinate System

The orbital coordinate system is centered on the satellite and its orientation is based on the spacecraft position in inertial space (Figure 3.3-6). The origin is the spacecraft center of mass with the Z axis pointing from the spacecraft center of mass to the Earth center of mass. The Y axis is the normalized cross product of the Z axis and the instantaneous (inertial) velocity vector. It corresponds to the direction of the negative of the instantaneous angular momentum vector direction. The X axis is the cross product of the Y and Z axes.

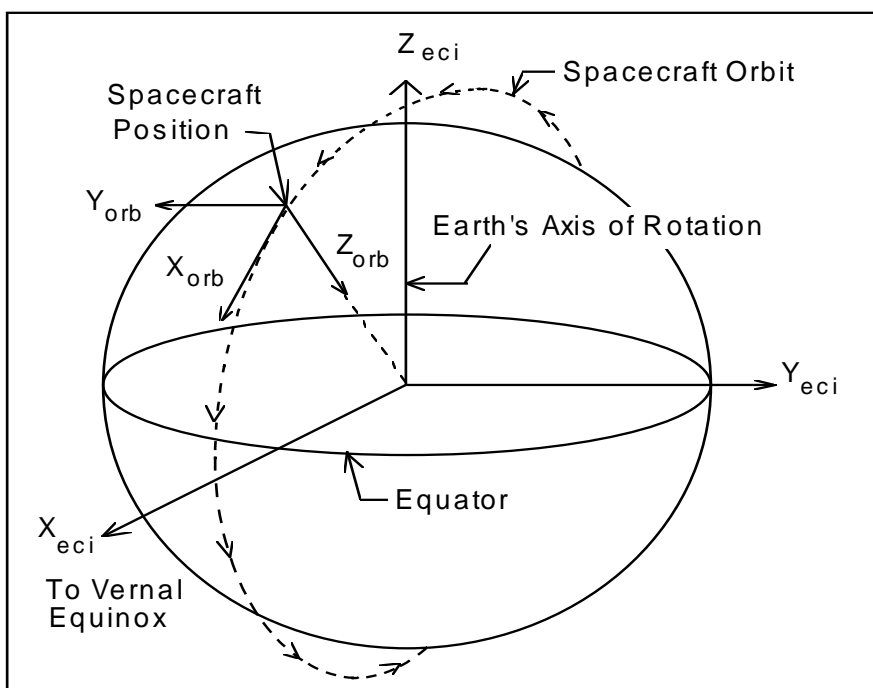


**Figure 3.3-6. Orbital Coordinate System**

## Earth Centered Inertial Coordinate System

The Earth Centered Inertial (ECI) coordinate system is space fixed with its origin at the Earth's center of mass (Figure 3.3-7). The Z axis corresponds to the mean north celestial pole of epoch J2000.0. The X axis is based on the mean vernal equinox of epoch J2000.0. The Y axis is the cross product of the Z and X axes. This coordinate system is described in detail in NIMA, 1997.

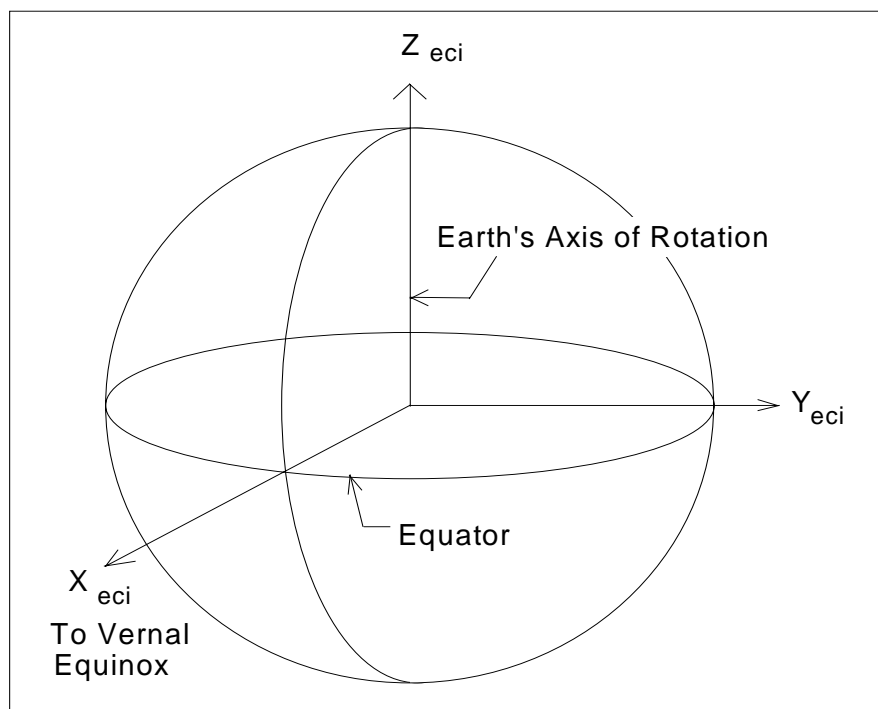


**Figure 3.3-7. ECI Coordinate System**

### Earth Centered Rotating Coordinate System

The Earth Centered Rotating (ECR) coordinate system is Earth fixed with its origin at the center of mass of the Earth (Figure 3.3-8). It corresponds to the Conventional Terrestrial System (CTS) defined by the International Earth Rotation Service (IERS), which is the same as the U. S. Department of Defense World Geodetic System 1984 (WGS84) geocentric reference system. This coordinate system is described thoroughly in NIMA, 1997.

### Geodetic Coordinate System

The geodetic coordinate system is based on the WGS84 reference frame with coordinates expressed in latitude, longitude, and height above the reference Earth ellipsoid. No ellipsoid is required by the definition of the ECR coordinate system but the geodetic coordinate system depends on the selection of an Earth ellipsoid. Latitude and longitude are defined as the angle between the ellipsoid normal and its projection onto the equator and the angle between the local meridian and the Greenwich meridian, respectively. The Earth location data fields in the VIIRS RDR will be expressed in the geodetic coordinate system.

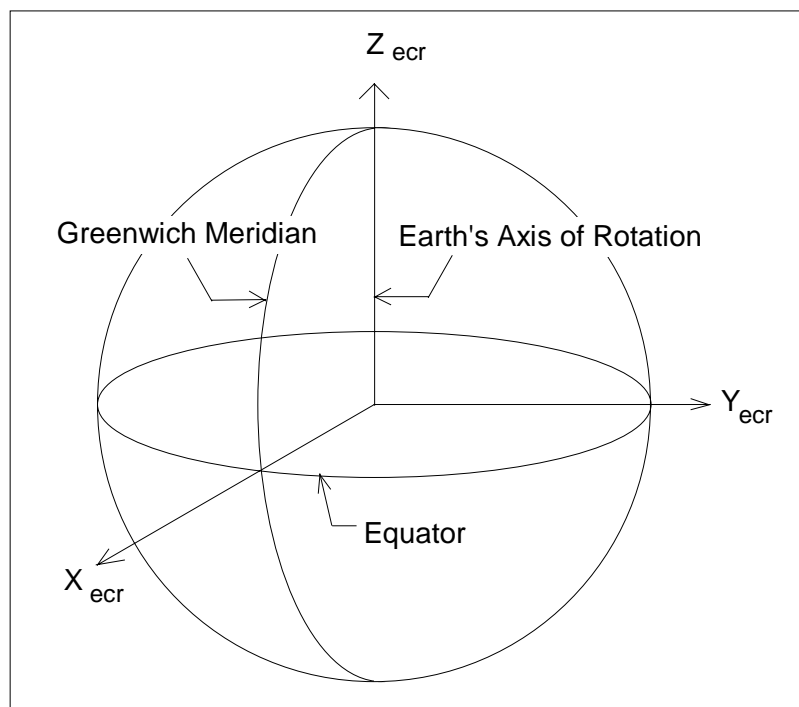


**Figure 3.3-8. ECR Coordinate System**

### 3.3.1.3 Coordinate Transformations

There are nine transformations between the ten basic coordinate systems used by the VIIRS Earth location algorithm. These transformations are referred to frequently in the remainder of this document and are defined here. They are presented in the logical order in which a spatial element number and sample time would be transformed into a geodetic position. An overview of the ten coordinate systems and their relationship is illustrated in Figure 1.1-2.

#### Focal Plane to Aft Optics

Because of the along-track satellite motion during the scan the focal planes are rotated by a small angle  $\theta_{scanvel}$  of -0.129 deg. This rotation is necessary to compensate for the along-track spacecraft sub-satellite point movement of about 65.2 m during the 9.67 msec between the times the bands at the leading and trailing edges see the same area on the ground. The motion along the spacecraft ground track velocity varies a small amount because of the velocity of the Earth relative to the satellite and the orbit's and Earth's eccentricity. The actual rotation will be measured preflight and be included in the transformation from the focal to the telescope coordinate system. If there is a slight difference in rotation between the focal planes one value will be used and the residual rotation will be absorbed in the detector focal plane locations. The transformation matrix for this rotation is given by:

$$\mathbf{T}_{tel/foc} = \begin{bmatrix} \cos(\theta_{scanvel}) & -\sin(\theta_{scanvel}) & 0 \\ \sin(\theta_{scanvel}) & \cos(\theta_{scanvel}) & 0 \\ 0 & 0 & 1 \end{bmatrix} \quad (3.3-1)$$

## Aft Optics to Instrument

The relationship between the aft optics and instrument coordinate systems is described by the aft optics alignment matrix. This relationship will be measured preflight. The transformation  $T_{inst/aft}$  from the aft optics to the instrument coordinate system is a three dimensional transformation implemented as a matrix multiplication. The transformation matrix is expected to be constant in-flight. Considering the half angle mirror angle  $0^\circ$  or  $180^\circ$  to make view vector (0,0,f) should be nadir vector from the telescope pointing to the ground, the aft optics coordinate system is rotated around  $Y_{inst}$  axis by an angle  $\Omega_A$  which is nominally equal and opposite to the rotation of the telescope entrance aperture relative to the instrument coordinate system. In the matrix notation, this is given by:

$$\begin{bmatrix} \cos(\Omega_A) & 0 & -\sin(\Omega_A) \\ 0 & 1 & 0 \\ \sin(\Omega_A) & 0 & \cos(\Omega_A) \end{bmatrix} \quad (3.3-2)$$

See Figure 3.3-4 to understand how the aft optics coordinate system is tilted with respect to the instrument coordinate system.

Relationship between instrument and aft optics coordinate systems before rotation around Y-axis can be expressed by:

$$\begin{bmatrix} 0 & 0 & 1 \\ -1 & 0 & 0 \\ 0 & -1 & 0 \end{bmatrix} \quad (3.3-3)$$

Combining these two transformations,  $T_{inst/aft}$  can be expressed by:

$$\mathbf{T}_{inst/aft} = \begin{bmatrix} 0 & \sin(\Omega_A) & \cos(\Omega_A) \\ -1 & 0 & 0 \\ 0 & -\cos(\Omega_A) & \sin(\Omega_A) \end{bmatrix} \quad (3.3-4)$$

## Half Angle Mirror to Instrument

The relationship between the half angle mirror and instrument coordinate systems is described by the HA mirror alignment matrix. This relationship will be measured preflight. The transformation  $T_{inst/HA}$  from the half angle mirror to the instrument coordinate system is a three dimensional affine transformation implemented as a matrix multiplication. The transformation matrix is expected to be constant in-flight.



The nominal rotation matrix is:

$$\mathbf{T}_{\text{inst/HA}} = \begin{bmatrix} 1 & 0 & 0 \\ 0 & 1 & 0 \\ 0 & 0 & 1 \end{bmatrix} \quad (3.3-5)$$

### Telescope to Instrument

The relationship between the telescope and instrument coordinate systems is described by the transformation matrix  $\mathbf{T}_{\text{inst/tel}}$ . This relationship will be measured preflight. The transformation  $\mathbf{T}_{\text{inst/tel}}$  from the telescope to the instrument coordinate system is a three dimensional affine transformation implemented as a matrix multiplication. The transformation matrix is expected to be constant in-flight.

The nominal rotation matrix is:

$$\mathbf{T}_{\text{inst/tel}} = \begin{bmatrix} 1 & 0 & 0 \\ 0 & 1 & 0 \\ 0 & 0 & 1 \end{bmatrix}$$

### Instrument to Spacecraft

The relationship between the instrument and spacecraft coordinate systems is described by the instrument alignment matrix. This relationship will be measured preflight and refined in-flight as described in Section 3.6.1. The transformation from instrument coordinates to spacecraft coordinates  $\mathbf{T}_{\text{sc/inst}}$  is a three dimensional affine transformation implemented as a matrix multiplication. The transformation matrix will initially be defined to be fixed. Subsequent analysis may detect repeatable variations with time that can be effectively modeled making this a (slowly) time varying transformation.

The terminator flexure effect, non-uniform thermal expansion/contraction when going from the night to day or vice versa, is one of the dynamic error sources that may be included in this time varying transformation. Typically, the settle time for this phenomenon is several minutes and may have very high frequency components (thermal snap). This error source is expected to be relatively small and below the measurement threshold. Still, analysis will follow to determine if a repeatable pattern can be found.

The nominal rotation matrix is the identity matrix:

$$\mathbf{T}_{\text{sc/inst}} = \begin{bmatrix} 1 & 0 & 0 \\ 0 & 1 & 0 \\ 0 & 0 & 1 \end{bmatrix} \quad (3.3-7)$$

## Spacecraft to Orbital

The relationship between the spacecraft and orbital coordinate systems is defined by the spacecraft attitude. This transformation is a three dimensional rotation matrix with the components of the rotation matrix being functions of the spacecraft roll, pitch, and yaw attitude angles. The nature of the functions of roll  $\xi_r$ , pitch  $\xi_p$ , and yaw  $\xi_y$  depends on the exact definition of these angles (i.e. how they are generated by the attitude control system). Wertz (1985) requires the proper order to perform the rotation to be yaw, roll, and pitch. Since the spacecraft attitude is constantly changing, this transformation is time varying. The transformation matrix is:

$$\mathbf{T}_{orb/sc} = \begin{bmatrix} \cos \xi_y & -\sin \xi_y & 0 \\ \sin \xi_y & \cos \xi_y & 0 \\ 0 & 0 & 1 \end{bmatrix} \begin{bmatrix} 1 & 0 & 0 \\ 0 & \cos \xi_r & -\sin \xi_r \\ 0 & \sin \xi_r & \cos \xi_r \end{bmatrix} \begin{bmatrix} \cos \xi_p & 0 & \sin \xi_p \\ 0 & 1 & 0 \\ -\sin \xi_p & 0 & \cos \xi_p \end{bmatrix} \quad (3.3-8)$$

$$\mathbf{T}_{orb/sc} = \begin{bmatrix} \cos \xi_y \cos \xi_p - \sin \xi_y \sin \xi_r \sin \xi_p & -\sin \xi_y \cos \xi_r & \cos \xi_y \sin \xi_p + \sin \xi_y \sin \xi_r \cos \xi_p \\ \sin \xi_y \cos \xi_p + \cos \xi_y \sin \xi_r \sin \xi_p & \cos \xi_y \cos \xi_r & \sin \xi_y \sin \xi_p - \cos \xi_y \sin \xi_r \cos \xi_p \\ -\cos \xi_r \sin \xi_p & \sin \xi_r & \cos \xi_r \cos \xi_p \end{bmatrix}$$

## Orbital to ECI

The relationship between the orbital and ECI coordinate systems is based on the spacecraft's instantaneous ECI position and velocity vectors. The rotation matrix to convert from orbital to ECI can be constructed by forming the orbital coordinate system axes in ECI coordinates:

$\mathbf{p}$  - spacecraft position vector in ECI

$\mathbf{v}$  - spacecraft velocity vector in ECI

$\mathbf{T}_{eci/orb}$  - rotation matrix from orbital to ECI

$$\hat{\mathbf{b}}_3 = -\mathbf{p}/|\mathbf{p}| \quad (\text{nadir vector direction}) \quad (3.3-9)$$

$$\hat{\mathbf{b}}_2 = \hat{\mathbf{b}}_3 \times \mathbf{v} / |\hat{\mathbf{b}}_3 \times \mathbf{v}| \quad (\text{negative of angular momentum vector direction}) \quad (3.3-10)$$

$$\hat{\mathbf{b}}_1 = \hat{\mathbf{b}}_2 \times \hat{\mathbf{b}}_3 \quad (\text{circular velocity vector direction}) \quad (3.3-11)$$

$$\mathbf{T}_{eci/orb} = [\hat{\mathbf{b}}_1 \quad \hat{\mathbf{b}}_2 \quad \hat{\mathbf{b}}_3] \quad (3.3-12)$$

## ECI to ECR

The transformation from ECI to ECR coordinates is a time varying rotation due primarily to Earth rotation but also containing more slowly varying terms for precession, astronomic nutation, and polar wander. The ECI to ECR rotation matrix can be expressed as a composite of these transformations:

$$\mathbf{T}_{ecr/eci} = \mathbf{ABCD} \quad (3.3-13)$$

**A** - Polar Motion

**B** - Sidereal Time

**C** - Astronomic Nutation

**D** - Precession

Each of these transformation terms is described in detail in NIMA, 1997. The actual transformation from ECI to ECR coordinates is done by calling a routine of the SDP Toolkit (see ECS Project, 1995).

### ECR to Geodetic

The relationship between ECR and geodetic coordinates can be expressed simply in its direct form (NIMA, 1997):

$$x = (N + h) \cos(lat) \cos(lon) \quad (3.3-14)$$

$$y = (N + h) \cos(lat) \sin(lon) \quad (3.3-15)$$

$$z = (N(1 - e^2) + h) \sin(lat) \quad (3.3-16)$$

$$N = a / (1 - e^2 \sin^2(lat))^{\frac{1}{2}} \quad (3.3-17)$$

$$e^2 = 1 - \frac{b^2}{a^2} \quad (3.3-18)$$

where:

$(x, y, z)$  - ECR coordinates

$(lat, lon, h)$  - Geodetic coordinates

$N$  - Ellipsoid radius of curvature in the prime vertical

$e$  - Ellipsoid eccentricity

$a, b$  - Ellipsoid semi-major and semi-minor axes

Unfortunately, there is no closed form solution for the inverse problem (which is the problem of interest here). Latitude and height must be solved iteratively for points that do not lie on the ellipsoid surface.

### 3.3.2 Mathematical Description of Algorithm

The VIIRS Earth location algorithm is separated into three parts. The first part describes the algorithm that generates a viewing vector in object space corresponding to either the center of a spatial element or a detector. The second part describes the algorithm that calculates the Earth location of the viewing vector. The third part describes an algorithm for calculating approximate sub-pixel locations. It should be noted that this sub-pixel algorithm is not performed during the VIIRS geolocation processing.

#### 3.3.2.1 Instrument Model Algorithm

A model of the instrument is used to generate an object space viewing vector in instrument coordinates for a spatial element or detector. The instrument model is composed of three elements: the focal plane/aft optics assembly; the half angle mirror assembly; and the telescope as shown in Figure 3.3-9. After discussing each model, a summary of the algorithm for the generation of the viewing vector is given.

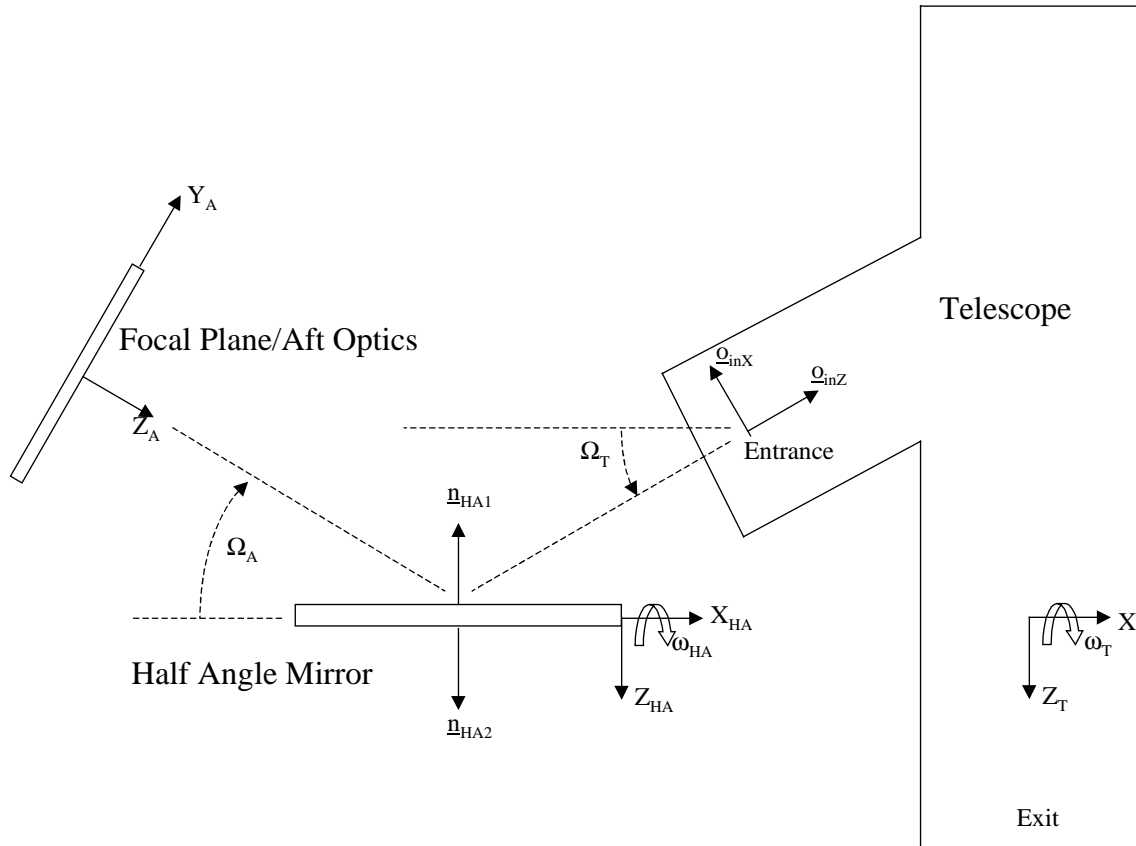


**Figure 3.3-9. VIIRS Instrument Model Components**

Instrument models are described in the following order:

- Focal Plane Assembly Model,
- Detector Sampling and Aggregation,
- Aft Optics Model,
- Half Angle Mirror Assembly Model,
- Telescope Encoder Assembly,
- Telescope Model,
- Generation of the Object Viewing Vector.

### Focal Plane Assembly Model

The layout of the 18 VIIRS spectral bands on the three focal planes is illustrated in Figure 3.3-10. The relationship between the focal plane coordinate system given in Figure 3.3-10 and the aft optics coordinate system is described in the beginning of Section 3.3.1. All three focal planes are rotated around the optical axis.

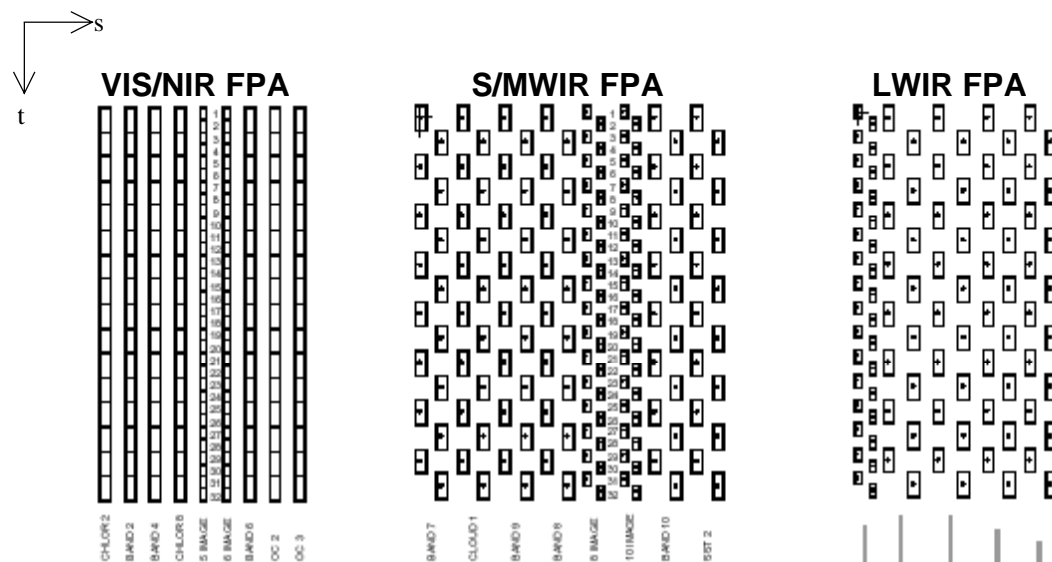


**Figure 3.3-10. Physical Layout of the Focal Planes**

The detector sizes, ground resolutions, and number of detectors for each of the bands is given in Table 3.3-1.

**Table 3.3-1. Detector Specifications**

Bands	Ground Projection	Detector Size	Number of Detectors
Imaging	371 m (Track) by 131 m (Scan)	121.2 $\mu\text{m}$ by 42.8 $\mu\text{m}$	32
Radiometric	742 m (Track) by 262 m (Scan)	242.4 $\mu\text{m}$ by 85.6 $\mu\text{m}$	16

The detectors are laid out on the focal plane so that when they are sampled there are an integral number of frames between the 0.8 km radiometric bands. The actual locations of each of the bands without the optical distortions will be measured both preflight and in-flight. The location  $(x_{i,j}, y_{i,j})$  of the center of detector  $i$  in band  $j$  is:

$$\begin{aligned} x_{i,j} &= x_{\text{cen } j} + x_{\text{res } i,j} \\ y_{i,j} &= y_{\text{cen } j} + y_{\text{space } j} \left[ i - \frac{1}{2} (N_{\text{det } j} + 1) \right] + y_{\text{resi},j} \end{aligned} \quad (3.3-20)$$

where (see Figure 3.3-11):

- $(x_{\text{cen } j}, y_{\text{cen } j})$  - Location of the center of band  $j$  relative to the optical axis
- $N_{\text{det } j}$  - Number of detectors for band  $j$
- $y_{\text{space } j}$  - Spacing between detectors for band  $j$
- $(x_{\text{resi},j}, y_{\text{resi},j})$  - Residual distortion for detector  $i$ , band  $j$
- $i = 1, \dots, N_{\text{det } j}$  - Detector number for band  $j$  (see Table 3.3-1)

For calculations involving ideal band the values for these quantities are:

$$(x_{\text{cen}}, y_{\text{cen}}) = (270\mu\text{m}, 0) \quad (3.3-21)$$

$$N_{\text{det}} = 16 \quad (3.3-22)$$

$$y_{\text{space}} = 242.4\mu\text{m} \quad (3.3-23)$$

$$(x_{\text{resi}}, y_{\text{resi}}) = (0, 0) \quad (3.3-24)$$

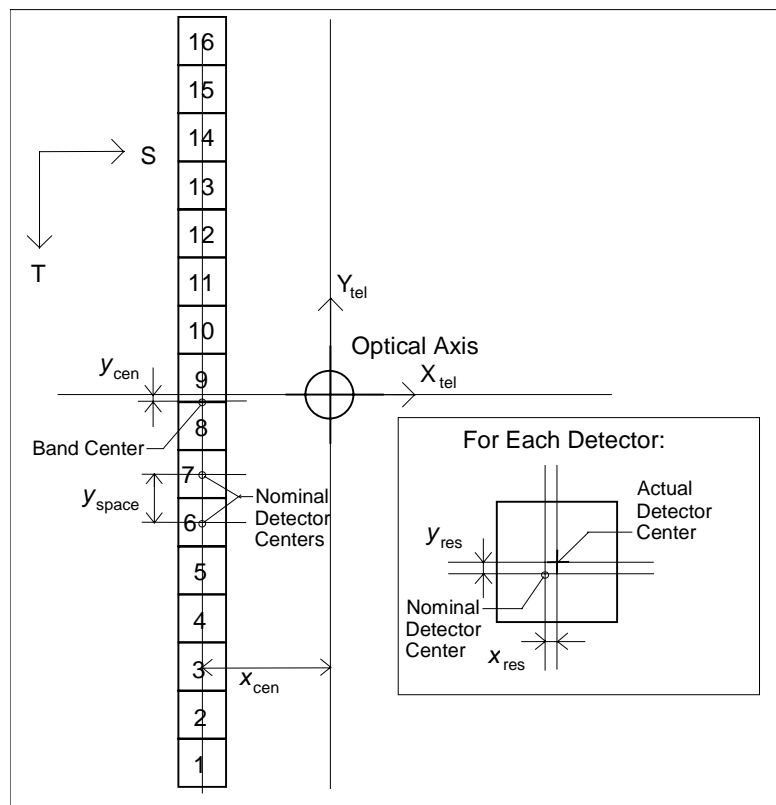


**Figure 3.3-11. Measurements of Detector Locations on Focal Plane**

### Detector Sampling and Aggregation

Radiometric band detectors are sampled every 89.47  $\mu\text{sec}$  and the imaging band detectors are sample twice as often. The raw samples are aggregated in the along-scan direction to normalize the effective ground footprint of each aggregated sample over the full range of VIIRS scan angles, as noted above. There are three aggregation regions: for scan angles between  $-31.71$  degrees and  $+31.71$  degrees three raw samples are aggregated to form out output sample. This reduces the effective number of samples in this zone from 7032 to 2344 for the imaging bands and from 3516 to 1172 for the radiometric bands. The second aggregation zone covers scan angles between  $\pm 47.87$  degrees and  $\pm 31.71$  degrees. Two raw samples are aggregated to create each output sample in this zone. This reduces the effective number of samples in this zone from 3584 (1792 on each side) to 1792 (896 on each side) for the imaging bands and from 1792 (896 on each side) to 896 (448 on each side) for the radiometric bands. For scan angles between  $\pm 55.84$  degrees and  $\pm 47.87$  degrees no sample aggregation is applied. There are 1772 (886 per side) imaging band samples and 886 (443 per side) radiometric band samples in this zone. The sample time, number of raw samples, and number of aggregated samples per scan for each type of band are given in Table 3.3-2.

**Table 3.3-2. Detector Sampling**

Bands	Actual/Effective Sample Time ( $\mu$ s)	Number of Samples per Scan	Number of Samples after Aggregation
Imaging Agg 1	44.74 44.74	1772	1772
Imaging Agg 2	44.74 89.47	3584	1792
Imaging Agg 3	44.74 134.21	7032	2344
Imaging Total	44.74	12388	5908
Radiometric Agg 1	89.47 89.47	886	886
Radiometric Agg 2	89.47 178.94	1792	896
Radiometric Agg 3	89.47 268.41	3516	1172
Radiometric	89.47	6194	2954

For purposes of line-of-sight generation, the effective sample times are taken to be the raw sample time of the central raw sample in the three sample aggregation zone, the mean of the two raw sample times in the two sample aggregation zone, and the raw sample time in the one sample aggregation zone.

### Aft Optics Model

The aft optics are modeled as a simple optical system. There are three (TBD) focal planes illuminated by the aft optics, with several independent elements in the optical path for the longwave IR focal plane. In Table 3.3-3 are the nominal focal lengths for the aft optics for the three (TBD) focal planes: Long Wave Infrared (LWIR); Short and Medium Wave Infrared (SWIR/MWIR); and Near Infrared/Visible (NIR/VIS).

**Table 3.3-3. Focal Lengths for Each Focal Plane (TBD)**

Focal Planes	Focal Length ( $f$ )
LWIR	272.128 mm
SWIR/MWIR, NIR/VIS	272.128 mm

The optical distortion of the lenses for each optical path was modeled before the focal planes were built and the layout of the detectors on the focal plane was adjusted for this distortion. These adjustments to the detector locations are not included in the focal plane coordinates used in the instrument model; thus a simple optical model can be used. Given focal plane coordinates  $(x, y)$  and focal length  $f$ , the corresponding image space viewing vector  $\mathbf{u}_{foc}$  in the aft optics coordinate system is:



$$\mathbf{u}_{\text{foc}} = \begin{bmatrix} x \\ y \\ f \end{bmatrix} \quad (3.3-19)$$

When doing this calculation for the ideal band, a focal length of exactly 272.128 mm (TBR) will be used with  $16 \times 242.4 \mu\text{m} \times 85.6 \mu\text{m}$  (TBR) detectors. The x and y focal plane coordinates are computed as a function of band and detector number as described above

### Half Angle Mirror Assembly Model

The half angle mirror assembly consists of a double-sided mirror and motor-encoder assembly. The half angle mirror assembly geometric specifications are listed in Table 3.3-4 with the corresponding mirror wedge angles and axis errors shown (exaggerated) in Figure 3.3-12.

**Table 3.3-4. Half Angle Mirror Assembly Geometric Specifications (TBD)**

Characteristic	Specification
Wedge Angle $\alpha$	$\leq \text{TBD}$
Wedge Angle $\beta$	$\leq \text{TBD}$
Axes Error $\gamma$	$\leq \text{TBD}$
Axes Error $\delta$	$\leq \text{TBD}$
Along-Track Mirror Axis Dynamic Error (jitter); equivalent to axis error $\gamma$	$\leq \text{TBD}$
Mirror Rotation Period	$\leq \text{TBD}$
Mirror Angular Velocity	$\leq \text{TBD}$
Absolute Position Along-Scan	$\leq \text{TBD}$
Scan Timing and Encoder Errors (dynamic)	$\leq \text{TBD}$

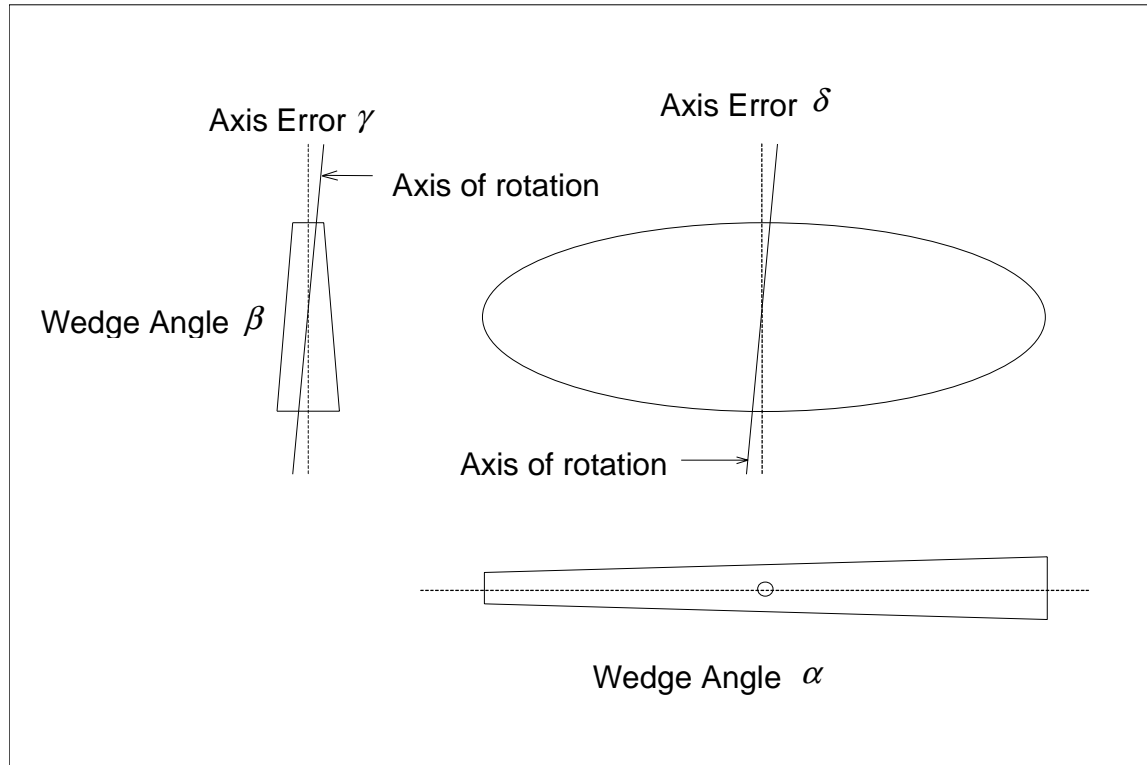


**Figure 3.3-12. Mirror Wedge Angles and Axis Errors Definitions**

The wedge angle  $\alpha$  is the non-parallelism of the half angle mirror in the along-scan axis and creates an along-scan offset between scans from mirror sides 1 and 2. The wedge angle  $\beta$  is the non-parallelism of the mirror in the along-track axis and creates an along-track offset (conical scan). The axis error  $\gamma$  is the misalignment of the mirror center line through the depth of the mirror and the axis of rotation in the along-scan direction. The dynamic along-track axis error is similar but is the dynamic motion caused by the bearings. These axis errors cause a scan-to-scan along-track overlap or under-lap. The axis error  $\delta$  does not have a direct geometric effect. Of these errors, the wedge angles and the non-dynamic axis errors are static errors that will be measured preflight and are not expected to change in-flight. The dynamic along-track axis error will be characterized preflight and may be a function of the mirror angular position.

The normal vectors for each of the half angle mirror surfaces can be determined from these axis and wedge errors. Figure 3.3-13 illustrates the construction of the normal vectors in the scan mirror coordinate system with zero rotation of the mirror. The normal vectors are:

$$\hat{\mathbf{n}}_{\text{side } 1} = \begin{bmatrix} -\sin\left(\frac{\beta}{2} - \gamma\right) \\ \sin\left(\frac{\alpha}{2}\right)\cos\left(\frac{\beta}{2} - \gamma\right) \\ -\cos\left(\frac{\alpha}{2}\right)\cos\left(\frac{\beta}{2} - \gamma\right) \end{bmatrix} \quad (3.3-30)$$

$$\hat{\mathbf{n}}_{\text{side } 2} = \begin{bmatrix} -\sin\left(\frac{\beta}{2} + \gamma\right) \\ \sin\left(\frac{\alpha}{2}\right)\cos\left(\frac{\beta}{2} + \gamma\right) \\ \cos\left(\frac{\alpha}{2}\right)\cos\left(\frac{\beta}{2} + \gamma\right) \end{bmatrix} \quad (3.3-31)$$

These equations assume a sign convention for  $\alpha$ ,  $\beta$  and  $\gamma$  as shown in Figure 3.3-13.

The half angle mirror rotates about the HA mirror coordinate system X axis. The following rotation matrix is used to rotate a mirror normal vector through an angle of  $\theta_{HA}$ .

$$\mathbf{T}_{\text{rot}}(\theta_{HA}) = \begin{bmatrix} 1 & 0 & 0 \\ 0 & \cos(\theta_{HA}) & -\sin(\theta_{HA}) \\ 0 & \sin(\theta_{HA}) & \cos(\theta_{HA}) \end{bmatrix} \quad (3.3-32)$$

Each of the mirror normal vectors is only relevant when the mirror side is facing toward the aft optics and telescope entrance. When the mirror is rotated 0 degrees the line of sight from the aft optics reflected off HA mirror side 1 through the telescope is pointed toward nadir. The following equation is used to compute the HA mirror normal  $\hat{\mathbf{n}}_{HA}$  at any angle  $\theta$  for the appropriate mirror side  $i$ :

$$\hat{\mathbf{n}}_{HA} = \mathbf{T}_{\text{rot}}(\theta_{HA}) \hat{\mathbf{n}}_{\text{side } i} \quad (3.3-33)$$

where  $i=1$  when  $-90^\circ < \theta_{HA} \leq 90^\circ$  and  $i=2$  when  $90^\circ < \theta_{HA} \leq 270^\circ$ . Note that the half angle mirror angle is not directly telemetered so it is assumed to be perfectly synchronized with the telescope. Thus, the half angle mirror angle is taken to be one half the telescope angle.

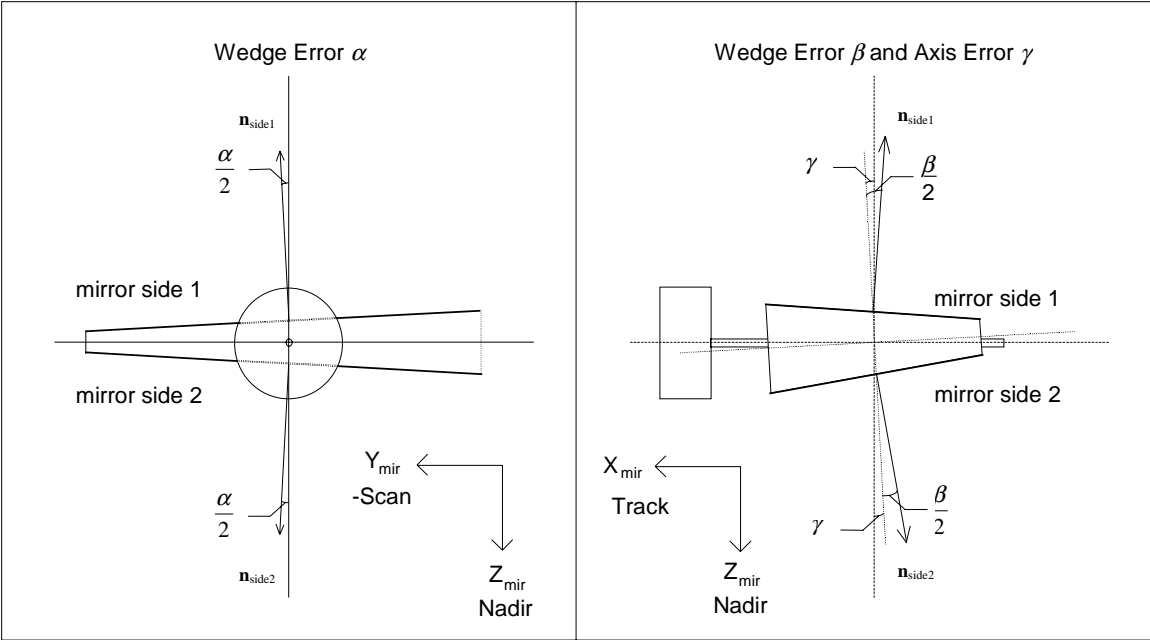


Figure 3.3-13. Half Angle Mirror Normal Vectors

Telescope Encoder Assembly

The telescope encoder assembly measures the telescope and, by inference, half angle mirror position. Constants for the encoder are listed in Table 3.3-5 with derived values in Table 3.3-6.

Table 3.3-5. Telescope Encoder Geometric Constants

Characteristic	Value
Encoder Pulses (per rotation)	TBD
Number of Telescope Time Samples	TBD
Encoder Pulses per Telescope Time Sample	TBD

Table 3.3-6. Telescope Encoder Geometric Derived Values

Characteristic	Derived Value
Rotation per Encoder Pulse	TBD
Rotation per Telescope Time Samples	TBD
Time per Encoder Pulse	TBD
Time per Telescope Time Samples	TBD

The telescope angle  $\theta_T$  (in degrees) versus encoder position  $n_{enc}$  will be measured during preflight testing. SBRS will provide either a parametric model or a set of angles versus encoder number. Until this is available a polynomial model will be used:

$$\theta_T = A_0 + A_1 n_{enc} + A_2 n_{enc}^2 + \dots \quad (3.3-34)$$

and:

$$\theta_{HA} = \frac{1}{2}(\theta_T - \theta_{T0})$$

Where:

$$0 \leq n_{enc} < 16384 \quad (3.3-35)$$

and:

$\theta_{T0}$  is the telescope angle corresponding to nadir pointing.

The time at which every 100<sup>th</sup> (TBD) telescope encoder pulse occurs after the start of the Earth view is transmitted as part of the instrument telemetry. A total of 24 (TBD) telescope time samples, in  $\mu\text{sec}$ , are collected during the Earth view. These relative times  $t_{\text{pulsere}_i}$  must be added to the telemetered Earth view sector start time  $t_{\text{sector}}$  to generate the absolute time samples  $t_{\text{pulse}}$ .

$$t_{\text{pulse}_0} = t_{\text{sector}} \quad (3.3-36)$$

$$t_{\text{pulse}_i} = t_{\text{sector}} + t_{\text{pulsere}_i} \quad i = 1, \dots, 24 \quad (3.3-37)$$

To determine the angle at any time  $t$  after the start of the Earth view it is necessary to interpolate between the encoder times in the spacecraft telemetry. The Chebyshev polynomials interpolation technique will be used in the initial model. A more physically based model may be used in later versions of the software.

Given:

$n_{\text{enc}_0}$  - Encoder position at start of the Earth view sector (fractional)

$t_{\text{pulse}_i}$  - Telescope pulse absolute times;  $i = 0, \dots, 24$

then the encoder locations corresponding to the time samples are:

$$n_{\text{enc}_i} = n_{\text{enc}_0} + 100i \quad (3.3-38)$$

The final encoder interpolation method is still under study. Until this final method is determined, we are using the Chebyshev polynomials. The Chebyshev polynomials  $f_{\text{enc}}$  which will be used to calculate the encoder position  $n_{\text{enc}}$  at time  $t$  is:

$$n_{\text{enc}} = f_{\text{enc}}(t, \mathbf{n}_{\text{enc}}, \mathbf{t}_{\text{pulse}}) \quad (3.3-39)$$

where:

$$\mathbf{n}_{\text{enc}} = [n_{\text{enc}0} \quad \dots \quad n_{\text{enc}24}]^t \quad (3.3-40)$$

$$\mathbf{t}_{\text{pulse}} = [t_{\text{pulse}0} \quad \dots \quad t_{\text{pulse}72}]^t \quad (3.3-41)$$

Figure 3.3-14 illustrates the interpolation of the encoder times. The non-linear motion of the telescope is exaggerated in this figure.

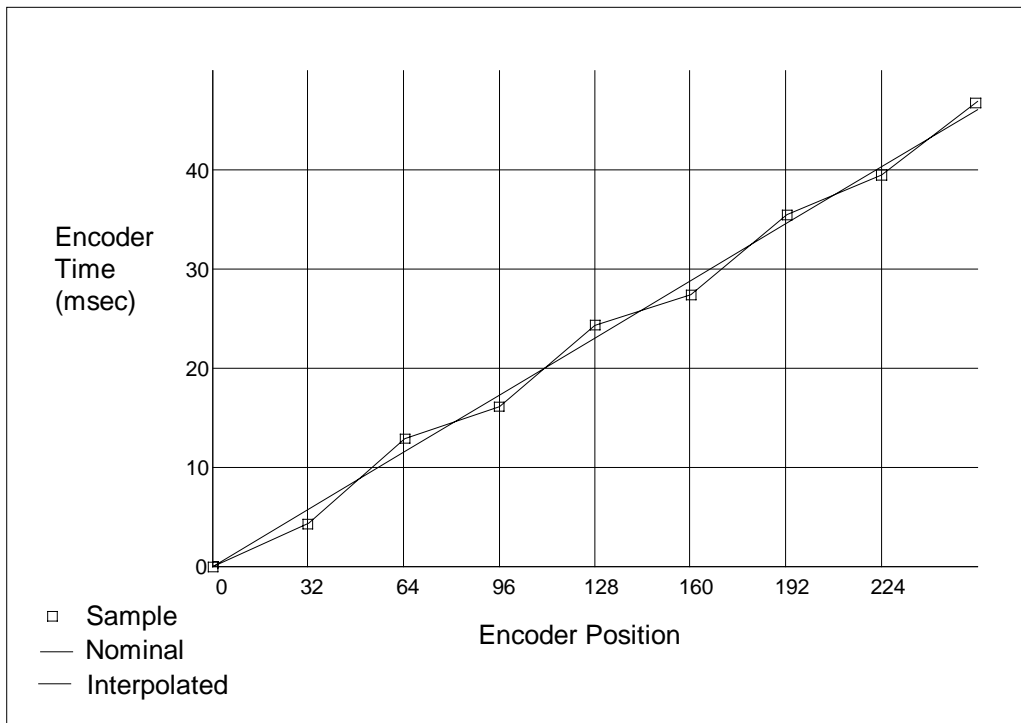


**Figure 3.3-14. Encoder Time Sample Interpolation**

### Telescope Model

The components of the telescope model include two sets of basis vectors: one for the entrance aperture facing the half angle mirror and one for the exit aperture facing the Earth; a magnification factor, and a rotation about the telescope coordinate system X axis. The basic concept of the telescope model is as follows:

1. Construct the entrance and exit aperture basis vectors.
2. Rotate both sets of basis vectors in the telescope coordinate system through the telescope rotation angle.
3. Convert both sets of rotated basis vectors to the instrument coordinate system.

4. Project the viewing vector (after reflection off the half angle mirror) onto the entrance aperture basis vectors by taking scalar (dot) products.
5. Reduce the off-axis (X and Y basis vector terms) components by the magnification factor.
6. Reconstruct the viewing vector using the exit aperture basis vectors.

The exit aperture basis vectors are aligned with the telescope coordinate system axes:

$$\hat{\mathbf{o}}_{outX} = \begin{bmatrix} \cos \delta_T \\ 0 \\ \sin \delta_T \end{bmatrix} \quad \hat{\mathbf{o}}_{outY} = \begin{bmatrix} 0 \\ 1 \\ 0 \end{bmatrix} \quad \hat{\mathbf{o}}_{outZ} = \begin{bmatrix} -\sin \delta_T \\ 0 \\ \cos \delta_T \end{bmatrix}$$

The entrance aperture is rotated by an angle  $\Omega_T$  about the telescope coordinate system Y axis with respect to the exit aperture. This leads to the following entrance aperture basis vectors:

$$\hat{\mathbf{o}}_{inX} = \begin{bmatrix} -\sin(\Omega_T) \\ 0 \\ -\cos(\Omega_T) \end{bmatrix} \quad \hat{\mathbf{o}}_{inY} = \begin{bmatrix} 0 \\ 1 \\ 0 \end{bmatrix} \quad \hat{\mathbf{o}}_{inZ} = \begin{bmatrix} \cos(\Omega_T) \\ 0 \\ -\sin(\Omega_T) \end{bmatrix}$$

The telescope rotation is applied in the same manner as the half angle mirror rotation:

$$\mathbf{T}_T(\theta_T) = \begin{bmatrix} 1 & 0 & 0 \\ 0 & \cos(\theta_T - \theta_{T0}) & -\sin(\theta_T - \theta_{T0}) \\ 0 & \sin(\theta_T - \theta_{T0}) & \cos(\theta_T - \theta_{T0}) \end{bmatrix}$$

Both sets of basis vectors are rotated about the telescope X axis using the  $\mathbf{T}_T$  matrix and then converted to the instrument coordinate system using the telescope to instrument coordinate system transformation matrix  $\mathbf{T}_{inst/tel}$  defined above:

$$\mathbf{M}_{in}(\theta_T) = [\hat{\mathbf{o}}'_{inX} \quad \hat{\mathbf{o}}'_{inY} \quad \hat{\mathbf{o}}'_{inZ}] = \mathbf{T}_{inst/tel} \mathbf{T}_T(\theta_T) [\hat{\mathbf{o}}_{inX} \quad \hat{\mathbf{o}}_{inY} \quad \hat{\mathbf{o}}_{inZ}]$$

The column vectors of matrix  $\mathbf{M}_{in}(\theta_T)$  are the rotated entrance aperture basis vectors in the instrument coordinate system. The exit aperture basis vectors are handled similarly to construct the matrix  $\mathbf{M}_{out}(\theta_T)$ :

$$\mathbf{M}_{out}(\theta_T) = [\hat{\mathbf{o}}'_{outX} \quad \hat{\mathbf{o}}'_{outY} \quad \hat{\mathbf{o}}'_{outZ}] = \mathbf{T}_{inst/tel} \mathbf{T}_T(\theta_T) [\hat{\mathbf{o}}_{outX} \quad \hat{\mathbf{o}}_{outY} \quad \hat{\mathbf{o}}_{outZ}]$$

Note that the exit aperture basis vectors form the identity matrix.

The telescope magnification scales the off-axis components of the viewing vector by the magnification factor  $m$ . The VIIRS magnification factor is 4.

$$\mathbf{M}_{mag} = \begin{bmatrix} \frac{1}{m} & 0 & 0 \\ 0 & \frac{1}{m} & 0 \\ 0 & 0 & 1 \end{bmatrix}$$

### Generation of the Object Viewing Vector

This section summarizes the generation of an object viewing vector. For any focal plane location  $(x,y)$  the following can be used to generate an object space viewing vector  $\mathbf{u}_{inst}$  in the instrument coordinate system at time  $t$ . Typically, the focal plane location will be the center of a spatial element or detector and the time  $t$  will be the time  $t_{center}$  when the center of the sample was imaged.

1. Generate the image space viewing  $\mathbf{u}_{tel}$  in focal plane coordinates from the focal plane location  $(x,y)$  and the focal length  $f$ .

$$\mathbf{u}_{foc} = [x \quad y \quad f]^T \quad (3.3-42)$$

2. Transform the view vector from the focal plane to the aft optics coordinate system:

$$\mathbf{u}_{aft} = \mathbf{T}_{aft/foc} \mathbf{u}_{foc} \quad (3.3-43)$$

- 3 Transfer the viewing vector from the aft optics to instrument coordinate system:

$$\mathbf{u}_{HA} = \mathbf{T}_{inst/aft} \mathbf{u}_{aft} \quad (3.3-44)$$

4. Compute the encoder position  $n_{enc}$  at time  $t$ .

$$n_{enc} = f_{enc}(t, \mathbf{n}_{enc}, \mathbf{t}_{pulse}) \quad (3.3-45)$$

5. Compute the telescope angle  $\theta_T$  from the encoder position  $n_{enc}$ :

$$\theta_T = A_0 + A_1 n_{enc} + A_2 n_{enc}^2 + \dots \quad (3.3-46)$$

6. Compute the half angle mirror angle  $\theta_{HA}$  from the telescope angle:

$$\theta_{HA} = \theta_T / 2$$

7. Compute the half angle mirror normal vector  $\hat{\mathbf{n}}_{HA}$  using the half angle mirror angle  $\theta_{HA}$  and the normal  $\hat{\mathbf{n}}_{side i}$  for the appropriate mirror side  $i$ .

$$\hat{\mathbf{n}}_{HA} = \mathbf{T}_{rot}(\theta_{HA}) \hat{\mathbf{n}}_{side i} \quad (3.3-47)$$

8. Transfer the half angle mirror normal vector from the HA mirror to the instrument coordinate



system and normalize it:

$$\mathbf{n}_{\text{mirr}} = \mathbf{T}_{\text{inst/HA}} \hat{\mathbf{n}}_{\text{HA}} \quad \hat{\mathbf{n}}_{\text{mirr}} = \frac{\mathbf{n}_{\text{mirr}}}{|\mathbf{n}_{\text{mirr}}|} \quad (3.3-48)$$

9. Reflect the viewing vector  $\mathbf{u}_{\text{HA}}$  off the mirror to generate the viewing vector  $\mathbf{u}_{\text{tel}}$  at the telescope entrance aperture:

$$\mathbf{u}_{\text{tel}} = \mathbf{u}_{\text{HA}} - 2\hat{\mathbf{n}}_{\text{mirr}}(\mathbf{u}_{\text{HA}} \cdot \hat{\mathbf{n}}_{\text{mirr}}) \quad (3.3-49)$$

10. Project the incoming viewing vector onto the entrance aperture basis vectors by premultiplying by  $\mathbf{M}_{\text{in}}^T(\theta_T)$ :

$$\mathbf{u}_{\text{in}} = \mathbf{M}_{\text{in}}^T(\theta_T) \mathbf{u}_{\text{tel}}$$

11. Apply the magnification factor and reconstruct the object space viewing vector using  $\mathbf{M}_{\text{out}}(\theta_T)$ :

$$\mathbf{u}_{\text{inst}} = \mathbf{M}_{\text{out}}(\theta_T) \mathbf{M}_{\text{mag}} \mathbf{u}_{\text{in}} = \mathbf{M}_{\text{out}}(\theta_T) \mathbf{M}_{\text{mag}} \mathbf{M}_{\text{in}}^T(\theta_T) \mathbf{u}_{\text{tel}}$$

### 3.3.2.2 Earth Location Algorithm

The VIIRS Earth location algorithm computes the Earth location and other ancillary parameters for a viewing vector. There are three sections describing this calculation: the standard algorithm for intersection with the Earth ellipsoid; the terrain intersection algorithm; and the algorithm to generate the satellite and sun viewing angles and the satellite range.

#### Basic Earth Ellipsoid Intersection Algorithm

Given an object viewing vector  $\mathbf{u}_{\text{inst}}$  in the instrument coordinate system and a corresponding time  $t$ , the basic Earth ellipsoid intersection algorithm proceeds as follows:

1. Compute the required coordinate transformations:
  - 1a. Get instrument-to-spacecraft alignment matrix  $\mathbf{T}_{\text{sc/inst}}$ . [Construct the instrument-to-spacecraft alignment matrix based on the time  $t$  if a time varying model is needed.]
  - 1b. Interpolate the spacecraft attitude to time  $t$  and construct the spacecraft to orbital coordinate transformation matrix  $\mathbf{T}_{\text{orb/sc}}$ .
  - 1c. Interpolate the ECI spacecraft position  $\mathbf{P}_{\text{eci}}$  and velocity  $\mathbf{V}_{\text{eci}}$  to time  $t$  and construct the orbital to ECI transformation matrix  $\mathbf{T}_{\text{eci/orb}}$ .
  - 1d. Construct the ECI to ECR rotation matrix  $\mathbf{T}_{\text{ecr/eci}}$  from the sampling time  $t$ .
  - 1e. Construct the composite transformation matrix:

$$\mathbf{T}_{\text{ecr/inst}} = \mathbf{T}_{\text{ecr/eci}} \mathbf{T}_{\text{eci/orb}} \mathbf{T}_{\text{orb/sc}} \mathbf{T}_{\text{sc/inst}} \quad (3.3-50)$$

2. Transform the viewing vector and spacecraft position vector to the ECR coordinate system:

- 2a. Rotate the viewing vector  $\mathbf{u}_{\text{inst}}$  to the ECR coordinate system:

$$\mathbf{u}_{\text{ecr}} = \mathbf{T}_{\text{ecr/inst}} \mathbf{u}_{\text{inst}} \quad (3.3-51)$$

- 2b. Rotate the spacecraft position vector to the ECR coordinate system:

$$\mathbf{p}_{\text{ecr}} = \mathbf{T}_{\text{ecr/eci}} \mathbf{p}_{\text{eci}} \quad (3.3-52)$$

3. Intersect the ECR viewing vector with the WGS84 Earth ellipsoid (Figure 3.3-15):

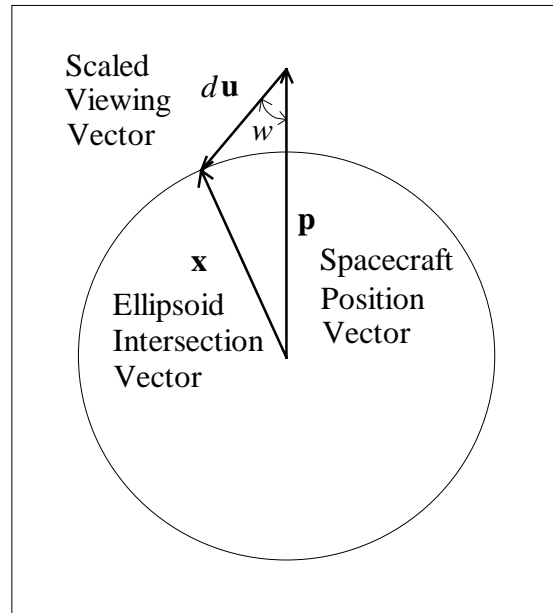


**Figure 3.3-15. Ellipsoidal Viewing Vector Intersection**

Note: These equations do not account for light travel time or aberration due to spacecraft motion or relativistic effects. These effects cause a systematic bias of 7 m at nadir and 14 m at the edges of the scans.

- 3a. Re-scale the viewing vector and satellite vector using the ellipsoid semi-major  $a$  and semi-minor  $b$  axis dimensions ( $a, a, b$ ):

$$\mathbf{u}' = \begin{bmatrix} u_1 / a \\ u_2 / a \\ u_3 / b \end{bmatrix} \quad \mathbf{p}' = \begin{bmatrix} p_1 / a \\ p_2 / a \\ p_3 / b \end{bmatrix} \quad (3.3-53)$$

Note:

$$\mathbf{x}' = \begin{bmatrix} x_1 / a \\ x_2 / a \\ x_3 / b \end{bmatrix} \quad - \text{ the unknown ground point vector (re-scaled)} \quad (3.3-54)$$

3b. Solve for the scaling  $d$  of  $\mathbf{u}'$  which intersects the unit sphere:

From the law of cosines:

$$|\mathbf{x}'|^2 = |d\mathbf{u}'|^2 + |\mathbf{p}'|^2 - 2|d\mathbf{u}'||\mathbf{p}'|\cos(w) \quad (3.3-55)$$

Using the dot-product, the cosine of the acute angle  $w$  between  $\mathbf{u}'$  and  $-\mathbf{p}'$  is:

$$\cos(w) = -(\mathbf{u}' \cdot \mathbf{p}') / (|\mathbf{u}'||\mathbf{p}'|) \quad (3.3-56)$$

By definition  $|\mathbf{x}'| = 1$  so:

$$1 = d^2|\mathbf{u}'|^2 + |\mathbf{p}'|^2 + 2d|\mathbf{u}'||\mathbf{p}'|(\mathbf{u}' \cdot \mathbf{p}') / (|\mathbf{u}'||\mathbf{p}'|) \quad (3.3-57)$$

Simplifying and rearranging:

$$d^2|\mathbf{u}'|^2 + 2d(\mathbf{u}' \cdot \mathbf{p}') + |\mathbf{p}'|^2 - 1 = 0 \quad (3.3-58)$$

This can be solved for  $d$  using the quadratic formula:

$$d = \frac{-(\mathbf{u}' \cdot \mathbf{p}') - \sqrt{(\mathbf{u}' \cdot \mathbf{p}')^2 - |\mathbf{u}'|^2(|\mathbf{p}'|^2 - 1)}}{|\mathbf{u}'|^2} \quad (3.3-59)$$

This is the smaller of the two solutions for  $d$ , the intersection closest to the satellite. If the solution is not real, then there is no intersection.

3c. Use  $d$  to compute  $\mathbf{x}'$  and  $\mathbf{x}$ :

$$\mathbf{x}' = \mathbf{p}' + d\mathbf{u}' \quad (3.3-60)$$

$$\mathbf{x} = \begin{bmatrix} x'_1 a \\ x'_2 a \\ x'_3 b \end{bmatrix} = \begin{bmatrix} (p'_1 + d u'_1) a \\ (p'_2 + d u'_2) a \\ (p'_3 + d u'_3) b \end{bmatrix} = \begin{bmatrix} p'_1 a + d u'_1 a \\ p'_2 a + d u'_2 a \\ p'_3 b + d u'_3 b \end{bmatrix} \quad (3.3-61)$$

$$\mathbf{x} = \mathbf{p} + d\mathbf{u} \quad (3.3-62)$$

4. Convert the ECR ellipsoid pierce point to geodetic coordinates (special case direct

solution):

$$\text{lon} = \tan^{-1}\left(\frac{x_2}{x_1}\right) \quad (3.3-63)$$

$$\text{lat} = \tan^{-1}\left(\frac{x_3/(1-e^2)}{\sqrt{x_1^2 + x_2^2}}\right) \quad (3.3-64)$$

$$h = 0 \quad (3.3-65)$$

### Terrain Intersection Algorithm

The terrain intersection algorithm refines the earth ellipsoid intersection to account for the local terrain parallax. The method uses the ECR coordinate system and geodetic coordinate system and obtains geodetic coordinates where the view vector from the satellite intersects the terrain.

1. Compute the local ellipsoid normal unit vector from the geodetic latitude and longitude:

$$\hat{\mathbf{n}} = \begin{bmatrix} \cos(\text{lat}) \cos(\text{lon}) \\ \cos(\text{lat}) \sin(\text{lon}) \\ \sin(\text{lat}) \end{bmatrix} \quad (3.3-66)$$

at  $\mathbf{x}$  on the Earth ellipsoid.

2. Compute the ECR unit vector from the ground point  $\mathbf{x}$  to the satellite:

$$\hat{\mathbf{u}} = -\frac{\mathbf{u}}{|\mathbf{u}|} \quad (3.3-67)$$

3. Compute the component of the satellite vector which is in the local vertical direction:

$$\cos \nu = \hat{\mathbf{u}} \cdot \hat{\mathbf{n}} \quad (3.3-68)$$

4. Compute the distance along the satellite vector ( $D_{\max}$ ) we must move to achieve a height of  $H_{\max}$  where  $H_{\max}$  is a pre-computed value representing the highest local terrain height:

$$D_{\max} = \frac{H_{\max}}{\cos \nu} \quad (3.3-69)$$

5. Compute the ECR coordinates of the point along the viewing vector that corresponds to  $H_{\max}$ :

$$\mathbf{x}_{\max} = \mathbf{x} + D_{\max} \hat{\mathbf{u}} \quad (3.3-70)$$

6. Compute the distance along the satellite vector ( $D_{\min}$ ) we must move to achieve a height

of  $H_{\min}$  where  $H_{\min}$  is a pre-computed value representing the lowest local terrain height:

$$D_{\min} = \frac{H_{\min}}{\cos \nu} \quad (3.3-71)$$

7. Compute the ECR coordinates of the point along the viewing vector that corresponds to  $H_{\min}$ :

$$\mathbf{x}_{\min} = \mathbf{x} + D_{\min} \hat{\mathbf{u}} \quad (3.3-72)$$

8. Convert  $\mathbf{x}_{\max}$  to geodetic coordinates (iterative general solution), with coordinates  $(\phi_{\max}, \lambda_{\max}, H_{\max})$ ,

9. Define points  $\mathbf{s}_{\max}$  on the ellipsoidal surface from point  $\mathbf{x}_{\max}$  by:

$$(\phi_{\max}, \lambda_{\max}, 0)$$

10. Perform terrain intersection iterations (see Figure 3.3-16):

$$\mathbf{s}_0 = \mathbf{s}_{\max} = (\phi_{\max}, \lambda_{\max}, 0) \quad - \text{ (Geodetic coordinates)} \quad (3.3-73)$$

$$h_0 = \text{DEM}(\mathbf{s}_0) \quad - \text{ (DEM at } \mathbf{s}_0) \quad (3.3-74)$$

$$h'_0 = H_{\max} \quad (3.3-75)$$

$$ds = (\text{nominally } 1/2 \text{ km}) \quad (3.3-76)$$

$$dD = \frac{ds}{\sin \nu} \quad (3.3-77)$$

$$i = 0 \quad (3.3-78)$$

$$D_0 = D_{\max} \quad (3.3-79)$$

$$\text{do until } (h_i \geq h'_i) \quad (3.3-80)$$

$$i = i + 1 \quad (3.3-81)$$

$$D_i = D_{i-1} - dD \quad (3.3-82)$$

$$\mathbf{x}_i = \mathbf{x} + D_i \hat{\mathbf{u}} \quad (3.3-83)$$

$$\mathbf{x}_i \Rightarrow (\phi_i, \lambda_i, h'_i) \quad - \text{ (Convert from ECR to geodetic)} \quad (3.3-84)$$

$$\mathbf{s}_i = (\phi_i, \lambda_i, 0) \quad (3.3-85)$$

$$h_i = \text{DEM}(\mathbf{s}_i) \quad (3.3-86)$$

end do

$$D = D_i \quad (3.3-87)$$

11. Compute the precise terrain intersection from the last two iterations:

The final terrain intersection height can be expressed:

$$h_{\text{final}} = \alpha h_i + (1 - \alpha) h_{i-1} = \alpha h'_i + (1 - \alpha) h'_{i-1} \quad (3.3-88)$$

Solving for the weights:

$$\alpha = \frac{h'_{i-1} - h_{i-1}}{h_i - h_{i-1} - dh'} \quad (3.3-89)$$

$$1 - \alpha = \frac{h_i - h'_i}{h_i - h_{i-1} - dh'}$$

The final position is:

$$D_{\text{final}} = D + (1 - \alpha) dD \quad (3.3-90)$$

$$\begin{aligned} \bar{\mathbf{x}} &= \mathbf{x} + D_{\text{final}} \hat{\mathbf{u}} \\ &\Rightarrow (\phi_{\text{final}}, \lambda_{\text{final}}, h') \end{aligned} \quad \text{- (Convert from ECR to geodetic)} \quad (3.3-91)$$

$$h_{\text{final}} = \alpha h_i + (1 - \alpha) h_{i-1} \quad (3.3-92)$$

12. Final geodetic coordinates (*lat, lon, height*) on the terrain are given by  $(\phi_{\text{final}}, \lambda_{\text{final}}, h_{\text{final}})$ .

Care must be taken, so that *ds* is in sync. with the resolution of the DEM; otherwise tops of steep mountains at large scan angles might be missed.

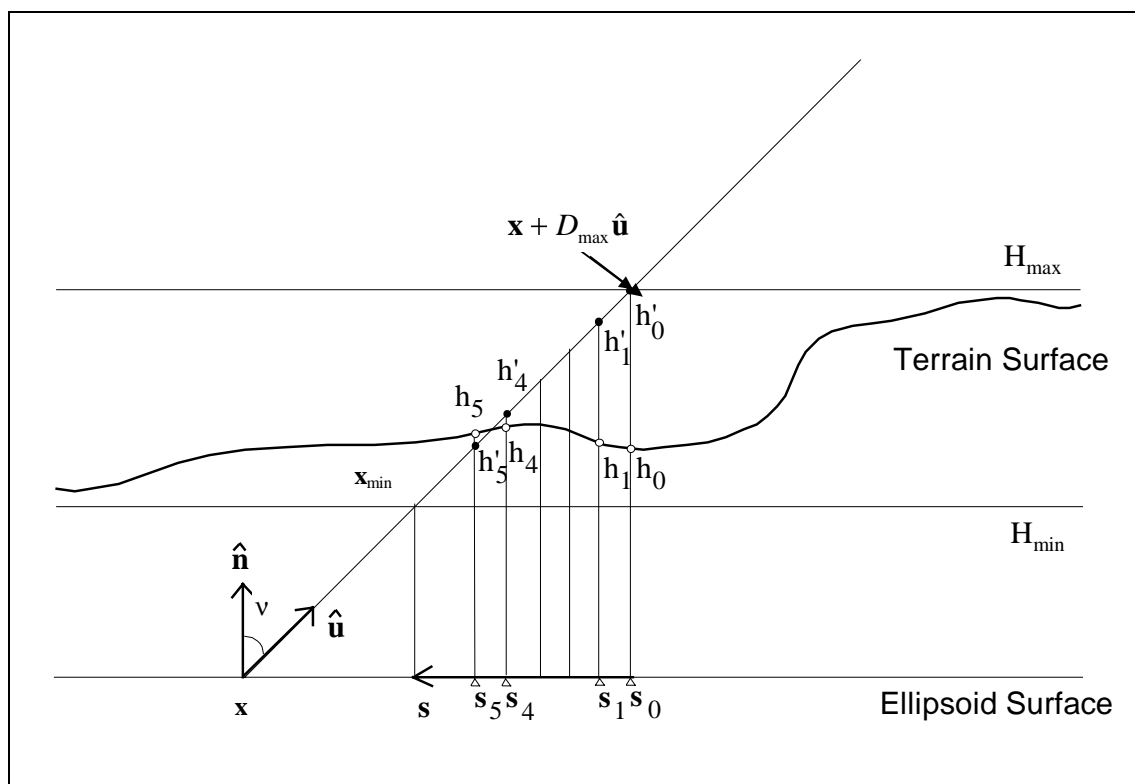


**Figure 3.3-16. Terrain Intersection Search Geometry**

The database used for performing the terrain correction is the 3 arc-second DEM generated from the Shuttle Radar Topography Mission (SRTM) supplemented by the GTOPO30 data set where SRTM coverage is unavailable. Height information is retrieved from the DEM database by performing linear interpolation to the specified geographic location from the four nearest-neighbor DEM data points. The DEM values are given over a geoid model and values from the Toolkit must be adjusted with the geoid to obtain the height values over the WGS84 ellipsoid.

It should be noted that the terrain correction will not be performed if the sensor zenith angle  $v$  (angle between  $\hat{n}$  and  $\hat{u}$ ) is greater than 85 degrees, which only occurs during the spacecraft maneuvers.

The use of alternative methods can be used to find the final geodetic coordinates simplifying some of the above processing.

### Computing Additional Parameters

The remaining Earth location parameters can now be calculated from the final geodetic coordinates. These parameters are the zenith and azimuth angles to the satellite, the range to the satellite and the zenith and azimuth angles to the Sun. Also the sun vector from the satellite is provided in addition to the lunar vector. The solar and lunar vectors are useful in the instrument calibration.

Given the final geodetic position latitude, longitude and height  $(\varphi, \lambda, h)$ , ECR coordinates  $(x, y, z)$  ( $= \mathbf{X}_{ecr}$ ) can be expressed (as given at the beginning of section 3.3.1) by:

$$x = (N + h) \cos \varphi \cos \lambda \quad (3.3-93)$$

$$y = (N + h) \cos \varphi \sin \lambda \quad (3.3-94)$$

$$z = (N(1 - e^2) + h) \sin \varphi \quad (3.3-95)$$

$$N = a / (1 - e^2 \sin^2 \varphi)^{1/2} \quad (3.3-96)$$

$$e^2 = 1 - \frac{b^2}{a^2}$$

1. Compute the unit normal vector  $\hat{\mathbf{n}}$  at the final geodetic position  $(\varphi, \lambda, h)$  by differentiating equations (3.3-93), (3.3-94), and (3.3-95) with respect to  $h$  and evaluate at  $(\varphi, \lambda, h)$ :

$$\hat{\mathbf{n}} = \begin{bmatrix} \cos(\varphi) \cos(\lambda) \\ \cos(\varphi) \sin(\lambda) \\ \sin(\varphi) \end{bmatrix} \quad (3.3-97)$$

2. Compute a unit vector  $\hat{\mathbf{E}}$  in the east direction at the geodetic position by differentiating equations (3.3-93), (2), and (3) with respect to  $\lambda$  and evaluate at the position:

$$\hat{\mathbf{E}} = \begin{bmatrix} -\sin \lambda \\ \cos \lambda \\ 0 \end{bmatrix} \quad (3.3-98)$$

3. Compute a unit vector  $\hat{\mathbf{N}}$  in the north direction at the geodetic position by computing the cross product of  $\hat{\mathbf{n}}$  and  $\hat{\mathbf{E}}$ :

$$\hat{\mathbf{N}} = \hat{\mathbf{n}} \times \hat{\mathbf{E}} \quad (3.3-99)$$

4. Generate the range to the spacecraft  $r_{sc}$  and the ground to spacecraft unit vector  $\mathbf{v}_{sc}$ :

$$\mathbf{v}_{sc} = \mathbf{p}_{ecr} - \mathbf{x}_{ecr} \quad (3.3-100)$$

$$r_{sc} = |\mathbf{v}_{sc}|$$

$$\hat{\mathbf{v}}_{sc} = \frac{1}{r_{sc}} \mathbf{v}_{sc}$$



5. The zenith angle  $\zeta_{sc}$  is the angle between the spacecraft view vector and the normal:

$$\cos(\zeta_{sc}) = \hat{\mathbf{n}} \cdot \hat{\mathbf{v}}_{sc} \quad (3.3-101)$$

6. Compute the azimuth angle  $\alpha_{sc}$ :

- 6a. Compute two directional cosines by:

$$l = \mathbf{v}_{sc} \cdot \hat{\mathbf{E}}m = \mathbf{v}_{sc} \cdot \hat{\mathbf{N}} \quad (3.3-102)$$

- 6b. Using the following relationship between the azimuth angle and the directional cosines  $l$  and  $m$ , determine the angle.

$$\tan(\alpha_{sc}) = \frac{l}{m} \quad (3.3-103)$$

7. The following steps are used to generate the solar vectors from the ground and from the instrument after retrieving the ECI solar vector  $\mathbf{s}_{eci}$  based on the imaging time  $t$ .

- 7a. In the ECR coordinate system, rotate the solar vector at time  $t$  by:

$$\mathbf{s}_{ecr} = \mathbf{T}_{ecr/eci} \mathbf{s}_{eci} \quad (3.3-104)$$

For the solar zenith and azimuth angles, use steps 5 and 6.

- 7b. In the instrument coordinate system,

$$\mathbf{s}_{inst} = \mathbf{T}_{inst/sc} \mathbf{T}_{sc/orb} \mathbf{T}_{orb/eci} \mathbf{s}_{eci} \quad (3.3-105)$$

8. The following steps are used to generate the lunar vector  $\mathbf{m}_{inst}$  from the spacecraft in the instrument coordinate system after retrieving the ECI lunar vector  $\mathbf{m}_{eci}$  based on the time  $t$ .

In the instrument coordinate system,

$$\mathbf{m}_{inst} = \mathbf{T}_{inst/sc} \mathbf{T}_{sc/orb} \mathbf{T}_{orb/eci} \mathbf{m}_{eci} \quad (3.3-106)$$

### 3.3.3 Archived Algorithm Output

The Earth location algorithm creates eight output fields for each VIIRS spatial element: geodetic latitude, geodetic longitude, height above the Earth ellipsoid, satellite zenith angle, satellite azimuth, range to the satellite, solar zenith angle, and solar azimuth. Since a VIIRS scan contains  $2954 \times 16 = 47264$  spatial elements this yields 378112 fields per scan. These fields are archived for every VIIRS Level 1A product. Six additional fields: the three element solar and lunar vectors in the instrument coordinate system can also be computed as described above, when necessary to support calibration activities, but would not need to be archived for every data product.

### 3.4 ERROR ANALYSIS AND SENSITIVITY STUDIES

#### 3.4.1 Variance or Uncertainty Estimates

The fundamental measure of uncertainty of interest for the Earth location algorithm is the locational accuracy of the geodetic coordinates computed for each spatial element. This accuracy is limited by the uncertainty in the spacecraft, instrument, and elevation data provided to the algorithm.

An analysis of VIIRS Earth location error is presented in this and the following sections. This analysis includes a detailed breakdown of the anticipated sources of error in the NPOESS spacecraft ephemeris and attitude knowledge, and in the VIIRS instrument pointing knowledge. It also demonstrates the effects these errors and errors in the ancillary digital elevation data have on the resulting data product Earth location accuracy. The current best estimates of the contributing errors from the VIIRS instrument error budget were used in conjunction with the spacecraft specification requirements for this analysis.

The sensitivity of the output product accuracy to the uncertainty in the input data varies with scan angle. Plots depicting this sensitivity for spacecraft position, spacecraft attitude pointing, and instrument pointing knowledge errors are presented in Section 3.4.2.

The three error components, spacecraft position, spacecraft attitude, and instrument pointing knowledge, were analyzed separately with all contributing errors classified as either static or dynamic. Static errors are unknown constant or repeatable periodic offsets caused by imprecise knowledge of the instrument or spacecraft geometry, or by geometric distortions occurring before or in-flight. These error components, though initially unknown, should not change with time in-flight. Estimates of these constant offsets or biases will be computed using the geometric parameter estimation and algorithm verification procedures described in Section 3.6.1. The dynamic error components are time varying and cannot be easily modeled. Tables detailing the various error sources and their expected magnitudes are presented in Section 3.4.3. Tables 3.4-1, 3.4-2, and 3.4-3 summarize the impact on Earth location of the various error sources. Two cases are shown in each table: the current design before on-orbit calibration case; and the after on-orbit calibration case. Table 3.4-4 shows the combined effect (Root Sum Square (RSS)) of all of the components.

**Table 3.4-1. Geolocation Impact of 3 Sigma Spacecraft Position Errors**

Spacecraft Position	X-Axis Platform Position Error	Corresponding Along-Track Earth Location Error		Y-Axis Platform Position Error	Corresponding Along-Scan Earth Location Error		Z-Axis Platform Position Error	Corresponding Along-Scan Earth Location Error	
		scan = 0°	scan = 55°		scan = 0°	scan = 55°		scan = 0°	scan = 55°
Before Calibration	75.0 m	66.4 m	64.5 m	75.0 m	66.4 m	66.4 m	75.0 m	0.0 m	177.9 m
After Calibration	75.0 m	66.4 m	64.5 m	75.0 m	66.4 m	66.4 m	75.0 m	0.0 m	177.9 m

**Table 3.4-2. Geolocation Impact of 3 Sigma NPOESS Platform Attitude Knowledge Error Components**

Platform Attitude	Roll Pointing Error	Corresponding Along-Scan Earth Location Error		Pitch Pointing Error	Corresponding Along-Track Earth Location Error		Yaw Pointing Error	Corresponding Along-Track Earth Location Error	
		scan = 0°	scan = 55°		scan = 0°	scan = 55°		scan = 0°	scan = 55°
Before Calibration	56.7 arcsec	228.2 m	1417.4 m	67.7 arcsec	272.4 m	330.6 m	61.6 arcsec	0.0 m	446.3 m
After Calibration	36.8 arcsec	148.1 m	919.7 m	36.8 arcsec	148.1 m	179.7 m	36.8 arcsec	0.0 m	266.5 m

**Table 3.4-3. Geolocation Impact of 3 Sigma Instrument Pointing Knowledge Error Components**

Instrument Pointing	Roll Pointing Error	Corresponding Along-Scan Earth Location Error		Pitch Pointing Error	Corresponding Along-Track Earth Location Error		Yaw Pointing Error	Corresponding Along-Track Earth Location Error	
		scan = 0°	scan = 55°		scan = 0°	scan = 55°		scan = 0°	scan = 55°
Before Calibration	144.7 arcsec	582.3 m	3616.1 m	144.7 arcsec	582.1 m	706.5 m	154.5 arcsec	0.0 m	1118.9 m
After Calibration	27.6 arcsec	111.2 m	690.4 m	29.6 arcsec	119.0 m	144.4 m	31.9 arcsec	0.0 m	230.6 m

**Table 3.4-4. Total Combined 3 Sigma RSS Geolocation Error**

	Total RSS Along-Scan Earth Location Error (3 sigma)  (Y-Axis Spacecraft Position) (Z-Axis Spacecraft Position) (Platform Roll) (Instrument Roll)		Total RSS Along-Track Earth Location Error (3 sigma)  (X-Axis Spacecraft Position) (Platform Pitch) (Instrument Pitch) (Platform Yaw) (Instrument Yaw)		Equivalent Circular Error (3 sigma)  (Equal Area Circle Radius)	
	scan = 0°	scan = 55°	scan = 0°	scan = 55°	scan = 0°	scan = 55°
Before Calibration	628.9 m	3888.6 m	646.1 m	1436.6 m	637.5 m	2363.5 m
After Calibration	196.7 m	1165.6 m	201.2 m	426.1 m	199.0 m	704.7 m

Figure 3.4-1 and 3.4-2 show these combined Earth location errors graphically. In the first figure, the four error ellipses correspond to the two cases at two different scan angles, 0 and 55 deg with the error given in meters. The second figure shows plots of Earth location error growth, in the

along-track and across-track directions, as a function of distance from nadir for the after calibration case.

The accuracy impact of the digital elevation data is also a function of scan angle with no effect on Earth location at nadir and a greater than one-to-one correspondence between height and position errors at high scan angles. Figure 3.4-3 shows the impact of two different terrain accuracies on the Earth location accuracy in fractions of a pixel (in the along-scan direction). The discontinuities in these plots are due to the changes in pixel aggregation factor in the along-scan direction. In each graph, the Earth location error in pixel fraction reaches a peak and drops down after that point. Although both the Earth location error and ground pixel size increase as the scan angle increases, the rate of increase in the pixel size is slower than the rate of increase in the Earth location error close to nadir, but becomes faster at higher scan angles where the ratio begins to decrease. See Figure 3.3-1 for growth of the pixel size on the ground. In the context of image-to-image registration, the displacement due to terrain errors is self-canceling if the two data sets are taken from approximately the same viewing geometry but are arithmetically added if the views are from different directions. The effect of the input elevation model on the product accuracy is further complicated by the relationship between elevation accuracy and terrain roughness. In rugged areas, elevation variations of hundreds of meters can occur within a single VIIRS spatial element. Assigning a single geodetic coordinate to such a spatial element using a representative elevation masks the true complexity of the terrain and the real differences in what is being viewed from different directions.

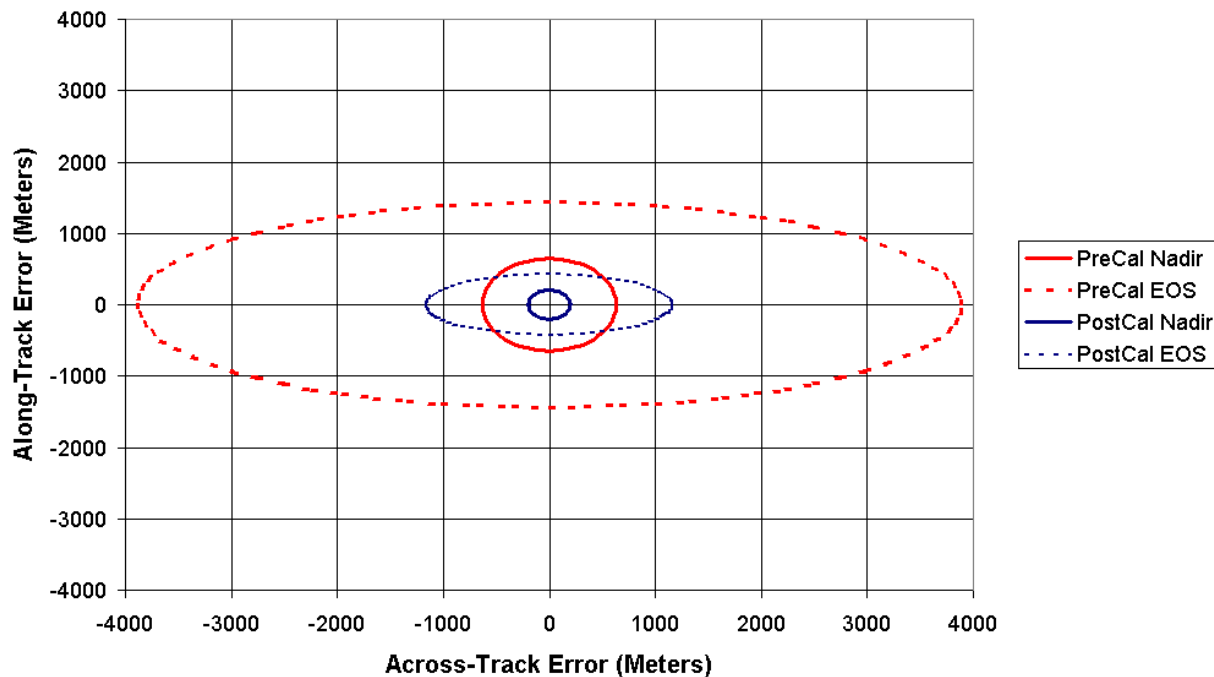


**Figure 3.4-1. 3-Sigma Earth Location Error (Meters)**

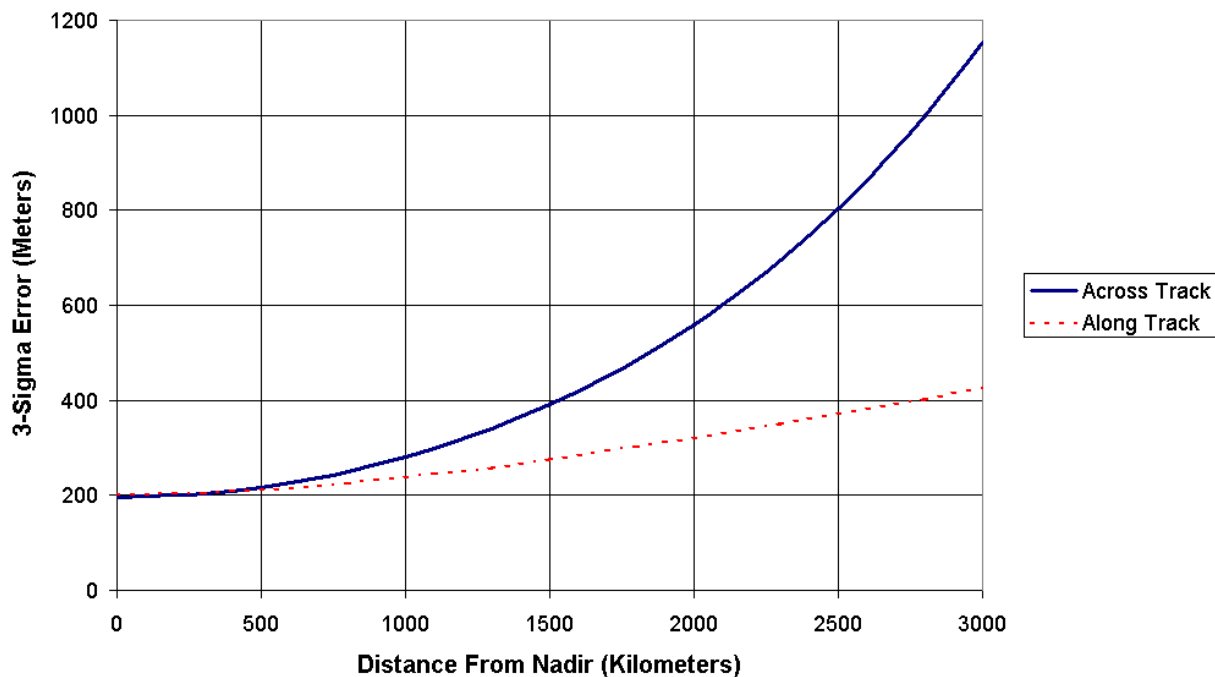


Figure 3.4-2. Earth Location Error Growth

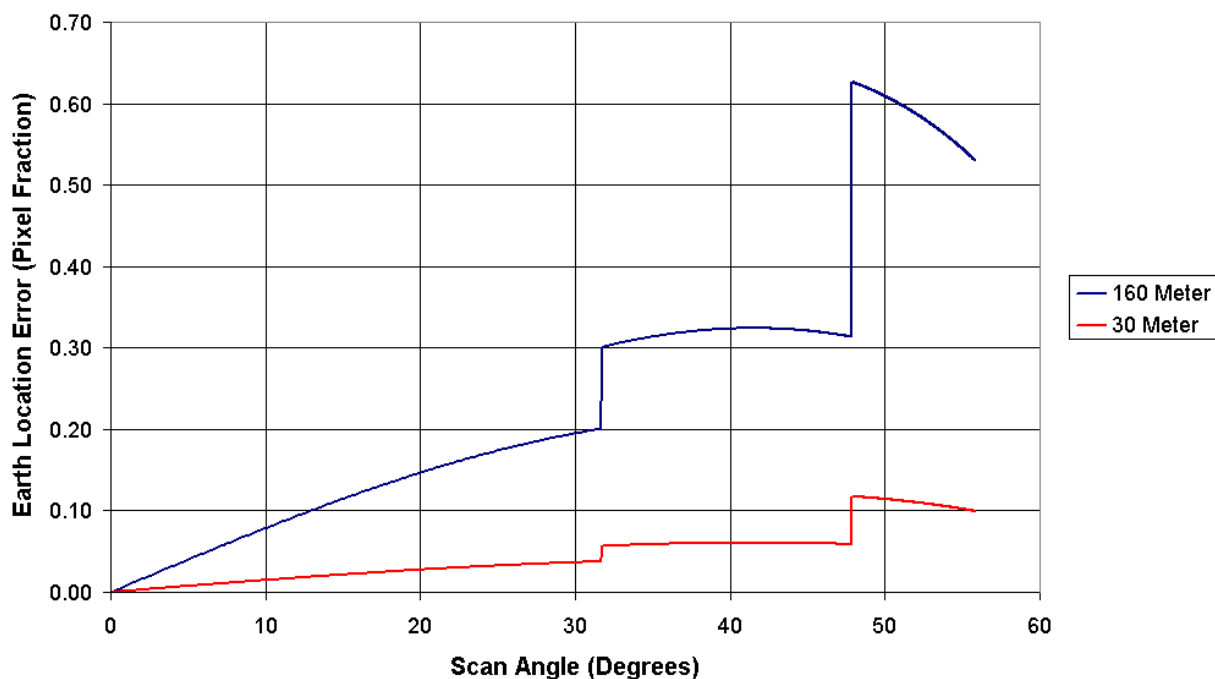


Figure 3.4-3. Earth Location Error (in imaging band pixel fraction) Resulting from Various Terrain Height Errors as a Function of Scan Angle

Section 3.4.2 relates Platform position, Platform attitude, and Instrument pointing errors to Earth location error. The distortion (or growth) of VIIRS pixels as a function of scan angle is also shown. Section 3.4.3 describes the position and attitude errors specific to the NPOESS Platform and the pointing errors specific to the VIIRS Instrument. Two sets of data are provided. The first is the current at-launch error budget specification limit for each type of error. This is followed by an estimate of actual on-orbit performance following a post-launch calibration activity. The error estimates are separated into component parts and characterized as being either static or dynamic in nature. Section 3.4.4 presents the total combined Earth location error due to specific NPOESS Platform and VIIRS Instrument position, attitude, and pointing errors. Earth location error summary information is presented for both the at-launch and post-calibration Platform/Instrument scenarios:

- Platform/Instrument errors are at the at-launch specification (or spec) limits
- Platform/Instrument errors are at the reduced estimates based on the degree to which ground processing is able to remove static error components.

Section 3.4.6 provides more details on ground processing, the approach, error characteristics, and limitations. Section 3.4.7 contains a discussion of the effect of inadequate terrain height information on pixel location as a function of scan angle. Section 3.4.8 discusses the minimum scan angle required for complete global coverage as a function of number of days per repeat cycle and latitude of the area in question. Section 3.4.9 contains the current band to band registration specification, contractor goals, and current estimates. In addition the impact of band to band misregistration is discussed. A concluding summary is provided in Section 3.4.10. Section 3.4.5 contains a description of the equations that were used and some comments on the statistical simplifications used in this analysis.

### 3.4.2 Earth Location Sensitivity to Position/Pointing Error

This section will relate the units of spacecraft position error (meters in space) and platform attitude/instrument pointing error (arc seconds) to absolute geolocation error (meters on the ground). Earth location errors are scan angle dependent, growing larger with increasing scan (or view) angle. A prefacing section describes the corresponding growth of the viewed ground pixel, which also increases in size with increasing scan angle.

#### 3.4.2.1 Pixel and Scan Growth as a Function of Scan Angle

Figure 3.3-1 depicts the growth of a radiometric band pixel as a function of scan angle. In the figure the lighter continuous line shows along-track growth while the darker line depicts cross-track growth. For example a radiometric band pixel viewed at a scan angle of 55.84 degrees would have dimensions of 1.60 kilometers cross-track by 1.60 kilometers along-track. The discontinuities in the cross-track plot are due to the changes in pixel aggregation described in section 3.3. Many of the plots that follow show increasing absolute geolocation error for increasing scan angle. However, pixel size is also (piece-wise) increasing and thus the error expressed as a pixel fraction is less variable.

Since the VIIRS along-track field of view is designed to collect sixteen radiometric band pixels at one time, the along-track dimension of the VIIRS scan also grows as a function of scan angle from 11.87 kilometers at nadir to 25.60 kilometers at a scan angle of 55.84 degrees. This leads to the so-called "bow tie" effect in the ground projection of a VIIRS scan in which the scan

coverage is wider at the edges than at the center. This effect causes adjacent scans to overlap at high scan angles, with a maximum overlap over 50 percent at 55.84 degrees. This overlap is unaffected by the VIIRS pixel aggregation strategy which applies only in the cross-track direction. The overlap in coverage for two consecutive VIIRS scans is depicted in Figure 2.2-10. The two scans are shown with solid and dashed lines.

Several consequences of this VIIRS imaging geometry should be noted. When viewing VIIRS data in its raw geometric form the images will appear to be discontinuous at the edges where pixels overlap and image features are repeated. This does not affect the Earth location accuracy and the following discussion applies to all VIIRS pixels without regard to how pixels from consecutive scans are spatially related to one another. There is an impact on the way in which VIIRS Earth location data must be computed and stored to correctly represent this geometry.

### 3.4.2.2 Geolocation Sensitivity to Position Error

The relationship between spacecraft position error and Earth location error is shown in Figure 3.4-4. Two assumptions are made to compute these curves. First, the spacecraft altitude (not including Z-Axis displacement) is taken to be 830 kilometers. Second, a spherical Earth model, with a radius of 6378 kilometers, is used. Terrain variation and non-sphericity of the Earth are second order effects for this part of the analysis.

Each curve relates spacecraft position error in meters along a given axis in the Orbital Reference Coordinate Frame to along-track or cross-track Earth location error in meters as a function of scan angle. In this and all subsequent figures, Earth location errors in the along-track direction are depicted by a solid line, while cross-track Earth location errors are depicted by a dotted line with stars. Spacecraft position errors along the Orbital Reference X-Axis contribute geolocation errors only in the along-track direction. Position errors along the Y and Z-axes contribute geolocation errors only in the cross-track direction.

At nadir (scan angle 0 degrees), a 1.0 meter displacement of the spacecraft along the X-Axis causes an Earth location error of 0.885 meters in the along-track direction as does a 1.0 meter Y-Axis displacement but in the cross-track direction. Spacecraft displacement along the Z-Axis does not impact Earth location at nadir.

At a scan angle of 55.84 degrees, a 1.0 meter X-Axis displacement causes a 0.860 meter along-track Earth location error. A 1.0 meter Y-Axis displacement causes a 0.885 meter cross-track Earth location error. Finally, a 1.0 meter spacecraft displacement along the Z-Axis causes a 2.372 meter cross-track Earth location error. The slight downward dip in the X-Axis displacement curve becomes intuitively obvious when one considers the smaller circle the Earth-surface pixel will traverse during a complete orbit at large scan angle, than at nadir.

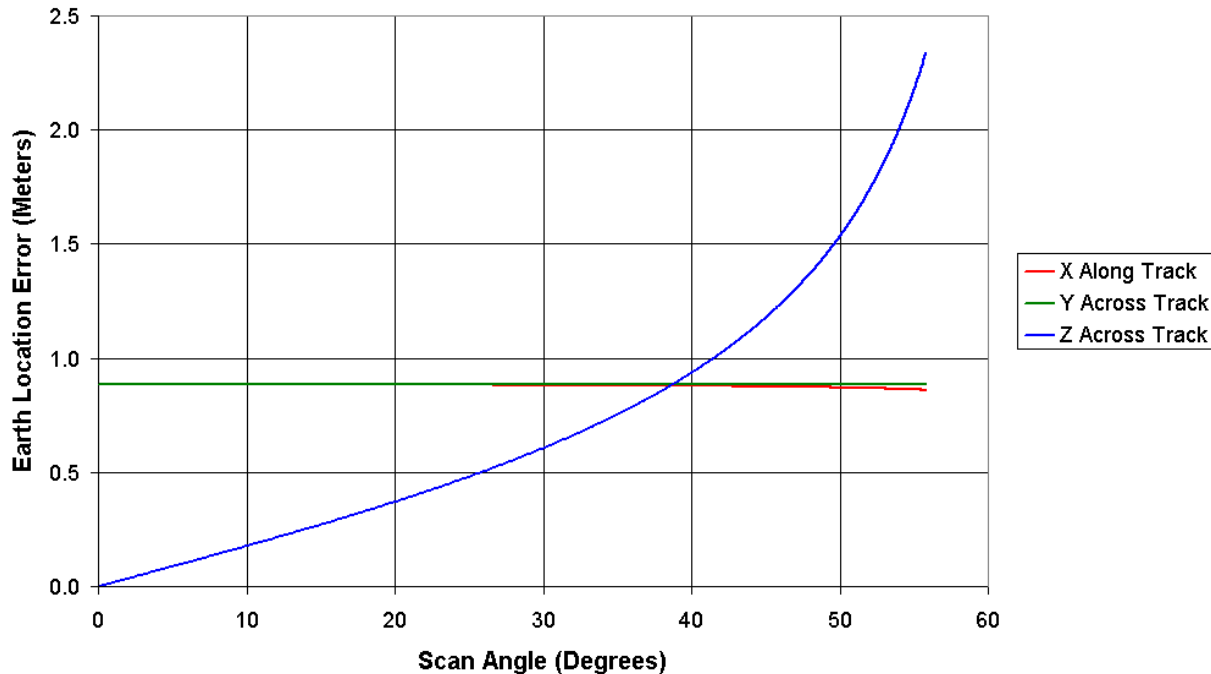


**Figure 3.4-4. Earth Location Error (in meters) resulting from Spacecraft Position Error (in meters) as a Function of Scan Angle**

### 3.4.2.3 Geolocation Sensitivity to Attitude/Pointing Error

The relationship between Platform attitude/Instrument pointing error and Earth location error is shown in Figure 3.4-5. The same assumptions of a spherical earth and a 830 km orbit are made to compute these curves.

Each curve relates attitude/pointing error (in arc-seconds) about a given axis in the Orbital Reference Coordinate Frame to along-track or cross-track Earth location error (in meters) as a function of scan angle. Roll pointing errors contribute geolocation errors only in the cross-track direction. Pitch pointing errors contribute geolocation errors only in the along-track direction. Yaw pointing errors effect geolocation primarily in the along-track direction for small angular displacement.

At nadir, a 1 arc-second error in roll causes an Earth location error of 4.024 meters in the cross-track direction. A 1 arc-second error in pitch also causes a 4.024 meter Earth location error, but in the along-track direction. Errors in yaw pointing do not impact Earth location at nadir.

At a scan angle of 55.84 degrees a 1 arc-second error in roll causes a 24.990 meter cross-track Earth location error. A 1 arc-second error in pitch causes a 4.884 meter along-track Earth location error. Finally, a 1 arc-second error in yaw causes a 7.241 meter Earth location error, primarily in the along-track direction.

The large increase in cross-track Earth location error from roll pointing error at high scan angle corresponds to the cross-track distortion of the pixel at high scan angle (see Figure 3.3-1). So the growth in absolute geolocation error from roll pointing error at high scan angles is partially offset by the increase in pixel size so that the error in terms of pixel fraction is more stable.



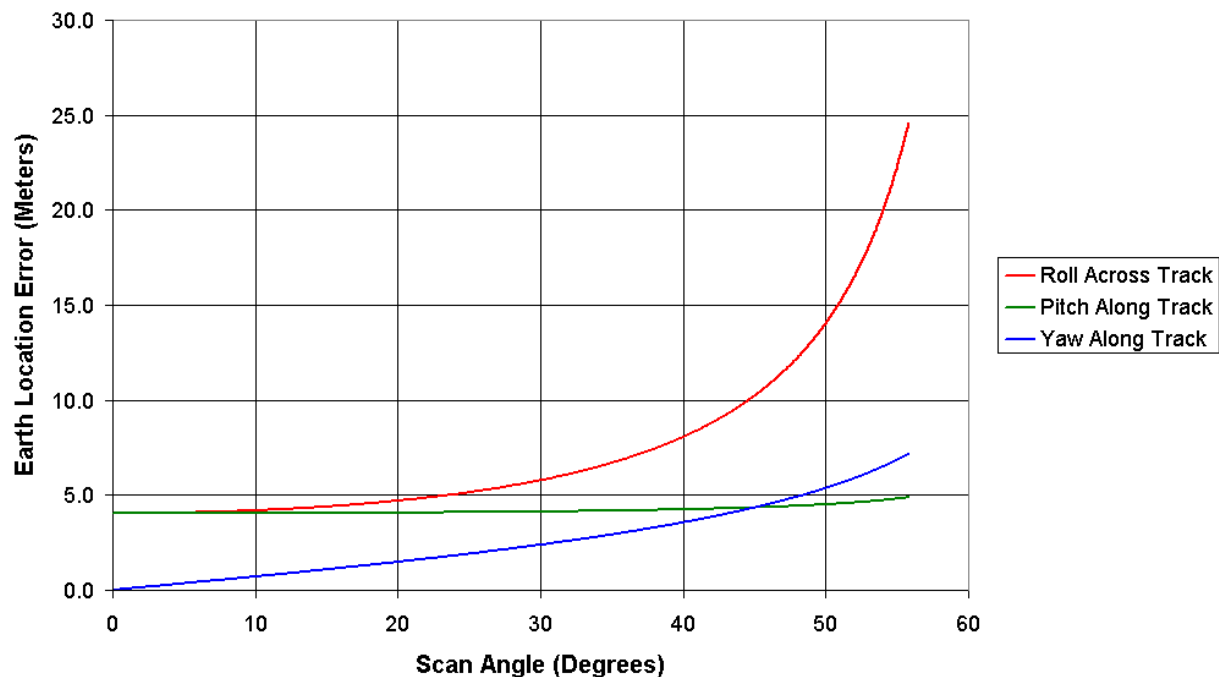


**Figure 3.4-5. Earth Location Error (in meters) resulting from Instrument/Platform Pointing Error (in arcseconds) as a Function of Scan Angle**

### 3.4.3 Position and Attitude Error Specification and Estimation

#### 3.4.3.1 NPOESS Platform Position Error

Platform position errors are specified in meters along 3 axes in the Orbital Reference Coordinate Frame. This coordinate frame moves with the satellite along the space trajectory and defines the orientation of the satellite. The origin of coordinates is at the center of mass of the spacecraft. The positive Z-Axis points from the Spacecraft center of mass to the center of the Earth. The Y-Axis is normal to the Z-Axis and to the Spacecraft's instantaneous velocity vector. The X-Axis completes the right handed set and is positive in the direction of motion of the satellite. Due to orbit eccentricity, the X-Axis and the Spacecraft's instantaneous velocity vector are not generally co-aligned.

Table 3.4-5 shows the current 3 sigma platform position error specification. The source of information is the NPOESS System Requirements Document (SRD).

Assuming a zero-mean Gaussian distribution, the linear (per coordinate axis) position error requirement implies that 99.7% of the observations would have position errors less than the 3 sigma value (75 meters), 95.5% of the observations would have position errors less than the 2 sigma value (50 meters), and 68.3% of the observations would have position errors less than the 1 sigma value (25 meters).

**Table 3.4-5. NPOESS Platform Position 3 sigma Error Specification**

Spacecraft Position Error	X-Axis Position Error Spec	Y-Axis Position Error Spec	Z-Axis Position Error Spec
3 sigma Spec	75.0 meters	75.0 meters	75.0 meters

### 3.4.3.2 NPOESS Platform Attitude Error

Attitude errors are expressed in terms of two components, attitude accuracy and attitude knowledge. Attitude accuracy is a measurement of the angle between the desired and actual orientation of the Orbital Reference Coordinate Frame (described below) about a given axis. Attitude knowledge is the accuracy of determination of the actual orientation of a given axis of the Orbital Reference Coordinate Frame. For purposes of geolocation, one is more concerned with attitude knowledge than attitude accuracy.

Platform attitude errors are described as rotations about the 3 axes of the Orbital Reference Coordinate Frame in units of arc-seconds. In this report, rotation about the X-Axis is described as Roll, rotation about the Y-Axis is described as Pitch, and rotation about the Z-Axis is described as Yaw. Table 3.4-6 shows the current 3 sigma specification of roll, pitch, and yaw attitude knowledge of the NPOESS Platform at the Instrument Mounting Plate. The information source is the NPOESS SRD. In the SRD the requirement is expressed in terms of separate low (0-10 Hz) and high (> 10 Hz) frequency uncertainties. These have been root sum squared in the table.

**Table 3.4-6. NPOESS Platform Attitude Knowledge 3 sigma Error Specification**

Platform Attitude Knowledge	Roll Error Spec	Pitch Error Spec	Yaw Error Spec
3 sigma Spec	33.5 arcsecs	33.5 arcsecs	33.5 arcsecs

Table 3.4-7 shows a 3 sigma error budget for the net NPOESS Platform pointing knowledge. This error budget includes the attitude determination component levied on the spacecraft as well as additional terms which effect instrument pointing, based upon experience with the Terra spacecraft, to compile an overall pointing error budget. The errors in this budget were separated into component parts with dynamic error components listed in the first four rows followed by static error components.

**Table 3.4-7. NPOESS Platform Attitude Knowledge 3 sigma Error Estimates**

Platform Attitude Knowledge Error Source	Roll Error Estimate	Pitch Error Estimate	Yaw Error Estimate
<b>DYNAMIC TERMS</b>			
Attitude Determination	33.5 arcsecs	33.5 arcsecs	33.5 arcsecs
Ephemeris Error	2.1	2.1	2.1
Thermal Distortion	15.0	15.0	15.0
<b>STATIC TERMS</b>			
Thermal Distortion	26.1 arcsecs	26.1 arcsecs	26.1 arcsecs
Moisture Distortion	18.0	15.0	15.0
Measurement Error	15.0	15.0	15.0
Gravity Effects	7.5	39.0	15.0
Launch Shift	24.0	24.0	33.0
Total Dynamic(RSS)	36.8 arcsecs	36.8 arcsecs	36.8 arcsecs
Total Static (RSS)	43.2 arcsecs	56.8 arcsecs	49.4 arcsecs
3 sigma Total Combined Allocation	56.7 arcsecs	67.7 arcsecs	61.6 arcsecs

Each error term was assumed to be independent with zero-mean Gaussian distribution. Errors within each category were combined by computing the sum of the squares of the component errors then taking the square-root (RSS error). The total RSS dynamic and static errors around each axis are shown towards the bottom of the table. The estimated Platform attitude/pointing error has an approximate equal static/dynamic breakdown.

### 3.4.3.3 VIIRS Instrument Pointing Error

Pointing errors from the VIIRS instrument are also described in terms of pointing accuracy and pointing knowledge. Pointing accuracy is the ability to align the line-of-sight to the target frame. Pointing knowledge is how well one knows the line-of-sight relative to the target. For purposes of geolocation we are concerned with pointing knowledge rather than pointing accuracy.

Instrument pointing errors are described in the same way as Platform pointing errors. It is an angular measurement, in units of arc-seconds, rotated about one of the 3 axes of the Orbital Reference Coordinate Frame. Rotation about the X-Axis is described as Roll pointing error, rotation about the Y-Axis is described as Pitch pointing error, rotation about the Z-Axis is described as Yaw pointing error.

Table 3.4-8 shows the current 3 sigma error estimates for VIIRS pointing knowledge. Once again, pointing errors were broken down into component parts. The expected dynamic error components about each axis are listed in the first 9 rows, the static error components follow. All error terms are assumed to be independent zero-mean Gaussian distributions.

**Table 3.4-8. VIIRS Instrument Pointing Knowledge 3 sigma Error Estimates**

Instrument Pointing Knowledge Error Source	Roll Error Estimate	Pitch Error Estimate	Yaw Error Estimate
<b>DYNAMIC TERMS</b>			
Telescope Thermal Effects	10.0 arcsecs	10.0 arcsecs	10.0 arcsecs
Telescope Bearing Runout	0.0	9.8	0.0
Telescope Control System Error	5.0	5.0	0.0
S/C-Induced Telescope Jitter	5.0	5.0	5.0
HAM Bearing Runout	0.0	4.9	0.0
HAM Thermal Effects	2.5	1.25	5.0
HAM Control System Error	2.5	1.25	5.0
S/C-Induced HAM Jitter	2.5	1.25	5.0
Aft Optics to OBA Thermal Effects	2.5	2.5	10.0
S/C-Induced Aft Optics Jitter	1.25	1.25	5.0
Detector Field Angle Stability	1.25	1.25	0.0
OBA Structure Thermal Effects	20.0	20.0	20.0
S/C-Induced OBA Jitter	5.0	5.0	5.0
<b>STATIC TERMS</b>			
Telescope Rotation Axis Tilt Error	10.0 arcsecs	10.0 arcsecs	0.0 arcsecs
Telescope Rotation Axis Cone Error	10.0	10.0	10.0
Telescope 1-G Sag	20.0	20.0	20.0
Telescope Environmental Shift	50.0	50.0	50.0
HAM Wedge Angle Error	0.8	0.4	1.7
HAM Rotation Axis Alignment Error	5.0	2.5	10.0
HAM to OBA Alignment Error	5.0	2.5	10.0
HAM 1-G Sag	2.5	1.25	5.0
HAM Environmental Shift	10.0	5.0	20.0
Aft Optics to OBA Alignment Error	2.5	2.5	10.0
Aft Optics Environmental Shift	12.5	12.5	50.0
Detector Field Angles	3.75	3.75	0.0
Focal Plane Orientation	1.75	1.75	0.0
OBA Structure 1-G Sag	50.0	50.0	50.0
OBA Environmental Shift	120.0	120.0	120.0
Total Dynamic(RSS)	24.6 arcsecs	26.6 arcsecs	27.4 arcsecs
Total Static (RSS)	142.6 arcsecs	142.2 arcsecs	152.1 arcsecs
3 sigma Total Combined Allocation	144.7 arcsecs	144.7 arcsecs	154.5 arcsecs

The 3 sigma static terms, in Table 3.4-8, are based on expected worst case scenarios. Once again, errors about each axis and within static or dynamic categories are assumed to be independent with zero-mean Gaussian distributions. The RSS of the error components within each category was computed to give a total dynamic and total static error. The estimated Instrument pointing error is dominated by the static instrument-to-spacecraft alignment uncertainty term. This component can be reduced by on-orbit calibration. The total RSS dynamic and static errors around each axis are shown towards the bottom of Table 3.4-10.

#### 3.4.4 Earth Location Impact

Section 3.4.2 explored the sensitivity of Earth location errors to position and attitude/pointing errors. Section 3.4.3 presented position, attitude, and pointing errors specific to the NPOESS Platform and VIIRS Instrument. In this section, this information is combined, and geolocation errors resulting from specific position/pointing errors of the NPOESS Platform and the VIIRS Instrument are explored.

The component Earth location errors are presented for 2 specific Platform/Instrument cases: the at-launch design, and the post-calibration (static bias removed) case. The at-launch design assumes the Platform and Instrument are built to the current specifications and performance estimates. The post-calibration case assumes that the Platform and Instrument are built to meet the current estimates, the current static error estimates are correct, and that much of this static error is removable through ground processing.

##### 3.4.4.1 Platform Position Error Component Impact

Table 3.4-9 summarizes the Earth location error resulting from the 3 sigma X, Y, and Z-Axis NPOESS Platform position error components. The first column in Table 3.4-9 presents the at-launch design and the second column presents the post-calibration case. The second column is included here for consistency with the tables to follow even though the on-orbit calibration has no effect on platform position knowledge. The first 3 rows show the 3 sigma X-Axis position error and the corresponding Earth location error, in meters. These numbers were computed both at nadir and at scan angle of 55.84 degrees. The middle 3 rows show Y-Axis related errors, and the last 3 rows show Z-Axis related errors.

**Table 3.4-9. Geolocation Impact of 3 sigma Spacecraft Position Errors**

	At-Launch	Post-Calibration
X-Axis Platform Position Error	75.0 m	75.0 m
Corresponding Along-Track Earth Location Error (scan=0)	66.4 m	66.4 m
Corresponding Along-Track Earth Location Error (scan=55.8)	64.5 m	64.5 m
Y-Axis Platform Position Error	75.0 m	75.0 m
Corresponding Cross-Track Earth Location Error (scan=0)	66.4 m	66.4 m
Corresponding Cross-Track Earth Location Error (scan=55.8)	66.4 m	66.4 m
Z-Axis Platform Position Error	75.0 m	75.0 m
Corresponding Cross-Track Earth Location Error (scan=0)	0.0 m	0.0 m
Corresponding Cross-Track Earth Location Error (scan=55.8)	177.9 m	177.9 m

#### 3.4.4.2 Platform Attitude Error Component Impact

Table 3.4-10 summarizes the Earth location error resulting from the 3 sigma pitch, roll, and yaw NPOESS Platform attitude/pointing error components. Once again, the at-launch design and the post-calibration case are presented. The first 3 rows shows the 3 sigma Platform roll error and the corresponding Earth location error. The middle 3 rows show pitch related errors, the last 3 rows show yaw related errors.

**Table 3.4-10. Geolocation Impact of 3 NPOESS Platform  
Attitude Knowledge Error Components**

<b>Platform Attitude</b>	<b>At-Launch</b>	<b>Post-Calibration</b>
Roll Pointing Error	56.7 arcsecs	36.8 arcsecs
Corresponding Cross-Track Earth Location Error (scan=0)	228.2 m	148.1 m
Corresponding Cross-Track Earth Location Error (scan=55.8)	1417.4 m	919.7 m
Pitch Pointing Error	67.7 arcsecs	36.8 arcsecs
Corresponding Along-Track Earth Location Error (scan=0)	272.4 m	148.1 m
Corresponding Along-Track Earth Location Error (scan=55.8)	330.6 m	179.7 m
Yaw Pointing Error	61.6 arcsecs	36.8 arcsecs
Corresponding Along-Track Earth Location Error (scan=0)	0.0 m	0.0 m
Corresponding Along-Track Earth Location Error (scan=55.8)	446.3 m	266.5 m

### 3.4.4.3 Instrument Pointing Error Component Impact

Table 3.4-11 summarizes the Earth location error due to the 3 sigma pitch, roll, and yaw VIIRS Instrument pointing error components.

**Table 3.4-11. Geolocation Impact of 3 sigma VIIRS Instrument Pointing Knowledge Error Components**

Instrument Pointing	At-Launch	Post-Calibration
Roll Pointing Error	144.7 arcsecs	27.6 arcsecs
Corresponding Cross-Track Earth Location Error (scan=0)	582.3 m	111.2 m
Corresponding Cross-Track Earth Location Error (scan=55)	3616.1 m	690.4 m
Pitch Pointing Error	144.7 arcsecs	29.6 arcsecs
Corresponding Along-Track Earth Location Error (scan=0)	582.1 m	119.0 m
Corresponding Along-Track Earth Location Error (scan=55)	706.5 m	144.4 m
Yaw Pointing Error	154.5 arcsecs	31.9 arcsecs
Corresponding Along-Track Earth Location Error (scan=0)	0.0 m	0.0 m
Corresponding Along-Track Earth Location Error (scan=55)	1118.9 m	230.6 m

### 3.4.4.4 Combined Cross-Track and Along-Track Geolocation Error due to Position, Attitude, and Pointing Errors

Combined Earth location error in the along-track and cross-track directions are calculated by evaluating the square root of the sum of the squares (RSS) of the components.

Cross-track Earth location errors are contributed by errors in :

- Y-Axis Spacecraft position
- Z-Axis Spacecraft position
- Platform roll
- Instrument roll

Along-track Earth location errors are contributed by errors in :

- X-Axis Spacecraft position



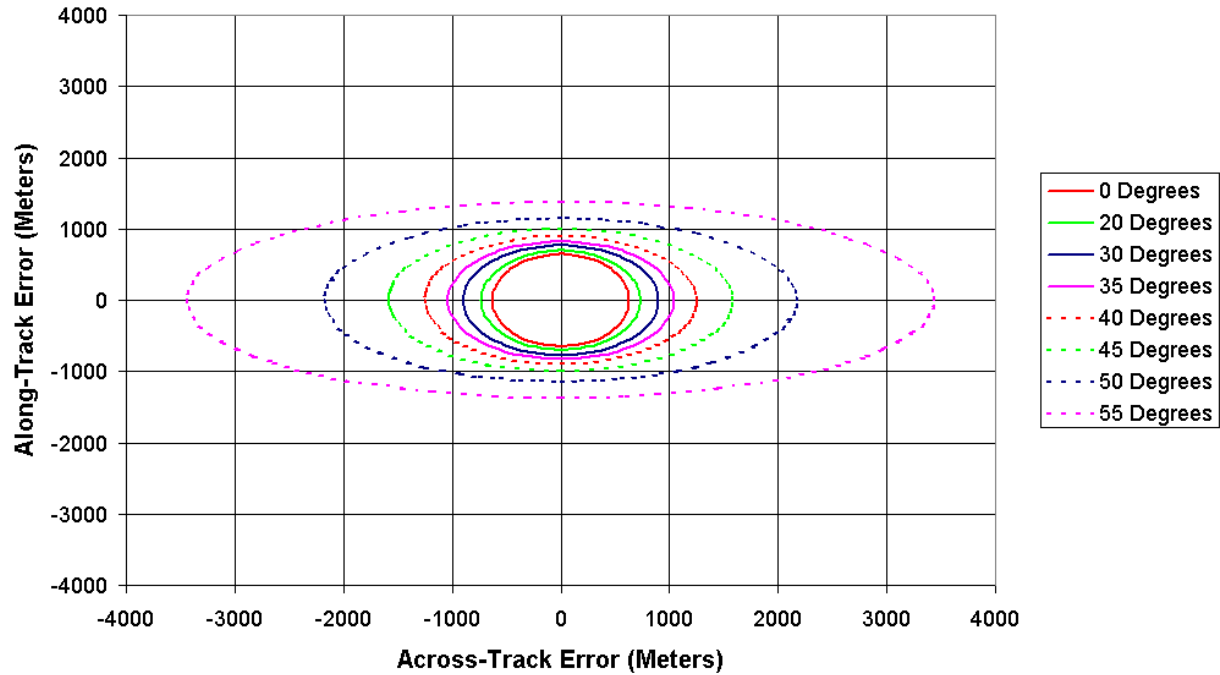
- Platform pitch
- Instrument pitch
- Platform yaw
- Instrument yaw

Table 3.4-12 summarizes the cross-track and along-track Earth location error for the two cases presented earlier. In addition, Earth location error based on fraction of a radiometric band pixel and an imaging band pixel is shown.

**Table 3.4-12. Total Combined 3-sigma RSS Geolocation Error  
in Cross-Track and Along-Track Directions**

	Total RSS Cross-Track Earth Location Error (3 sigma) (Y-Axis Spacecraft Position) (Z-Axis Spacecraft Position) (Platform Roll) (Instrument Roll)		Total RSS Along-Track Earth Location Error (3 sigma) (X-Axis Spacecraft Position) (Platform Pitch) (Instrument Pitch) (Platform Yaw) (Instrument Yaw)	
	scan = 0	scan = 55.8	scan = 0	Scan = 55.8
At-Launch	628.9 meters 0.800 pixels Radiometric Bands 1.600 pixels Imaging Bands	3888.6 meters 2.430 pixels Radiometric Bands 4.861 pixels Imaging Bands	646.1 meters 0.871 pixels Radiometric Bands 1.742 pixels Imaging Bands	1436.6 meters 0.898 pixels Radiometric Bands 1.796 pixels Imaging Bands
Post-Calibration	196.7 meters 0.250 pixels Radiometric Bands 0.501 pixels Imaging Bands	1165.6 meters 0.728 pixels Radiometric Bands 1.457 pixels Imaging Bands	201.2 meters 0.271 pixels Radiometric Bands 0.542 pixels Imaging Bands	426.1 meters 0.266 pixels Radiometric Bands 0.533 pixels Imaging Bands

The cross-track and along-track combined Earth location error can also be presented graphically. Figure 3.4-6 depicts the combined 3 sigma Earth location error resulting from Platform/Instrument position, attitude, and pointing errors based on the at-launch design. The centered origin of the plot represents perfect Earth location. Dashed grid lines are overlaid at 200 meter intervals. The innermost ring represents the 3 sigma Earth location error of pixels viewed at a scan angle of 0 degrees. Successive rings depict 3 sigma geolocation errors for pixels observed from increasing scan angle.



**Figure 3.4-6. Three-Sigma Earth Location Error (in meters) resulting from the at-launch design for Scan Angles of 0, 20, 30, 35, 40, 45, 50, and 55 degrees**

Figure 3.4-7 shows the combined 3 sigma Earth location error resulting from Platform/Instrument position, attitude, and pointing errors based on the post-calibration case.

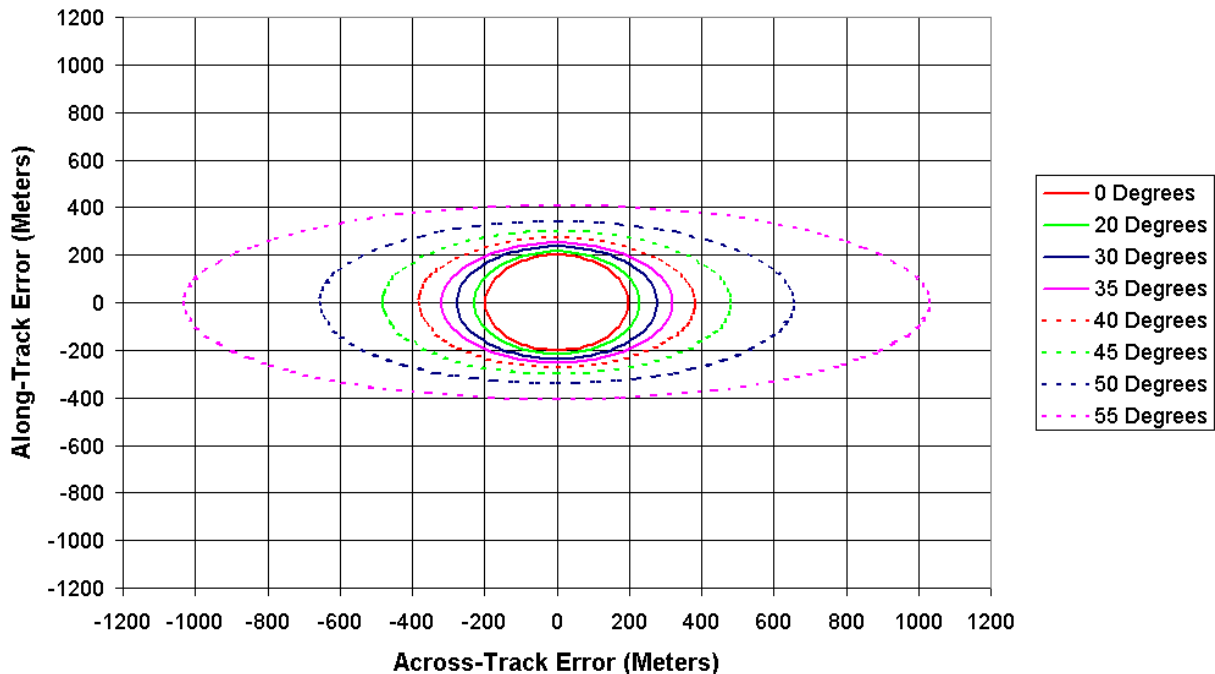


**Figure 3.4-7. Three-Sigma Earth Location Error (in meters) resulting from the post-calibration estimates for Scan Angles of 0, 20, 30, 35, 40, 45, 50, and 55 degrees**

### 3.4.5 Geolocation Equations and Methods

The equations used to calculate pixel geolocation error resulting from errors in Platform position in space, Platform/Instrument pointing, Earth terrain height, (also equations to calculate pixel distortion), were taken from the “MODIS Earth-Location Algorithm Theoretical Basis Document” (Wolfe *et al.*, 1997). A complete presentation of the underlying equations, with accompanying figures, is presented in that document and will not be repeated here.

### 3.4.6 Ground Processing

The VIIRS ground processing system is being designed to incorporate the capability to estimate and correct some of the residual errors described in this report. This includes building additional features into the operational VIIRS product generation software and developing additional tools for off-line geometric data analysis. This analysis will contribute to the refinement of the VIIRS geometric models over time.

#### 3.4.6.1 Earth Location Processing Approach

The VIIRS processing software is being designed with the minimization of Earth location error as a primary goal. Errors that are known or measured (e.g., telescope angles, band and detector offsets) will be corrected, or correction data will be appended, during geolocation processing. The geolocation algorithm will use the best available estimates of the platform and instrument geometric parameters (e.g., platform/instrument alignment) stored in a calibration parameter file as ancillary data. These parameters will be refined over time using measurements of the residual error present in previously processed data products.

Errors that are static or slowly varying and can be adequately modeled will be estimated by comparing VIIRS data products with ground control to measure the residual geometric distortion. The measured distortion from a series of products will be used to detect systematic trends and to estimate improved values for the platform and instrument geometric parameters. A library of ground control points will be created and maintained to provide the necessary geometric reference. The control point image chips will be compared with the VIIRS imaging bands from selected data products, using automated image correlation techniques to measure the residual (presumable sub-pixel) geometric distortion. Trend analysis and parameter estimation activities will be carried out off-line using the distortion measurements from multiple data products.

The geometric distortion measurements will be collected routinely and analyzed to estimate the residual static biases in the pre-flight platform and instrument geometric parameters and to monitor the stability of these static error estimates. Improved values of the bias estimates will periodically be generated for use in subsequent processing and reprocessing. Selected data products will be extracted from the archive for more rigorous interactive evaluation. This will include manually verifying the residual error measurements at the control points to validate the automated correlation process and comparing products from the same orbital path to verify image-to-image registration.

The off-line geometric analysis and parameter estimation effort will grow more ambitious with time as more data becomes available. A long data record will make it possible to compare the control point data with VIIRS image data from repeated and different orbital passes under varying conditions to detect constant offsets and slowly varying trends. Slowly varying dynamic errors that are repeatable and can be effectively modeled will be incorporated into the VIIRS geometric models over time.

#### 3.4.6.2 Geometric Error Characteristics

The primary sources of VIIRS geometric error are described in the preceding sections and fall into four main categories: ephemeris errors, attitude errors, instrument/platform alignment errors, and instrument internal geometry errors. Errors from each of these sources have been characterized as static or dynamic. Static errors can, in principle, be estimated and corrected but the ability to model, estimate, and compensate for dynamic errors is limited by the time constant of the error dynamics. Low frequency dynamic errors (e.g., those varying over an orbit) can be detected and estimated with a reasonable number of ground control points while high frequency errors (e.g., those varying within a scan) cannot. This makes an understanding of the nature of the anticipated errors central to the development of geometric correction models and places a limit on what can be achieved by ground processing.

Ephemeris errors are dynamic but can be successfully modeled as constant biases to the six-element "spacecraft state vector" over periods of several minutes. Although these errors could be estimated using ground control point observations, it would require a dense global network of ground control to perform routine ephemeris error correction. The same comments apply to the dynamic component of the attitude error though these attitude errors typically vary more rapidly than ephemeris errors, requiring even more frequent ground control observations. A significant component of the anticipated attitude error has been characterized as static. The problem of estimating the static attitude biases is complicated by their high correlation with the residual

biases in the instrument-to-platform alignment.

The instrument pointing errors are likewise divided between static and dynamic errors with the largest single term being the instrument-to-platform alignment knowledge. The instrument-to-platform alignment error should be primarily a static bias, possibly with some slowly varying, repeatable thermal effects included. The geometric relationship between the instrument and the platform will initially be assumed to be static, but the VIIRS processing software will be designed to accommodate a time varying transformation to allow for future model refinement. Telescope rotation variations, though dynamic, are measured in the VIIRS instrument and will be corrected in geolocation processing. Other internal instrument geometric errors are difficult to measure. Most internal alignment errors are highly correlated with the external instrument-to-platform alignment.

### 3.4.6.3 Limitations of Ground Processing

As mentioned above, the ability to model and correct residual geometric errors through ground processing is limited by the time scale and repeatability of the dynamic error components and the observability (parameter correlation) of both the static and dynamic errors. This is made even more challenging by the demanding VIIRS operational environment, in which continuously acquired data must be processed in near real-time with no operator intervention.

The ability to accurately measure sufficient ground control points in a fully automated system is limited by cloud cover, the availability and quality of world-wide ground control, and the performance of automatic correlation methods over varying viewing geometry and scene conditions. Attempting to estimate and apply corrections specific to a particular data set runs the risk of introducing product consistency problems due to differences in cloud cover and the resulting control point correlation performance. These concerns have led to the current approach in which control point data from multiple products will be analyzed with human intervention to monitor and refine the knowledge of the static and slowly varying error components for use in subsequent processing.

The achievable geometric product accuracy is also limited by the quality of the ancillary data sources, specifically the digital elevation model used to correct for terrain effects, and by the characteristics of the VIIRS instrument itself. The accuracy with which ground control points can be measured in the VIIRS data is limited by the resolution of the VIIRS pixels. Experience with Landsat and SPOT data has shown that operational automated image matching techniques reliably measure image displacement to an accuracy of 1/3 to 1/2 of a pixel. Using the 742/786 meter resolution imaging bands will provide a control point measurement accuracy of from 250 to 375 meters. Achieving bias estimation accuracy better than this will require the use of many control point observations. The ability to transfer the Earth location knowledge gained through the use of the imaging bands to the radiometric bands is further limited by the band-to-band registration knowledge.

### 3.4.7 Terrain Height Error Impact

The National Imagery and Mapping Agency (NIMA) DTED-1 (a digital terrain data base), distributed by the United States Geological Survey (USGS) for the United States and by the

Department of Defense (DOD) for selected parts of the world, has a specified vertical accuracy of 30 meters (linear error encompassing 90% of the data points). The portion of DTED controlled by DOD has large areal gaps over South America, Africa, Australia, Antarctica, and remote parts of Asia; in addition, it has not yet been approved for general release. Over the next several years data from the Shuttle Radar Topography Mission (SRTM) will become available for most of the world's land area between 60 degrees north latitude and 56 degrees south latitude at a spatial resolution (~100 meters) and accuracy (~30 meters) comparable to or better than the DTED-1. Regions outside the SRTM latitude range are covered by the global GTOPO-30 elevation database constructed for the EOS project. This data set provides elevations approximately every 1000 meters (30 arc-seconds) and was compiled from a variety of sources including DTED and Digital Chart of the World (DCW). A conservative estimate of the accuracy of the GTOPO-30 data is 160 meters (90% linear error) based on the DCW accuracy measured during the construction of GTOPO-30 by comparing DCW data to DTED.

Figure 3.4-8 shows the Earth location errors resulting from a 30 meter and a 160 meter terrain height error. A 30 meter inaccuracy is representative of the SRTM data while the 160 meter inaccuracy is representative of the DCW-derived GTOPO-30 data available at high latitudes. The resulting Earth location error is primarily in the cross-track direction and is a function of scan angle. There is no impact on geolocation at nadir. The geolocation error reaches a one-to-one correspondence (a 1 meter terrain height error leads to a 1 meter geolocation error) at a scan angle of approximately 40 degrees. Since geolocation error is linear with terrain height error, one can easily estimate Earth location error resulting from any terrain height error from this plot.

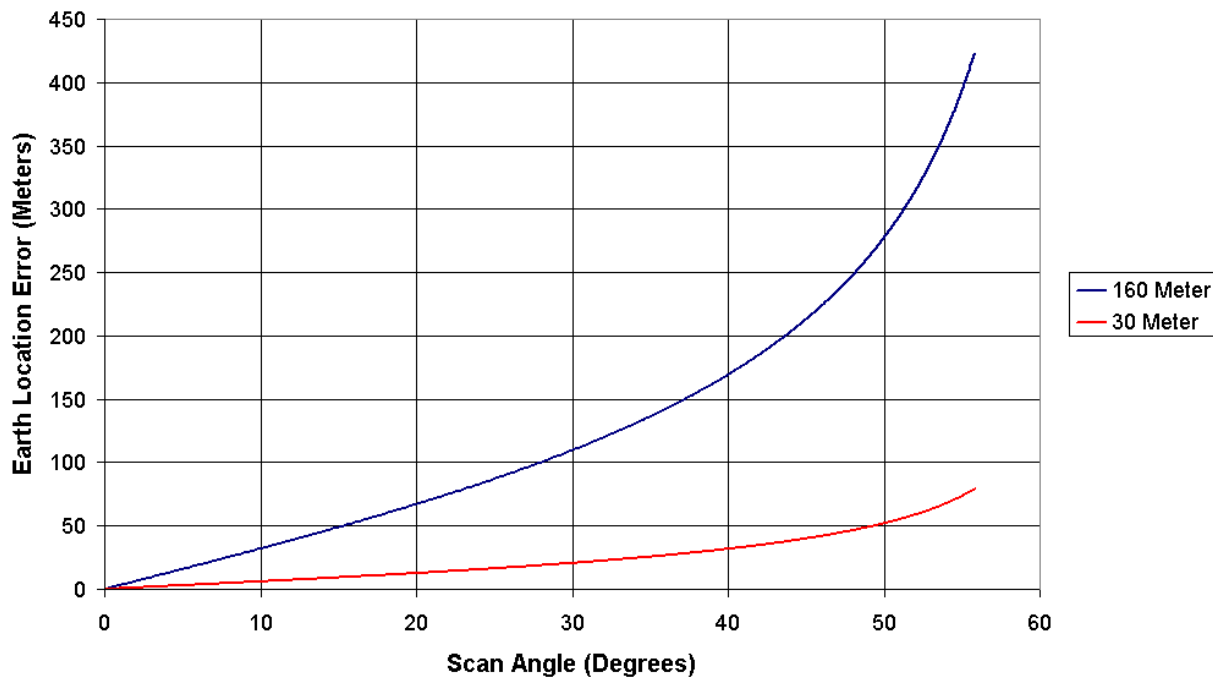


**Figure 3.4-8. Earth Location Error (in meters) resulting from various Terrain Height Errors as a Function of Scan Angle**

Terrain height induced error is unlike the other errors described in this document with regard to collocation of two pixels observed at different times. For any given location it is not random from one observation to the next. There is good and bad news resulting from this. The good news is, if two observations of the same point are made during different times but when the pixel is directly under the spacecraft, there will be no terrain height induced error in location or coregistration. If the two observations are made from different orbits with very similar ground tracks, for instance both ground tracks pass about 800 km to the right of the point under consideration, there may be a large location error but it will be nearly the same for both observations. Thus there will only be a small coregistration error. The bad news is, if one orbit ground track is to the left of the ground point and the other is to the right, the geolocation error will be the same in magnitude but in opposite directions. This means that the terrain height induced coregistration error will be the sum of the magnitudes of the two geolocation errors. Thus if precise coregistration is important for a particular investigation, it becomes important to give special consideration to the viewing geometry of the various observations.

### 3.4.8 Summary

There are five issues which are of concern with regard to accurate geolocation and/or coregistration of VIIRS data: Platform position knowledge, Platform attitude knowledge, Instrument pointing knowledge, detector to detector registration, and terrain height error. Three of these, the location and attitude of the Platform and the pointing of the Instrument are comparable to or better than that for previous instrument data sets such as MODIS. Their impact is such that VIIRS pixel data could be correctly Earth located within 0.7 (radiometric band) pixels (3 sigma). Earth location accuracy could be improved to within 0.3 pixels if ground processing is able to remove the expected biases. Thus these errors are of the same scale as those due to band to band registration accuracy error (0.2 pixels) and inadequate terrain height information at high latitudes (0.1 pixels).

### 3.4.9 Error Analysis Algorithms

The 742/786 meter resolution VIIRS imaging bands will be used in conjunction with sets of ground control points to validate the accuracy of the VIIRS Earth location data. Ground control points will be used to estimate residual errors in the spacecraft ephemeris and attitude. Small geolocation errors are mainly caused by errors in these parameters. Other parameter errors are difficult to analyze. However, through long term trend analysis, we are hoping to expand error analysis to the focal plane, telescope geometry, and half-angle mirror assembly geometry. The land ground control matching algorithm is first explained and then the trend and bias analysis.

#### 3.4.9.1 Land Control Point Matching and Correlation Algorithm

The Control Point Matching software will use the control points to automatically collect the raw verification data (in the form of ground control point residual errors). This data will then be analyzed off-line. The control point processing methods to be employed for VIIRS are the same as those developed for the MODIS sensor. These techniques are described in detail in the "MODIS Earth-Location Algorithm Theoretical Basis Document" (Wolfe *et al.*, 1997) and will only be summarized here.



## General Background and Preprocessing

The higher resolution VIIRS imaging bands will be used in conjunction with preassembled sets of ground control points to validate the accuracy of the VIIRS Earth location data. The known position of the control point can be used to extract an image neighborhood from the new VIIRS data at the location predicted by the Earth location data. Nominal radiometric calibration parameters will be applied to the VIIRS neighborhood to remove radiometric artifacts (detector to detector striping). A simple cloud detection algorithm (e.g. thresholding) will also be used to identify areas that are not suitable for image correlation. This product validation will be scheduled after the radiometric correction and cloud detection algorithm have been performed so that the simple radiometric correction, snow, sea ice and cloud detection algorithm would be skipped. In either case, the control point image chip can then be correlated with the VIIRS neighborhood to measure the sub-pixel displacement between its predicted and observed locations. The control data image chips will be processed to simulate the effects of the VIIRS viewing geometry including the elevation-related parallax and correlated with the real image data. This will include applying the VIIRS modulation transfer function (MTF) to the higher resolution control chips. The extracted VIIRS data will be shifted along the image lines and pixel counts over the control point chip. At each fraction of shift in the positive or negative direction, the MTF is applied over this higher resolution control point chip and matched with the VIIRS resolution. The measured image displacement shift or error angles, along with the extracted VIIRS neighborhoods, will then be passed along for off-line analysis.

## Control Point Image Chips and Control Scenes

The MODIS control point library, derived from Landsat Thematic Mapper data, will be augmented as necessary by Landsat 7 Enhanced Thematic Mapper Plus (ETM+) data. The improved absolute geodetic accuracy of the ETM+ data combined with the availability of SRTM terrain data make it possible to construct high-quality control points over a larger portion of the globe. Each control point is selected to contain a primary identifiable feature which will provide a strong target for image correlation at the VIIRS imaging band scale.

The term feature will be used here to mean a single, identifiable, geographical point on the earth's surface, specified by exactly one set of coordinates: latitude, longitude, and elevation. Ideally, the latitude, longitude, and elevation values point to a stable geographical feature that is detectable in VIIRS data. Each land control point chip will have exactly one key feature. Features that are close together may be used but they will be put into separate, possibly overlapping, control point chips.

## Extraction of Control Scene for Each Control Point Chip

Based on VIIRS granule's geographical metadata, (i.e., on the latitude and longitude coordinates of the corner points of the VIIRS data granule) a list of control points that could be in that granule will be constructed. The following steps will be taken to build a VIIRS control scene for each control point.

Step 1. Find a scan which contains the predicted control point based on the geographic locations of the scan,

Step 2. Find a fractional pixel/line number from the geographic location of the control point



using an inverse mapping algorithm and determine a nearest pixel (called feature pixel),

Step 3. Extract line segments from the current scan containing its neighborhood,

Step 4. Extract extra line segments from the above (and or below) the scan if the control point is too near the edge of the scan.

Figure 3.4-9 shows schematically how a control scene would typically be created using three scans.

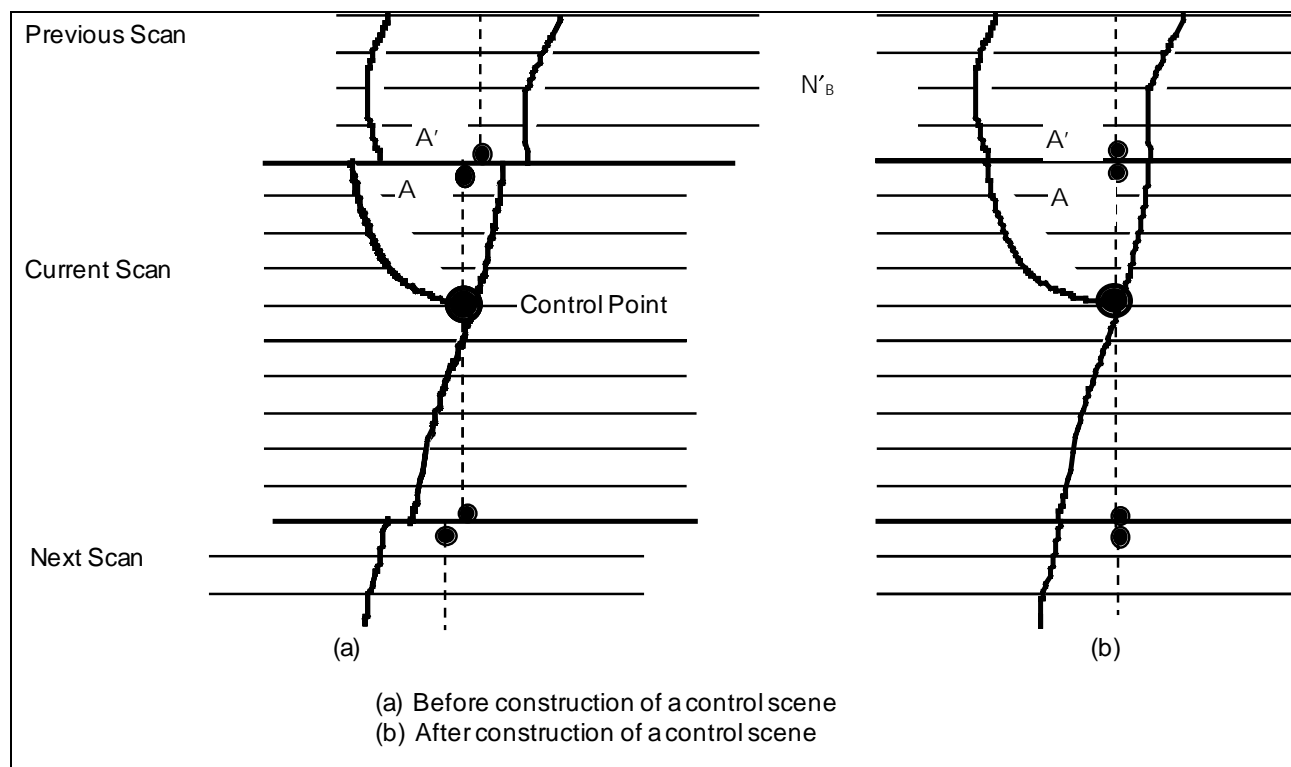


**Figure 3.4-9. Connecting Parts of 3 Scans**

### Simulated VIIRS Scenes with VIIRS Pixel Resolution

This section explains how a VIIRS imaging band size pixel is generated from TM pixels.

When a VIIRS detector in motion views TM pixels on the ground, the TM pixel radiances must be summed and put through the triangular weighting function, and pixel aggregation, to generate expected VIIRS pixels. All of the TM pixels within a 2-VIIRS-pixel wide rectangle are weighted and added together to get the VIIRS pixel value, as shown in Figure 3.4-22, where geometry does not show possible terrain and scan angle effects.

In Figure 3.4-10, TM pixel locations 1 and 2 are contributing to VIIRS pixel I and II, while No 3 and 4 are contributing to VIIRS pixel II and III. The triangular weighting function and the two pixel wide set of TM pixels used to generate an expected VIIRS pixel in bold outline.

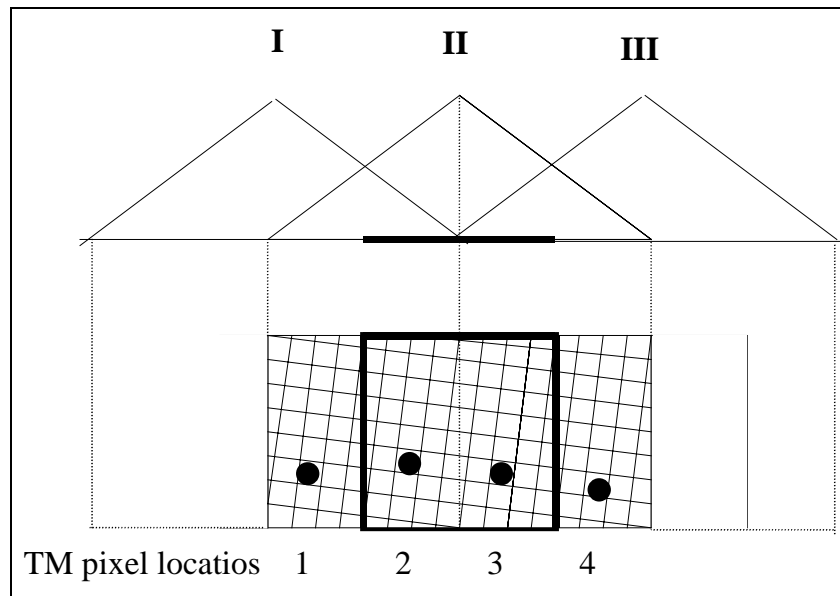


**Figure 3.4-10. Triangular Weighting Function**

To prepare for the correlation of TM and VIIRS chips, multiple simulated VIIRS scenes are generated at different sub-pixel offsets. Finding the simulated VIIRS scene which best matches the actual VIIRS data identifies the best-fit sub-pixel offset for that control point.

### Correlation of Simulated VIIRS Scenes and Actual VIIRS Control Scene

The cross correlations between simulated and actual VIIRS scenes will be performed using the normalized cross correlation function. (See ECS Project, 1995 at page 683, equation 20.4-1.)

In a shift pattern of ten steps of 1/10th of a pixel each, there are  $11 \times 11 = 121$  cross correlations to be performed. After all of the expected VIIRS pixel arrays are constructed and all the cross correlations are computed, the offsets that produce the maximum cross correlation are determined. The actual location of the best sub-pixel match point can be used to generate:

- (1) Actual location of the control point in the VIIRS scene in terms of fractional line/pixel numbers.
- (2) Sensor view vector.
- (3) Systematically computed geodetic coordinates of the control point.
- (4) Residuals error for residual data base, along with the VIIRS control scene.

### Error Conditions

The following conditions are regarded as errors:

- If the maximum cross correlation occurs at the edge of the shift region, then that set of geolocation residual error values should be flagged as suspect and as out of range.

- It is likely that either the cross correlations failed to detect the correct location of the feature in the image, or that the image correction needed is larger than what the algorithm is capable of measuring (e.g., larger than one VIIRS pixel).
- If a maximum cross correlation value occurs in two adjacent elements of the cross correlation matrix, then the residuals could be recorded as the average of the two corresponding values.
- If the maximum cross correlation value occurs in more than two (or more than one) element of the cross correlation matrix, then no residuals will be recorded for that control scene.

### 3.4.9.2 Error Analysis and Parameter Estimation Algorithm

The geolocation error comes from various sources including errors in satellite position, velocity, attitude, sensor misalignments, and telescope related errors. It may also be possible to have clock drift in the sensor data stream differing from the spacecraft's. Many of the sensor and telescope characteristics and internal temperature will be continuously collected and included in the telemetry. Some changes may appear in the form of such as attitude parameters and could be observed through the evaluation of control point residuals.

In this section, we describe the algorithm to estimate satellite position/velocity and attitude parameters through use of ground control points. It is assumed that some of the sensor misalignments and telescope error will be absorbed in the attitude parameter error.

From the control point matching algorithms, the following values are expected for each control point:

1. Time of control point observation,
2. Satellite position and velocity,
3. Attitude parameters  $\xi_r^0, \xi_p^0, \xi_y^0$  for roll, pitch, and yaw
4. Fractional scan line and pixel counts and a view vector in the spacecraft coordinate system pointing to the control point,
5. Systematic control point coordinates in the ECR coordinate system,
6. Control point coordinates in the ECR coordinate system,
7. Half-angle mirror side information(used in the trend analysis).

It is important to know that the error analysis depends on the accuracy of the control point matching results.

To express a ground control point and view vector, the following notations are used:

- |                       |  |
|-----------------------|--|
| <b>p</b>              | - True location of satellite(to be estimated),               |
| <b>p<sub>0</sub></b>  | - Satellite location from the systematic data,               |
| <b>x<sub>0</sub></b>  | - Ground control point location through the systematic data, |
| <b>x<sub>cp</sub></b> | - True ground control point location.                        |

For their relationship, see Figure 3.4-11.

In this section, we do not expect any large errors in satellite positions, attitude, or instrument clock time. Even if the control point's location and predicted location is a few pixels off, the control point matching algorithm may not be able to detect and this algorithm cannot use any residual information.

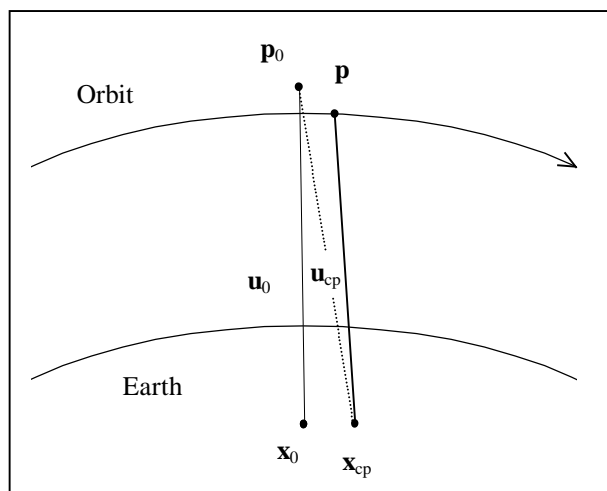


**Figure 3.4-11. Satellite Position and Ground Control Point**

Errors detected and calculated by the ground control point matching algorithm as described above will be used in the error analysis algorithm. Assuming errors are small, we will follow a methodology used by Landsat 7 (see USGS, 1997) and MODIS (Wolfe *et al.*, 1997) and refine our error estimate for correcting the parameters. In this approach, satellite position/velocity and attitude parameter residuals are estimated through use of the Earth and satellite geometry. The differences in the control point location and systematic point locations are used to construct a normal equation. By solving the normal equation, the error is estimated and the original parameter set is updated to create a new set of parameters. This process continues until it reaches a certain threshold.

The process is described in detail in the “MODIS Earth-Location Algorithm Theoretical Basis Document” (Wolfe *et al.*, 1997) and in the “Landsat 7 Image Assessment System Geometric Algorithm Theoretical Basis Document” (USGS, 1997) and will not be repeated here. The algorithm solves a set of observation equations using standard minimum-variance estimation techniques. Since the observation equations are non-linear and are linearized by computing partial derivatives, the entire process must be iterated until the correction parameters converge.

Sensor misalignments and telescope errors will be studied by examining the trends in long term results. More complex (e.g., time or temperature dependent) models for these parameters will be developed based on actual experience with VIIRS data and will be verified against a long term data record prior to implementation in the production stream.

### 3.5 PRACTICAL CONSIDERATIONS

The following sections discuss practical implementation and operational considerations

including numerical stability, computational efficiency, algorithm verification, product validation, automated quality control and metadata generation, and possible processing exception conditions.

### 3.5.1 Numerical Computation Considerations

The VIIRS Earth location algorithm incorporates two iterative procedures that must be implemented carefully to ensure convergence. The first of these is the general iterative conversion from ECR to geodetic coordinates. This procedure is straightforward and robust.

The second iterative procedure is the detection of the VIIRS line of sight intersection with the terrain. Simple approaches to implementing this algorithm break down at high off-nadir angles due to the possibility of multiple intersections of the line of sight with the terrain surface. Under these conditions, care must be taken to ensure that the algorithm converges to the correct terrain intersection point (i.e. the intersection closest to the satellite). This is achieved here by searching from above to find the first (highest) terrain intersection. The iteration proceeds down monotonically until the viewing vector is below the terrain surface so that convergence is not a problem. The precision of the final terrain intersection determination is a function of the local relief. The degree to which this approximation breaks down is a function of the height range searched and the satellite look angle. These statistics will be monitored for quality control purposes as described in Section 3.6.2.

### 3.5.2 Programming/Procedural Considerations

The computational burden imposed by the VIIRS Earth location algorithm arises primarily from the terrain intersection computation. Current estimates indicate that approximately 80% of the Earth location processing load is used by the terrain correction step. Within this procedure the conversion from ECR to geodetic coordinates consumes the bulk of the processing.

In the ECR to geodetic conversion the main computational driver is the number of trigonometric functions that must be performed. One way to achieve efficiency in these computations is to carefully apply small angle approximations and Taylor series expansions when the angles involved change very little between invocations. Another approach is to implement the standard sine and cosine functions as look-up tables that have been pre-computed based on the required precision of the calling routine. The tradeoff of computational precision for computational performance would have to be carefully weighed before implementing any of these approximations.

### 3.5.3 Configuration of Retrievals

The Earth location data fields will be generated using a fully automated process during routine operations with human intervention required only in anomalous circumstances. In order to achieve the required Earth location accuracy, however, it will be necessary to perform an initial on-orbit geometric calibration to estimate the static pointing errors that will be present when using only prelaunch characterization data. These instrument characterization and calibration activities, described in section 3.4.11, will require a skilled analyst with considerable knowledge of the VIIRS instrument. It will also require the development of the necessary analysis software tools and the assembly of the required supporting ground control data and reference imagery before launch.

### 3.5.4 Quality Assessment and Diagnostics

The VIIRS Earth location procedure will accumulate performance indicators during the normal course of processing for inclusion in the product metadata as quality control information. Numeric performance indicators include the number of suspect ephemeris points replaced and the number of suspect attitude points replaced. Other quality control fields include quality information taken from the ancillary input data sets such as the DEM and possibly the ephemeris and attitude data if it came from a source other than the RDR data itself.

These quality control fields will be included in the product metadata along with other descriptive data such as a record of the ancillary data lineage (e.g., data set version number and date, preprocessing history).

### 3.5.5 Exception Handling

The Earth location algorithm will provide mechanisms for gracefully handling the following three known exception conditions:

1. There are missing ephemeris or attitude data,
2. There are missing DEM data, and
3. The instrument line of sight does not intersect the Earth.

The input ephemeris and attitude data will be checked for consistency and completeness by the geolocation processing software. These checks will be first order only and will primarily remove blunders. For example, the magnitude of the position and velocity must be close to the nominal values and the instrument must be pointing downward, etc. If these ancillary data are completely missing or unusable, an error message will be generated and Earth location data will be filled by interpolation with appropriate quality control information entered into the product metadata. In the case of missing input DEM data, the Earth location will proceed using the Earth ellipsoid as the reference terrain surface. A warning message will be generated and an appropriate notation added to the product metadata. If the line of sight intersection algorithm detects a viewing vector that does not intersect the Earth ellipsoid, the geodetic position fields will be populated with fill values, a warning message will be generated, and a notation will be added to the product metadata.

## 3.6 ALGORITHM VALIDATION AND DISCUSSION

### 3.6.1 Algorithm Verification

The purpose of the algorithm verification process is to verify that the algorithm will accurately calculate the location of VIIRS samples. This verification process will verify the accuracy of the algorithms presented here in this document as well as the algorithm's implementation in software. Initially at launch there will be systematic biases in the model that will be removed by the geometric parameter estimation process. It is expected that over time the algorithm will

converge to an accurate solution which will be stable and repeatable in both scene to scene and scene to ground measurements.

There are three steps in the verification process. First, the software implementation of the Earth location model must match the algorithm. Second, the algorithm implementation must correctly represent the instrument. Third, the software implementation should match the end-to-end system, which verifies both the instrument model and the satellite and Earth models. The tools for measuring the accuracy will be tested as part of the verification process.

Once the algorithm has been verified, care must be taken that, as the algorithm evolves, the chain of verification is not broken. This process will involve careful feedback of model changes, both to the algorithm and constants. This will be done by verifying that the new model increases the accuracy from the previous baseline for multiple products.

#### 3.6.1.1 Verification Standard

The VIIRS accuracy testing involves two types of related measurements, absolute and relative. The former measures how well the VIIRS instrument matches a location on the Earth. The latter measures how well multiple images from the same area on the ground match one another. If two images have an absolute accuracy of 100 m, then the relative accuracy of the images is better than 200 m and would be around 141 m if the errors are uncorrelated and normally distributed. A measurement of relative accuracy does not necessarily give any information about the absolute accuracy; two scenes that are well registered to one another could be off by a large amount in an absolute sense.

The absolute error is very important in using VIIRS data with other data sets, such as maps and other satellite data. The standard by which the absolute accuracy is based is the World Geodetic System of 1984 (WGS84), an international standard model of the Earth. This standard is based on a number of physical constants, including the origin and orientation of an Earth centered and fixed Cartesian coordinate system, a standard ellipsoid model of the Earth, and a definition of mean sea level. Many countries are now basing their new maps on this standard and there are standard transformations from most older maps to this standard.

The relative measurement is very important in determining what changes occur between images. Since the mission is to look at global change, measuring season-to-season and year-to-year variations are very important. There is no standard for the relative accuracy measurements. It is expected that by achieving the absolute accuracy goal, the relative accuracy requirements will be met.

#### 3.6.1.2 Preflight Verification

The VIIRS algorithms will be verified preflight by prototyping key Earth location subsystems to develop and refine geometric models, and data processing and analysis techniques using both preflight data and data from other instruments such as MODIS.

The verification that the software matches the theoretical algorithm will be performed by software walk through and unit testing of individual parts of the algorithm. Separate hand calculations will be performed to verify that the unit testing is correct. The second step is to verify the instrument part of the model. This will be done by verifying that the results from the

instrument model match those from live data from the engineering model. The third step will be done both preflight and in-flight. The preflight part will be done using satellite data from other instruments such as MODIS. Parts of the software model, which are common to both VIIRS and MODIS, will be tested by verifying the Earth location of the MODIS data. In addition, simulated VIIRS data will be available to test the algorithm preflight.

### 3.6.1.3 In-flight Verification

The in-flight accuracy of the VIIRS Earth location data will be verified using automated control point correlation methods coupled with off-line analysis. Control point measurement will be built into the VIIRS geolocation production system but, operationally, will only be applied to a subset of the data products based on control availability and cloud cover. This product verification activity is described in more detail below.

The schedule for in-flight Earth location/geometric verification activities is less well defined than the preflight phase. The planned activities are divided into Short-Term (conducted in the first three months after activation), Medium-Term (conducted in the first year of operation), and Long-Term (ongoing sustaining activities) in Table 3.6-1.

The performance of the automatic correlation procedure will be verified through interactive control point mensuration. The performance of interactive control point mensuration method is expected to be less accurate than the automatic procedure but will be used to provide a double check of the algorithm. The image internal geometric accuracy will be verified by correlating multiple VIIRS products from the same orbital path. This will include looking for even/odd scan artifacts due to differences in the two half-angle mirror sides. The control chips and neighborhoods will be used to verify the performance of the control point mensuration procedure itself, while the measured distortions will be used in anomaly detection, trend analysis, and to build up a statistical record of Earth location performance.



**Table 3.6-1. In-flight Algorithm Verification Activities**

Time Frame	Activity
Short-Term (first three months)	Verify Earth location algorithm performance as soon as operational data becomes available.
	Look for constant bias terms in control point QA results to assess accuracy of instrument alignment knowledge.
Medium-Term (first year)	Estimate refinements to instrument alignment knowledge using control point QA data.
	Analyze ancillary digital terrain data accuracy using orbit-to-orbit tie points.
	Analyze control point QA results to characterize repeatable errors correlated with scan angle and/or mirror side.
	Use control point QA results to detect repeatable within-orbit trends such as thermal effects.
	Use data from multiple instruments to estimate spacecraft position and attitude accuracy performance.
Long-Term (sustaining activities)	Analyze control point QA data for trends to monitor stability of instrument geometric parameters.
	Refine geometric models for mirror and thermal effects as appropriate based on longer data record.

#### 3.6.1.4 Verification of Inputs

The verification of the inputs to the VIIRS Earth location process must be performed to enable the overall process to be verified. It is expected that the inputs to the VIIRS Earth location algorithms will have systematic biases in them. As part of the verification process, these inputs will be verified and biases removed. These inputs include information about the geometric characterization and calibration of the instrument and spacecraft, information about the spacecraft position, velocity, attitude, telescope encoder data, ground control points, and the DEM. For the computational saving, the geolocation calculation is performed only for the ideal band. All real bands' locations on the ground are derived from the ideal band location as described in section 3.3.2. Because of this, the control point residual calculation relies on the approximated values. The approach will create some systematic or random error for the ground control point residual error calculation.

#### Instrument and Spacecraft Data Verification

The geometric characterization and calibration of instrument, spacecraft, and ancillary data are integral to the verification process. Geometric calibration activities that are being performed by the instrument and spacecraft contractors will be carried out in accordance with their contract schedules. Specifically, the preflight VIIRS instrument geometric calibration will be performed by the SBRS according to their calibration plan. Of particular interest to the Earth location model are the absolute orientation, telescope positioning, MTF, and band-to-band registration tests.

Preflight measurements of the instrument-to-spacecraft alignment will presumably be carried out during the instrument/spacecraft integration phase per the NPOESS development schedule.

The verification of the spacecraft pointing knowledge and position information will be performed by the spacecraft builder and the IPO. The science and telemetry data from the instrument and the telemetry data from the spacecraft, up to the point where it is input into the Earth location model, must also be verified.

Refinements to the knowledge of the alignment between the various parts of the instrument, and the instrument to the spacecraft, will be done as part of the geometric parameter estimation process.

The input data stream to be used for geolocation of VIIRS products will be read from the engineering packets and validated, which includes the spacecraft orbit position and velocity, attitude angles and rates, and the telescope encoder times. The scan start times and half-angle mirror side indicators, which are also required for geolocation, will be unpacked and converted by the unpacking software. It is assumed that any validation required for those data has been performed prior to geolocation. The validation tests to be performed fall into four basic categories: absolute limits, delta limits, consistency, and sanity.

1. The absolute limit test checks individual measurements against a specified range. For a value  $V$  and lower and upper limits  $L$  and  $U$ , the test requires that

$$L \leq V \leq U \quad (3.6-1)$$

2. The delta limit test checks the differences between successive values of an individual measurement against a specified range. For a delta limit  $\delta$ , the test requires that

$$|V_{j+1} - V_j| \leq \delta \quad \text{for } j\text{-th and } j+1 \text{ th sample of } V. \quad (3.6-2)$$

3. Consistency tests compare different measurements within a general category to verify consistency among the measurements.
4. Sanity tests involve computing additional quantities from the measurements, which can be checked against absolute limits such as magnitude of position and velocity vectors. These are performed to take advantage of our knowledge of the mission limits or the physical processes involved.

### Ground Control Verification

There are two methods for verifying the accuracy of the ground control point information. The first method is to internally verify the control using information from either VIIRS or other satellites. The second is to use some other type of verification such as an accurate map base or points from the Global Positioning System (GPS). In either case, there will be some prior knowledge of the accuracy of the control point information based on the source.

To use satellite data for validating the control points, it will be assumed that the error in the position of the satellite is random and that the pointing knowledge errors do not systematically

vary over any single location. If both these assumptions were true, it would be easy to take the large number of measurements of the points and then improve the knowledge of the control points using this information. However, only the first is true. The pointing knowledge errors are expected to have some systematically varying component, which we plan to remove as part of the geometric parameter estimation. If only the NPOESS satellite or satellites with similar orbit characteristics are used, the same type of bias may occur in all of the measurements. This would prevent the separation of the ground control bias from the systematically varying component of the pointing knowledge. So, it is not possible to use only the satellite data to validate the ground control points.

One problem in verifying the absolute accuracy of the VIIRS instrument is with the original maps and other sources which to be used in collecting control point information. In some well mapped areas of the world such as the United States of America (USA), it is easy to acquire highly accurate maps. In the continental USA, Canada, Europe, and some other areas, typical maps have a low enough vertical and horizontal error to be used as sources for absolute control point location information. The rest of the world is not as well mapped. In some areas the only maps available are 1:250,000, or even 1:1,000,000 scale maps. The accuracy of these maps is typically from 125 to 450 m horizontally and 50 to 200 m vertically. In areas of the world where accurate maps are unavailable, Landsat 7 ETM+ and SRTM elevation data, accurate to approximately 50 meters horizontally and 30 meters vertically, can be used instead.

Using an accurate map base or GPS has some appeal but there are also problems with this approach. First, the availability of accurate maps throughout the world is limited and the collection of GPS verified control points is likely to be expensive. Even once the ground control has been identified there is still the problem of transferring this knowledge to the image. Typically, a control point can only be identified in an image to the nearest 1/2 pixel by an operator. This should not be much of a problem with VIIRS because the control points are being identified in higher resolution images.

The correlation process may introduce a systematic bias into the process since it relies on correlation of an area and not the location of a single point. One bias may be caused by a change in elevation over the correlation area; the second may be caused by temporal changes in the scene or in the viewing geometry of the scene. In the case of errors introduced by elevation, correlation techniques rely on locking up on unique strong features in the correlation area. In the case when there is only a single strong feature at the center of the correlation area, this is not a problem. Many times, however, there are a number of less strong features in the area, which, if they are at a different elevation than the main feature, may cause the correlation process to be biased. To minimize this type of effect, efforts will be made to pick control points in areas that are relatively flat, or to orthorectify the control points before use. Then the VIIRS viewing geometry will be simulated as described in section 3.4.11.

Temporal changes and changes in the viewing geometry may cause other biases. Both may cause the correlation to fail completely. If a correlation is successful, there is a possibility that a systematic bias may be introduced by changes in the scene. For instance, if the correlation is occurring on a large lake in which the shallow end is partially covered by ice in the winter, the correlation of this area would tend to be biased toward the deep end of the lake. A different viewing geometry may also cause a similar bias. Suppose the image is of a volcanic island and the original image of the ground control point is taken when the shadows are to the left of the

mountain. If, when the point is later imaged, the viewing conditions are such that the shadow has moved to the right side of the mountain, there is a good possibility the correlation will be biased.

One solution that has been used in the past to alleviate this problem with correlation has been to use a large number of control points. If many control points of different types are used then this error can be treated as a random error. In any case, statistics should be kept for each control point. Moreover, care should be taken to use the good control points in the geometric parameter estimation, and to include the control point correlation statistics in the solution as well as any measured mean shift in the location.

### Digital Elevation Model Verification

The terrain correction accuracy will be verified and areas of poor DEM data will be identified by measuring tie points between overlapping VIIRS products. The DEM will be verified in two ways. First, the provider of the DEM will perform quality checks to verify its accuracy. It is expected that the DEM provided will have, at worst, a 1 km resolution with 160 m uncertainty in vertical direction (e.g., GTOPO-30). Second, multiple elevation data sets (SRTM and GTOPO-30) will be compared to each other in regions of common coverage.

Once the images have been correctly navigated, the image data will be rectified and then areas from overlapping orbits will be correlated. The tie points would be generated automatically, possibly using an interest operator to generate "good" tie points. Once this is done a sufficient number of times, there may be certain areas of the world where there is a systematic bias between every image pair. It is expected that biases covering large areas may be found using this method but the vertical accuracy when correlating the imaging bands is expected to be, at best, 250 m (1 sigma). Particular care should be taken to do this type of correlation only after sufficient systematic biases have been removed from the pointing knowledge. Lack of sufficient high frequency information in the DEM will cause residual high frequency errors in the VIIRS Earth location knowledge. It will not be possible to remove these errors until a higher resolution DEM becomes available.

### 3.6.2 Product Validation

The validation process will examine the end result of the process (the Earth location product) and not the mechanism for producing the product. This process will be done independently of the verification process. A number of products will be selected and measurements will be performed independently of the production software. This process will not necessarily be a global process but sufficient number of measurements will be made so that there is a high level of confidence in product accuracy for the entire globe. This validation process will be done with some regularity, either biannually or annually, and after any significant modifications to the production software or constants occur. Both the absolute and relative accuracy of the products will be validated.

The validation measurement tools will be developed independently of the production tools. Ground control information will also be independently collected for measurements of absolute accuracy. Of course, the same source material, maps, etc., may be used for ground control information.

### 3.6.3 Risks and Risk Reduction Efforts

The most significant Earth location algorithm risk is that the Earth location data fields generated will not be sufficiently accurate due to inadequate knowledge of the VIIRS instrument's operating characteristics. As the error analysis in section 3.4 demonstrates, the anticipated prelaunch knowledge of the key geometric characteristics is such that the initial on-orbit Earth location data is not expected to meet the accuracy requirements. The errors present in the at-launch geometric parameters can be categorized into four groups:

1. Static errors that are unknown but do not change after launch, such as an overall rotation of the sensor relative to the spacecraft;
2. Quasi-static errors that do not change with time, but do vary with scan angle, such as telescope axis or half-angle mirror wedge and tilt angle errors;
3. Low-frequency dynamic errors that change slowly with time in a more-or-less predictable way, such as orbital temperature-induced distortion;
4. High-frequency dynamic errors that change too rapidly or randomly to predict or measure, such as bearing runout and servo errors.

As shown in section 3.4, the initial on-orbit Earth location error model is dominated by static pointing errors. These errors can be effectively measured and modelled as sensor alignment offsets using the calibration techniques successfully demonstrated by Landsat 7 (USGS, 1997 ) and MODIS (Wolfe *et al.*, 1997). Quasi-static errors are more challenging but can also be addressed using reference imagery to measure VIIRS offsets at all scan angles and by analyzing data from many VIIRS scans. A method for solving the similar problem of estimating the Landsat 7 Enhanced Thematic Mapper Plus scan mirror profile on orbit has also been demonstrated (USGS, 1997).

The fundamental approach to mitigating the risk of inadequate Earth location accuracy has two aspects. First, the Earth location algorithm and its software implementation are designed to explicitly model and allow for updates to the values of the key geometric characteristics of the VIIRS instrument. Second, the required algorithms, software, analysis skills, and supporting data needed to measure, characterize and, through calibration, remove both static and quasi-static errors will be prepared prior to launch. Following the examples of Landsat 7 (USGS, 1997) and MODIS (Wolfe *et al.*, 1997), this analysis suite will also include the capability to measure and characterize low-frequency errors such as thermal distortions so that corresponding modelling and calibration software can be implemented in the unlikely event that it proves to be necessary.

## 4.0 ASSUMPTIONS AND LIMITATIONS

### 4.1 ASSUMPTIONS

The error analysis presented in Section 3.4.1 assumed that the individual contributors to the overall VIIRS Earth location error were independent zero-mean Gaussian distributed random variables. In addition, the Earth location algorithm was developed under the assumption that the nature and magnitudes of the errors are essentially correct. The quality of the available DEM data is assumed to conform to the characteristics specified in section 3.4.7, although this does not affect the algorithm itself, only its final performance.

The implementation of the VIIRS Earth location algorithm described above is based on the final assumption that the output product data structure will be sufficiently flexible to permit the addition of eight new Earth location data fields for each spatial element and to allow the efficient extraction of control point neighborhoods from the imaging bands for automated product validation.

### 4.2 LIMITATIONS

Several simplifying assumptions were made in the development of the VIIRS Earth location algorithm. These assumptions and their justifications are as follows:

- Ignore atmospheric refraction of the line of sight - Analysis of the refraction indicates it may be as high as 30 m at the edge of a scan. Later versions of the software will take this refraction into account.
- Ignore light travel time - The maximum range to a terrestrial target seen by VIIRS is about 1800 km. This corresponds to a light travel time of 6 msec. This is a significant effect that causes as much as a 21 m bias at the edges of the scans. Later versions of the software will take this effect into account.
- Ignore velocity aberration – The relativistic deflection of the apparent instrument line-of-sight toward the spacecraft velocity vector is less than 15 meters (TBR) and does not vary greatly as a function of scan angle since the scan is nearly normal to the velocity vector. As such it can be subsumed under the pitch component of the instrument to spacecraft alignment calibration.
- Ignore the instrument telescope offset from the spacecraft center of mass - The ephemeris position represents the spacecraft center of mass rather than the instrument optical origin, but this offset is a few meters at most, which is less than the accuracy of the ephemeris data and much less than a VIIRS pixel.



## 5.0 REFERENCES

Documents applicable to this ATBD include:

Wolfe, Robert *et al.*, 1997. MODIS Level 1A Earth Location: Algorithm Theoretical Basis Document, Version 3.0, MODIS Science Data Support Team (SDST).

Fleig, Albert J., Paul A. Hubanks, James C. Storey and Lloyd Carpenter, 1993. An Analysis of MODIS Earth Location Error, Version 2.0, by MODIS Science Data Support Team (SDST).

NIMA, 1997. NIMA TR8350.2: Department of Defense World Geodetic System 1984 – Its Definition and Relationship with Local Geodetic Systems, Third Edition, prepared by the NIMA WGS84 Development Committee.

Snyder, John P., 1987. Map Projections - A Working Manual, United States Geological Survey (USGS) Professional Paper 1395, U. S. Government Printing Office, Washington.

USGS, 1997. Landsat 7 Image Assessment System Geometric Algorithm Theoretical Basis Document, Version 2, USGS EROS Data Center.

Rosborough, G.W., D.G. Baldwin and W.J. Emery, 1994. "Precise AVHRR Image Navigation", IEEE Transaction on Geoscience and Remote Sensing, Vol 32, No. 3.

Pratt, W.K., 1991. "Digital Image Processing", Second Edition, John Wiley & Sons, Inc.

ECS Project, 1995. Theoretical Basis of the SDP Toolkit Geolocation Package for the ECS Project, Technical Paper, 445-TP-002-002.

Wertz, J.R. (ed.), 1985. Spacecraft Attitude Determination and Control, D. Reidel Publishing Co., Vol. 73, pp 447-455.